TAMPERE UNIVERSITY OF TECHNOLOGY

JAAKKO MARTTILA

QUADRATURE SIGMA-DELTA ADCs: MODELING AND SIGNAL PROCESSING

Master of Science Thesis

Examiners: Professor Mikko Valkama
and Professor Markku Renfors
Examiners and topic approved in the
Computing and Electrical Engineering
Faculty Council meeting on 4 March
2009

ABSTRACT

TAMPERE UNIVERSITY OF TECHNOLOGY
Degree Programme in Signal Processing and Communications Engineering
MARTTILA, JAAKKO: Quadrature sigma delta ADCs: modeling and signal processing
Master of Science Thesis, 96 pages
May, 2010
Major: Digital Transmission
Examiners: Professor Mikko Valkama, Professor Markku Renfors
Keywords: analog-to-digital conversion, bandpass sigma-delta modulation, complex filters, digital radio, I/Q imbalance, mirror frequency interference

The versatile nature of modern wireless communications and on the other hand the push towards cost-efficiency, have created a demand for flexible radio transceivers. In addition, size and power consumption are critical for mobile solutions, thus setting their own demands for the circuitry. Traditionally in such architectures, the analog-to-digital converter has been seen as a performance bottleneck, limiting the possibilities to harness the full potential of the available digital signal processing techniques and algorithms. Therefore, analog-to-digital conversion based on a quadrature ΣΔ modulator noise shaping has been brought in as a promising possibility. More efficient noise shaping and better suitability for modern receivers applying complex signal processing principles already, compared to real counterpart make the quadrature converter particularly interesting choice.

This thesis discusses the main principles of quadrature ΣΔ converter and related signal modeling. In addition to understanding the basic operation, it is crucial to understand the implementation related nonidealities, which can't be avoided in any true circuit. One of the most important phenomena in this field, concerning the in-phase/quadrature processing in the transceivers, is the nonideal matching of the components on the two rails. Thus, the latter part of the thesis gives a detailed analysis on the mismatch problem in quadrature ΣΔ converters. Thereafter, the analysis is confirmed by computer simulations.

Finally, it is shown that the mismatch mentioned above is a real concern, especially under the influence of a mirror frequency blocking signal. This might very well be the case in a wideband radio receiver with reduced analog selectivity. On the other hand, the analysis shows that educated design of the signal transfer function can be efficiently used to mitigate the interference originating from the mirror frequency in case of mismatch in the complex feedback branch of the modulator. In this way, the generated distortion can be reduced without any additional electronics, which would compromise cost-efficiency and other demands. Additionally, it is pointed out that independent frequency domain mirroring of the noise and the signal component sets challenges for traditional compensation algorithms. Thus, there is a call for innovative ideas to mitigate the mirror frequency distortion in quadrature ΣΔ modulators via digital signal processing. In this way the cost-efficiency, power consumption and size requirements wouldn't be jeopardized due to additional electronics.

TIIVISTELMÄ

TAMPEREEN TEKNILLINEN YLIOPISTO
Signaalinkäsittelyn ja tietoliikennetekniikan koulutusohjelma
MARTTILA, JAAKKO: Kvadratuuri-sigma-delta-AD-muuntimet: mallintaminen ja signaalinkäsittely
Diplomityö, 96 sivua
Toukokuu, 2010
Pääaine: Digitaalinen siirtotekniikka
Tarkastajat: Professori Mikko Valkama, professori Markku Renfors
Avainsanat: analogia-digitaalimuunnos, digitaalinen radio, I/Q-epätasapaino, kaistanpäästö-sigma-delta-modulaatio, kompleksiset suodattimet, peilitaajuushäiriö

Nykyaikaisen langattoman tiedonsiirron monimuotoisuus, ja toisaalta tarve kustannustehokkuuteen, ovat luoneet tarpeen joustaville radiolähetin-vastaanottimille. Mobiilipäätelaitteissa myös koko ja virrankulutus ovat tärkeässä asemassa, asettaen näin omat vaatimuksensa laitteistolle. Tällaisissa rakenteissa analogia-digitaalimuunninten suorituskykyä on pitkään pidetty pullonkaulana nykyaikaisten digitaalisten signaalinkäsittelytekniikoiden tarjoaman potentiaalin hyödyntämiselle. Tämän seurauksena kvadratuuri ΣΔ-modulaattoriin perustuva analogia-digitaalimuunnos on esitetty lupaavana ratkaisuna. Reaaliseen rakenteeseen perustuvaa vastinetta tehokkaampi kohinanmuokkaus ja parempi sopivuus moderneihin kvadratuurivastaanottimiin, joissa hyödynnetään kompleksista signaalinkäsittelyä jo valmiiksi, tekevät muuntimesta erityisen mielenkiintoisen vaihtoehdon.

Tässä diplomityössä esitellään kvadratuuri-ΣΔ-muunnoksen perusperiaatteet ja siihen liittyvät signaalimallit. Tämän lisäksi on myös tärkeää, perustoiminnallisuuden ymmärtämisen lisäksi, tiedostaa todelliseen piiritoteutukseen liittyvät väistämättömät epäideaalisuudet. I/Q prosessointia hyödyntävissä radiolaitteissa yksi tärkeimmistä tämän tyyppisistä ilmiöistä on kahden haaran välinen epäsovitus. Tästä johtuen sovitusongelma kvadratuuri ΣΔ muuntimissa analysoidaan tarkasti ja tietokonesimulaatioilla varmennetut tulokset esitetään tämän diplomityön loppupuolella.

Työssä osoitetaan, että yllä mainittu epäsovitus on todellinen huolenaihe, erityisesti voimakkaan häiritsevän signaalin ollessa läsnä peilitaajuudella. Tällainen tilanne saattaa toteutua erityisesti laajakaistaisessa vastaanottimessa, jossa analogista selektiivisyyttä on pyritty vähentämään. Toisaalta analyysi osoittaa, että älykkäästi suunniteltu signaalisiirtofunktio auttaa tehokkaasti poistamaan modulaattorin takaisinkytkentähaarassa sijaitsevan epäsovituksen aiheuttamaa häiriötä. Tällä tavoin syntynyttä vääristymää pystytään vähentämään ilman ylimääräistä elektroniikkaa, jolloin kustannustehokkuudesta, tai muista vaatimuksista ei tarvitse tinkiä. Tämän lisäksi osoitetaan, että signaali- ja kohinakomponenttien toisistaan riippumaton peilaantuminen taajuuden suhteen luo haasteita perinteisille korjausalgoritmeille. Näin ollen kvadratuuri-ΣΔ-modulaattoreiden peilitaajuushäiriön hallitsemiseksi digitaalisen signaalinkäsittelyn keinoin tarvitaan uudenlaisia innovaatioita. Tällä tavoin voitaisiin myös välttää analogisen lisäelektroniikan aiheuttama kustannustehokkuus-, virrankulutus- ja kokovaatimusten vaarantuminen.

PREFACE

This Master of Science Thesis work, "Quadrature sigma-delta ADCs: modeling and signal processing," was supported by the Academy of Finland, the Finnish Funding Agency for Technology and Innovation (Tekes) and the Technology Industries of Finland Centennial Foundation. The work was done in year 2009 while I was working at the Department of Communications Engineering (DCE) at Tampere University of Technology (TUT), Finland.

First and foremost I would like to thank my advisor Professor Mikko Valkama for his invaluable guidance and motivation. His deep devotion to the field of science has also been of great inspiration for myself and helped me to finish my Master's studies. I am also grateful for my co-examiner and Head of the DCE Professor Markku Renfors for his support and sharing his wide knowledge on digital communications.

My thanks go to my colleague and fellow student B.Sc. Markus Allén who has been of great help in numerous research problems. We have been studying ADC issues together and the discussions (on and off the topic) have been crucial in order to secure the correct understanding on the basics. I am also grateful for M.Sc. Lauri Anttila and M.Sc. Vesa Lehtinen for sharing their experience on the related research topics and for our office secretaries Tarja Erälaukko and M.Sc. Marianna Jokila for their help with practical arrangements. In addition, I would like to extend my thanks to all my co-workers in the DCE at TUT. Every each of You has guaranteed relaxed and productive atmosphere in your own way.

I am thankful for my friends for giving me also something else to think but the Thesis. Many thanks for my parents Jukka and Merja for being there whenever needed and believing in me. Finally, I would like to express my special gratitude to Reetta for her unconditional love during the ups and downs.

Tampere, 15 April 2010

Jaakko Marttila

CONTENTS

LIST OF ABBREVIATIONS

A/D	analog-to-digital
ADC	analog-to-digital converter
AWGN	additive white Gaussian noise
BP	bandpass
BPF	bandpass filter
CT	continuous-time
DAC	digital-to-analog converter
DC	direct current, zero-frequency
DSP	digital signal processing
FIR	finite-impulse-response
HT	Hilbert-transformer
I/Q	in-phase/quadrature
IF	intermediate frequency
INTF	image noise transfer function
IRR	image rejection ratio
ISTF	image signal transfer function
LO	local oscillator
LPF	lowpass filter
MASH	multi-stage noise shaping
NTF	noise transfer function
OSR	oversampling ratio
PCM	pulse-code modulation
RF	radio frequency
SC	switched-capacitor
SNR	signal-to-noise ratio
STF	signal transfer function

LIST OF SYMBOLS

$A, A_N, B, C, G, G_N, F, M, N$	complex multipliers
b	number of quantization bits
CF_{dB}	crest factor in decibels
f_0	frequency
f_{3rd}	center frequency of a third harmonic
f_B	signal bandwidth
f_C	center frequency of a radio frequency signal
f_{IF}	intermediate frequency
f_{LO}	local oscillator frequency
f_S	sampling frequency
$\overline{f}_{pass}$	NTF notch frequency relative to f_S
$\overline{f}_{int}$	STF notch frequency relative to f_S
$\mathcal{F}[\cdot]$	Fourier-transformation of the argument
$H_N[z]$	transfer function of the N th loop filter
$H_{nom}[z]$	nominal value of and common-mode error in $H[z]$
$INTF[z]$	image noise transfer function in z-domain
$ISTF[z]$	image signal transfer function in z-domain
IRR_{STF}	image rejection ratio of the STF
IRR_{NTF}	image rejection ratio of the NTF
L	order of the modulator

$\max(\cdot)$	maximum value
$NTF[z]$	noise transfer function in z-domain
p_{common}	the pole common to the NTF and the STF
r	$\log_2(OSR)$
$\mathrm{sgn}(\cdot)$	sign of the argument
$STF[z]$	signal transfer function in z-domain
T_S	sampling time instant
$x(t)$	continuous-time signal
$x(k)$	discrete-time signal
$x_I(t), x_Q(t)$	in-phase and quadrature components of $x(t)$
$X[z]$	Z-transformation of $x(k)$
x_{re}, x_{im}	real and imaginary parts of complex x
$x_{im,1}, x_{im,2}$	independent implementations of ideal x_{im}
w_{OPT}	optimum coefficent of the compensation filter
z_{NTF}	zeros of the NTF
z_{STF}	zeros of the STF
α_{bp}	notch frequency tuning parameter in BP ΣΔ modulator
$\Delta(\cdot\cdot)_{diff}$	differential error in the product
$\Delta H_{diff}[z]$	differential error in $H[z]$
σ_x^2	variance of x
ω	angular frequency

$(\cdot\cdot)_{nom}$	nominal value of and common-mode error in the product
$(\cdot)^*$	complex conjugation

1. INTRODUCTION

The strongly heterogeneous and mobile nature of the modern wireless communications calls for flexible radio transceivers. The transmitter and the receiver should be able to handle several different cellular systems together with wireless local area networks and positioning systems. The biggest challenges are set on the mobile terminals, like cellular phones, where the functionalities should be implemented in small size with low power consumption and cheap price for the mass-market. Especially the receiver functionalities should be implemented in a flexible way to ensure a smooth cross-system operation. These demands have encouraged the drive towards increasing the role of digital signal processing (DSP) in the mobile radio receivers. In this way, the analog front-end of the receiver could be simplified and made independent of the particular communication standard in use. Thus, designing multiple parallel receivers for the numerous systems could be avoided. [9], [11], [29], [44], [50]

In a digital multi-system receiver, the radio frequency (RF) processing should be simple, flexible and implemented with relatively cheap electronics. The RF front-end would then be followed by analog-to-digital (A/D) conversion. Thereafter, rest of the processing and selectivity would be implemented in the digital domain. [29] The conversion has been proposed to be done on either baseband [9], [11], [10], [29], or some chosen intermediate frequency (IF) [29], [61] depending on the exact architecture chosen. Also direct RF-sampling based reconfigurable receiver architecture has been described in [50].

In this composition, the A/D converter (ADC) has been widely considered as a performance bottleneck. A wide frequency band, involving multiple information signals, must be converted with adequate precision, taking probable large fluctuations in the power levels of the inter-system signals into account. [29], [42], [80] These aspects will be highlighted in Chapter 2 of the thesis, which will first give an introduction to in-phase/quadrature (I/Q) processing and then an overview on modern receiver architectures.

One of the most promising solutions to this problem is low-IF multi-standard receiver with a quadrature bandpass ΣΔ ADC. [29], [61] The ΣΔ principle allows shaping the quantization noise away from the frequency band of interest, thus making exploitation of the whole quantization precision on the desired signal possible [2], [7], [24], [68]. In addition, the quadrature version of the converter allows designing complex noise- and signal transfer functions (NTF and STF) not being restricted to be symmetric in respect of the zero-frequency (DC) [8], [30], [32],[33] [34], [35], [68]. This property can be put to use particularly in modern quadrature image rejecting receivers [30], [34]. The basic ΣΔ principle will be discussed in Chapter 3, which is expanded to specifics of the quadrature converter in Chapter 4. Mostly the discrete-time implementation of the modulator is considered. Main differences between discrete- and continuous-time systems are included in Chapter 3.

However, the push towards cost-efficiency and cheaper electronics gives rise to circuit nonidealities, such as nonlinearities [29], [55], [56], mismatch of the I and Q rails [55], [75], [76] timing jitter in the sampling circuit [43], [76] and oscillator phase noise [29], [56]. This work will concentrate on the I/Q mismatch and resulting mirror frequency interference related to the aforementioned quadrature ΣΔ converter [30], [33], [34], [84]. The interference mechanism will be discussed in detail in Chapter 5 and then some mitigation related aspects will be highlighted. The analysis is confirmed with computer simulations in Chapter 6. Thereafter, digital post-processing algorithm [3] is simulated, in context of quadrature ΣΔ modulator, to compensate mirror frequency interference. Some quadrature ΣΔ specific analog I/Q mismatch mitigation methods [12], [53], [57] have been presented in the literature, but digital post-compensation is desirable because no alteration, possibly compromising aforementioned demands set for mobile terminals, for the original modulator structure is needed.

Selected parts of this work have been published in IEEE International Microwave Workshop Series on “RF Front-ends for Software Defined and Cognitive Radio Solutions” [46]. Additionally, full-length journal article [47] has been submitter to Springer Circuits, Systems and Signal Processing Journal and it is under review at this moment.

2. RECEIVER ARCHITECTURES

In modern wireless communications, there are a number of different standards and systems designed for various purposes. This abundance and heterogeneity combined with rapid technical development have led to a few alternative radio transceiver topologies. The most remarkable receiver architectures will be introduced in the following. This knowledge is essential for the motivation and understanding for the rest of the work.

As a first step and an introduction to the receiver architectures, the basics of complex – or in-phase/quadrature – signal processing will be covered. This will form a basis for the topics discussed later in this chapter.

2.1. I/Q Signal Processing

Digital communication standards of today have widely adopted complex signals, consisting of the I and Q components, in to use. With I/Q processing it is, e.g., possible to use the radio spectrum more efficiently than in former systems exploiting only real signals. Most of the complex processing is usually done in the digital domain of the transmitter and the receiver, but on the other hand, also analog frequency translation and image signal rejection are of notable significance.

2.1.1. Complex Signals and Systems

It is said, that complex representation of the signals and systems is the natural way for the researcher or engineer in the field of radio communications. They provide convenient way to describe the functionality of the modern system standards and related transceivers. Moreover, as Martin states in the title of his well-known article [45] “Complex Signal Processing is Not Complex”.

Complex signals consist of two real signals. Having $x(t)$ as a complex signal, it can be represented with two separate real signals by $x(t) = x_{re}(t) + jx_{im}(t)$, where $x_{re}(t)$ and $x_{im}(t)$ denote the real and imaginary parts (also in-phase and quadrature components), respectively [45]. One of the basic examples employing this kind of structure is the

complex oscillator producing an exponential tone as an output. There two real tones have ideally 90° phase difference, the components being $\sin(2\pi f_0 t)$ and $\cos(2\pi f_0 t)$. Combining these two as was shown above leads to complex tone $\cos(2\pi f_0 t) + j\sin(2\pi f_0 t) = e^{j2\pi f_0 t}$.

The best way to express the benefits of using complex-valued signals is frequency-domain presentation with Fourier transform $\mathcal{F}(\cdot)$. The spectrum of a complex exponential tone in Figure 2.1 shows that signal energy is no more symmetrically situated around zero-frequency. For real signal $r(t)$ such symmetry exists, which is mathematically denoted by

$$R(-f) = R^*(f), \tag{2.1}$$

where $R(f) = \mathcal{F}[R(t)]$ and $(\cdot)^*$ is complex conjugation [16], [43]. On the other hand, there is no such restriction for complex signals in general. Thus, the negative and positive frequencies can be processed independently when complex signals and systems are applied. [75]

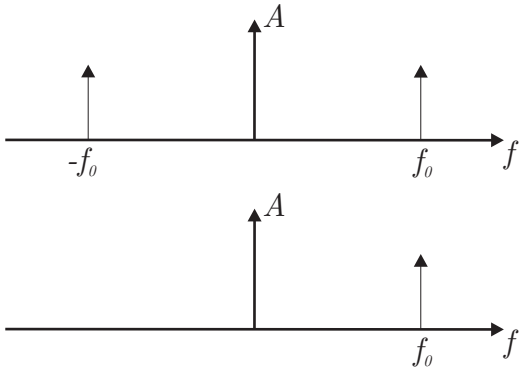

Figure 2.1 *Theoretical spectra of a real (up) and a complex (down) oscillator tone at the frequency* f_0.

2.1.2. Frequency Translation and Bandpass Signals

In modulated radio communication systems, originally baseband information signal is usually transmitted on certain non-zero center frequency – often referred as radio frequency. A complex information signal $x(t)$, or a pair of real signals ($x_{re}(t) + jx_{im}(t)$), can be transmitted as a real bandpass signal

$$r(t) = 2\,\mathrm{Re}[x(t)e^{j2\pi f_C t}] = 2x_{re}(t)\cos(2\pi f_C t) - 2x_{im}(t)\sin(2\pi f_C t), \tag{2.2}$$

where f_C is the center frequency of $r(t)$ and $\mathrm{Re}[\cdot]$ denotes the real part of a complex value [16], [43]. This real signal $r(t)$ has symmetric spectrum according to (2.1). Though, carried complex information signal $z(t)$ doesn't need to be symmetric around f_C [43] as is graphically shown in Figure 2.2. Frequency content originally lying around DC is transferred to a certain center frequency f_C by multiplying the information signals with oscillator signals, which have 90° phase difference as shown below. This operation, usually known as real mixing, produces a frequency translation of $\pm f_C$. The mentioned 90° difference in the carrier phases guarantees the recoverability of the information signals. If this condition is maintained ideally, the peak and zero values of the two carriers are coincident and thus don't interfere each other in the sampling process. In addition, (2.2) shows that transmitting two real information signals at the same time in complex form doesn't affect the used overall bandwidth and thus it increases spectral efficiency. [75]

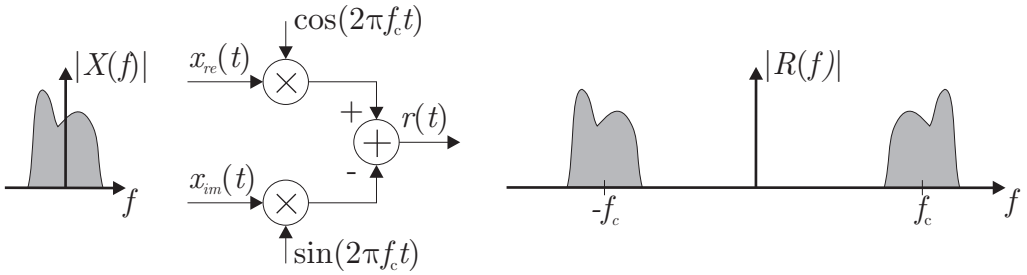

Figure 2.2 *Bandpass signal generation and symmetric frequency translation [75].*

The information signals $x_{re}(t)$ and $x_{im}(t)$ can be recovered from $r(t)$ by applying reverse bandpass-to-lowpass transformation. Either one of the symmetric copies in frequency domain around $-f_C$ or $+f_C$ can be used for this. Equation (2.2) can be modified to take a form

$$r(t) = 2\,\mathrm{Re}[x(t)e^{j2\pi f_C t}] = x(t)e^{j2\pi f_C t} + x^*(t)e^{-j2\pi f_C t}, \tag{2.3}$$

which confirms that the information content of original $z(t)$ exists in both of the mirroring signal components. [75]

In complex domain, frequency translation can be done also asymmetrically. Mixing the baseband information signal with complex exponential $e^{j2\pi f_C t}$ shifts the original signal to center frequency f_C. Ideally, in this case mirror image doesn't appear around $-f_C$ as graphically illustrated in Figure 2.3. Due to this property, complex mixers are often also called image rejection or quadrature mixers. Asymmetricity in the output signal spec-

trum of course indicates the complex nature of the signal at the same time. These kinds of signals are usually called analytic signals. Taking real part of analytic signal creates the mirror image for the signal components. [48]

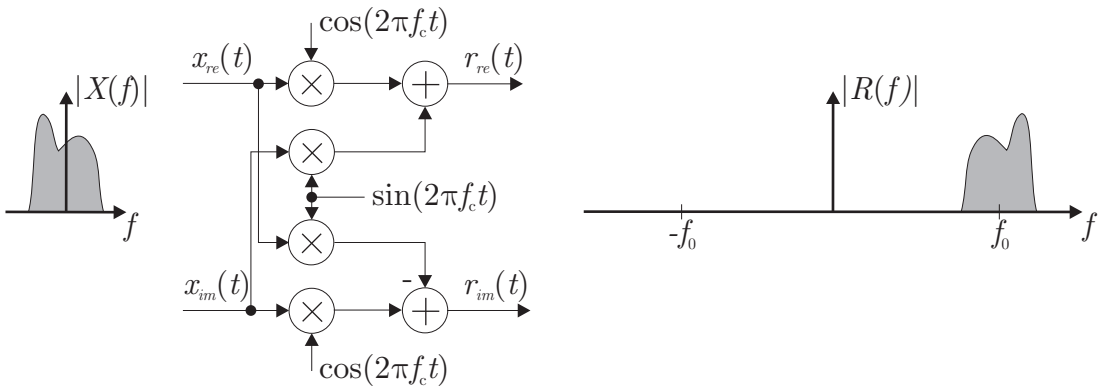

Figure 2.3 *Analytic bandpass signal and asymmetric frequency translation, modified from [48].*

On the other hand, this kind of asymmetric analytic signals can be obtained with Hilbert transformation (HT) [16], [43] as graphically illustrated in Figure 2.4. The Hilbert filter has a frequency response

$$H_{HT}(f) = -j\,\mathrm{sgn}(f) = \begin{cases} -j & \text{for} \quad f > 0 \\ 0 & \text{for} \quad f = 0 \\ j & \text{for} \quad f < 0. \end{cases} \tag{2.4}$$

Thus, the filter has an allpass response, with +90° phase shift for the negative frequencies and –90° for the positive ones. Exciting this filter with $r(t)$ of (2.3) gives

$$\begin{aligned} \hat{r}(t) &= -jz(t)e^{j2\pi f_C t} + jz^*(t)e^{-j2\pi f_C t} \\ &= 2z_{re}(t)\sin(2\pi f_C t) + 2z_{im}(t)\cos(2\pi f_C t). \end{aligned} \tag{2.5}$$

Now the analytic signal can be formed as $r(t) + j\hat{r}(t)$ having a Fourier transform $[1 + jH_{HT}(f)]R(f)$, where

$$1 + jH_{HT}(f) = 1 + j(-j\,\mathrm{sgn}(f)) = \begin{cases} 2 & \text{for} \quad f > 0 \\ 1 & \text{for} \quad f = 0 \\ 0 & \text{for} \quad f < 0. \end{cases} \tag{2.6}$$

This result shows that the energy on the negative frequencies in original symmetric spectrum $R(f)$ is nulled. At the same time, signal content on the positive frequencies

has gain of 2, thus maintaining the overall energy of the signal on the same level as before filtering. [75]

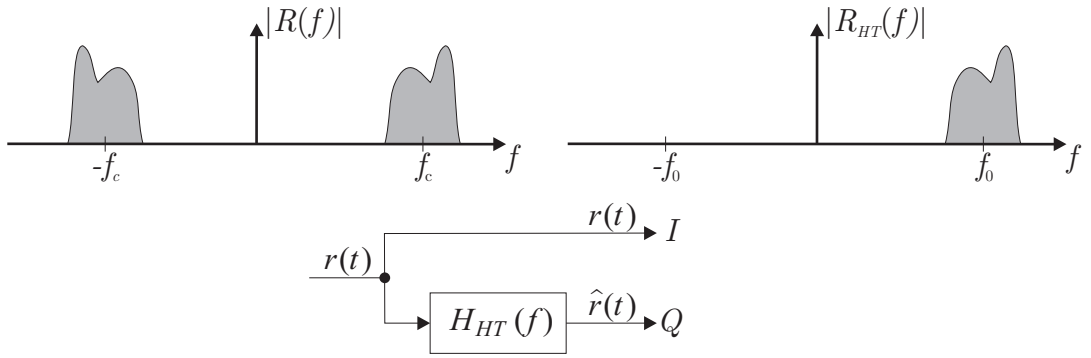

Figure 2.4 *Spectra of original* $r(t)$ *and analytic* $r_{HT}(t) = r(t) + j\hat{r}(t)$ *with the filter structure employing a Hilbert transformer.*

2.1.3. Complex Filtering

A filter having a complex valued impulse response, and thus complex valued transfer function coefficients, is called a complex filter. This kind of filter has a benefit of not being restricted to a symmetric magnitude response around DC. In other words, the poles and zeros of the filter don't have to appear in complex conjugate pairs. [20], [30], [45], [69]

Now concentrating on discrete-time filters, a general complex impulse response is of a form

$$h_{comp}(k) = h_{re}(k) + jh_{im}(k), \tag{2.7}$$

where $h_{re}(k)$ and $h_{im}(k)$ are real valued functions presenting the real and the imaginary part of $h_{comp}(k)$. If this filter is applied on a complex discrete-time signal $x(k) = x_{re}(k) + jx_{im}(k)$ the output becomes

$$\begin{aligned} y(k) &= h_{comp}(k) * x(k) \\ &= h_{re}(k) * x_{re}(k) - h_{im}(k) * x_{im}(k) + j(h_{re}(k) * x_{im}(k) + h_{im}(k) * x_{re}(k)), \end{aligned} \tag{2.8}$$

where the operations between the terms are convolutions in case of a multi-tap filter and reduce to scalar multiplications if the filter length is one. This assumption is carried throughout the thesis. The equation (2.8) shows that a real implementation of a complex filter can be done with four real-valued filters. Two of them are acting on the I rail carrying the real part of the signal and the other two on the Q rail presenting the imaginary

part. This is illustrated in Figure 2.5, where in case of ideal matching of the branch transfer functions $H_{re,1}[z] = H_{re,2}[z]$ and $H_{im,1}[z] = H_{im,2}[z]$ in *Z*-domain. [30] This structure reduces to a multiplication of two complex-valued constants in the case of all filters having only 1-tap impulse response, thus being scalar. Similar principles can be applied for continuous-time filters and signals by replacing the terms in *Z*-domain equations by corresponding *S*-domain functions [45], [69].

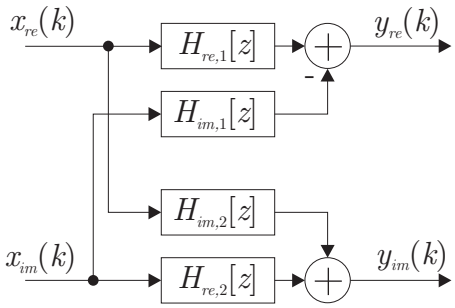

Figure 2.5 *Complex filter $H_{comp}[z]$ with a complex input $x(k)$ implemented with parallel real signals and real filters.*

A complex bandpass filter can be designed either with a real lowpass prototype, which will be then shifted on the desired center frequency, or by a direct method principally similar to ones applied for the real filters. [45] In case of finite-impulse-response (FIR) filters, the frequency shift can be realized simply by mixing the filter coefficients with a complex exponential of desired center frequency, following the same principle that was presented for information signals.

2.1.4. Mismatches in Complex Systems

Based on the published works, the error between the I and Q branch gains, usually referred to as a mismatch, causes mirror frequency interference in complex systems [20], [30], [33], [34], [45], [55], [72], [75], [76]. In Sub-section 2.1.2, it was noted that the I and Q components do not interfere each other, if the ideal 90° phase difference is maintained between the carriers. However, if this ideal quadrature separation is lost, e.g., due to circuit nonidealities, the components mix into each other causing so-called mirror frequency interference.

The interference is due to a conjugate response from the input to the output of the mismatched system [33], [72], [75]. The level of interference is proportional to the differential part of the deviation of the I and Q gains from the nominal values. In general, the gains are assumed complex-valued, thus having a certain magnitude and phase. So-called common

mode error, which includes the parallel part of the error, is only scaling the output signal and doesn't cause harmful interference. These phenomena are graphically demonstrated in Figure 2.6, where the nominal-value term $H_{nom}[z]$ is assumed to include also the common-mode error of the gain. The thicker lines in Figure 2.6 denote complex-valued signals. This notation will be used throughout the thesis to separate real and complex paths and operations.

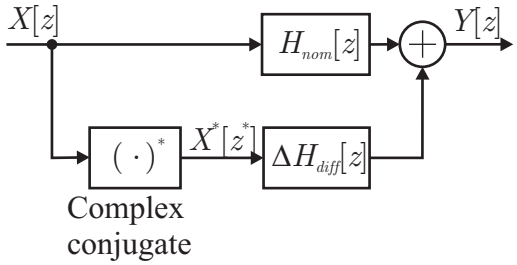

Figure 2.6 *Complex conjugate response, which generates mirror frequency interference due to a differential mismatch between the I and Q branches.*

The principle in the above figure can also be presented as a following equation:

$$Y[z] = H_{nom}[z]X[z] + \Delta H_{diff}[z]X^*[z^*]. \tag{2.9}$$

Subsequently, the common-mode term and differential error term can be derived from the actual realized values of the four real filters employed in the complex filter structure. In other words, the assumptions $H_{re,1}[z] = H_{re,2}[z]$ and $H_{im,1}[z] = H_{im,2}[z]$ do not hold anymore. From which follows, that [33]

$$H_{nom}[z] = \frac{H_{re,1}[z] + H_{re,2}[z]}{2} + j\frac{H_{im,1}[z] + H_{im,2}[z]}{2} \tag{2.10}$$

and

$$\Delta H_{diff}[z] = \frac{H_{re,1}[z] - H_{re,2}[z]}{2} + j\frac{H_{im,1}[z] - H_{im,2}[z]}{2}. \tag{2.11}$$

The effect of the conjugate response in the spectrum of a complex exponential is shown in Figure 2.7. The extent of the interference is usually measured with image attenuation,

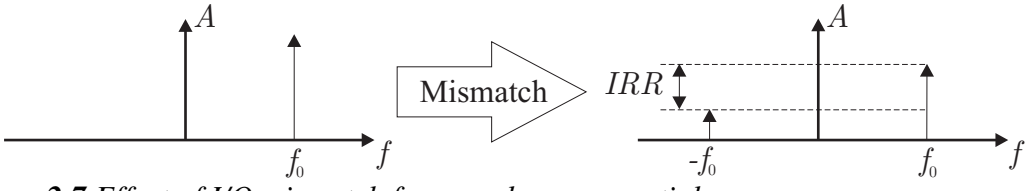

Figure 2.7 *Effect of I/Q mismatch for complex exponential.*

also known as a image rejection ratio (IRR), which is defined as a ratio of the powers of the original signal component and the mirror interference component [75]. With the previous notation, IRR can be defined with substitution $z \leftarrow e^{j2\pi ft}$, where f is frequency in hertz, as

$$IRR(e^{j2\pi fT_S}) = 10\log_{10}\left|\frac{H_{nom}(e^{j2\pi fT_S})}{\Delta H_{diff}(e^{j2\pi fT_S})}\right|^2, \tag{2.12}$$

which generally allows also frequency-dependent variations.

Numerous methods have been presented to mitigate or compensate the mirror-frequency interference and thus improve the IRR on receiver side. Some of the techniques are directed only against frequency-independent interference, see e.g., [3], [73] and [77]. On the other hand, also algorithms able to cope with frequency-dependency are presented, e.g., in [4], [73], [75] and [84].

2.2. Superheterodyne Receiver

Conventional and widely adopted architecture choice for radio receiver implementations for some time has been superheterodyne. The receiver employs an analog radio frequency bandpass (BP) filter for the coarse system selection and removal of out-of-band signal energy. After amplifying the signal with a low-noise amplifier, further filtering is done to guarantee adequate image band attenuation. Next, this RF signal is frequency-translated with a real mixer to an intermediate frequency. The real mixing operation namely creates the need for strict image-filtering on preceding stages. On the IF, the specific channel separation is done with analog bandpass filter (BPF). Tunability of the mixer, which is used to select specific channel, enables the use of fixed filter, making efficient implementation possible. Final down-conversion is done with a quadrature I/Q mixer. The baseband signal, including only the desired channel is then finally converted to digital domain. [44], [48], [76]

Placing the selectivity of the receiver on the analog side eases the requirements for the ADC by reducing signal dynamics. In addition, bandwidth of the converted signal is limited to the one of the desired channel. Thus, fairly simple traditional Nyquist converter or lowpass ΣΔ converter can be used. The noise shaping ΣΔ converter allows more efficient use of the available precision, but especially in case of wideband information

signals, demanded oversampling ratios can set challenging requirements for the sampling rate. [42], [80]

The main drawbacks in superheterodyne receiver are high number of components, high power consumption and heavy RF processing in the front-end limiting the flexibility. Thus, architectures with better integration characteristics and more simplified RF parts are favored in modern solutions. The main themes in the recent development have been exactly high integrability and flexibility with increasing role of digital signal processing. [76]

2.3. Direct-Conversion Receiver

Direct-conversion, or zero-IF, receiver was proposed [1] to reduce the heavy RF processing and the number of discrete components utilized in the superheterodyne. In this way, also the integrability of the receiver could be improved. The target is achieved by converting the RF signal straight to baseband with quadrature mixer. Coarse preselection filter is used on the RF but most of the selectivity is designed to baseband with lowpass channel-selection filter. The choice of the desired channel is done by tuning the local oscillator (LO) frequency of the down-conversion mixer.

Since the IF is effectively zero, the image signal is actually a mirror copy of the desired signal itself. This alleviates the image rejection requirements because there is practically no risk of a blocking signal with high relative power compared to the desired channel. Image rejection ratios of 25 – 40 dB are considered to keep the (self-)image interference on tolerable level [1], [55], [56]. However, in a wideband receiver where the final selectivity is realized with digital filters, mirror band signal might have notably larger power levels. This is because the interesting signal on the wide converted band might have a non-zero center frequency; this case will be discussed further when considering the IF-sampling receiver (Section 2.4). Wideband receiver also sets demands for the dynamics and the sampling rate (depending on the converted bandwidth) of the converter. [76] The problem has been addressed especially concerning emerging cognitive [83] and software radio [79] implementations. The dynamic range problem is due to the fact that the band can contain significantly stronger signals, as mentioned above, compared to desired one, and the ADC should be able to stretch the quantization range according to them, while still offering enough accuracy for the weak signal.

A/D conversion is done on the baseband as in heterodyne receiver and thus the demands on the converter are similar to ones addressed in Section 2.2. The more flexible structure of the direct-conversion receiver eases the transitions between radio standards. This is done again by tuning the LO frequency and the lowpass filter (LPF) bandwidth. Based on this property flexible software controlled architectures have been proposed for multistandard receivers utilizing the direct conversion principle [9], [10], [59], [63].

On the other hand, usage of zero-IF introduces also some problems. The most well known of them are DC offsets, LO leakage, even-order nonlinearity and flicker noise. All these phenomena generate interference on low frequencies. However, several techniques have been proposed to mitigate these issues [48], [55], [76]. Thus, direct-conversion receivers have been widely adopted to use, e.g., in mobile terminals.

2.4. IF-Sampling Receiver

To avoid the issues with direct conversion and baseband A/D conversion, mentioned in Section 2.3, the signal digitization has been proposed to be done on non-zero, but low IF [19], [20], [30], [34]. In this kind of structure, the final down-conversion is done in digital domain. Using non-zero IF allows more variation in the architecture but in [48] the preferred version employs similar analog front-end compared to direct-conversion receiver, the only difference being that the frequency shift is done to IF. Because the IF is assumed to be low, the filtering can be done with LPF. Usually intermediate frequencies in the order of a couple times the channel bandwidth are considered low in this sense. Though, the IF can be also higher, e.g. in wideband receivers where broader band is desired for the converted channels [48].

On the other hand, with non-zero IF the mirror band of the desired channel is no more the self-image of the signal. The image signal being non-controlled, large power fluctuations are possible. In some scenarios, the image band can be tens of decibels stronger than the desired information channel. With low IF the image signal often originates from the channels of the same system as the desired one, and the system specifications limit the power variations to 10 – 25 dB. In case of higher IF the inter-system image signals can be even 50 – 100 dB stronger, demanding remarkable image rejection in order to prevent the loss of the desired information content. [76]

Extending the converted bandwidth increases the requirements for the ADC, but with relatively small IF the sampling rate demands are usually moderate. Extended channel filter passband also allows non-desired signals to enter the ADC, thus adding possible dynamics of the converted signal. Thus, higher demands are set for the dynamic range of the converter and, on the other hand, for the preceding gain control to prevent overloading. However, the LPF can be replaced with complex BPF to reduce out-of-band energy, if more controlled dynamics are desired [42], [80]. On the other hand, selection of relatively high IF sets strict requirements for the sampling properties of the ADCs. In wideband IF receiver similar challenges are set for the A/D converter as was discussed in case of the wideband direct-conversion receiver (Section 2.3). In addition, more attention should be paid to the speed (the sampling rate) of the converter, depending on the choice of the applied IF.

On the IF, The digitization of the received signal can be done with a Nyquist converter, when the whole converted band is available in the digital domain for a selection of the desired channel. In that way, the available precision and the quantization noise of the converter is divided equally for the Nyquist band. The other possibility is to employ a bandpass ΣΔ converter for the digitization. This, in a sense, allows more efficient use of the ADC resources because the out-of-band noise levels are not interesting. Thus, the precision could be, so to say, concentrated on the desired band. Either a real [35], [54], [62] or a complex [6], [30], [34] bandpass modulator can be used, while the complex one having some benefits over the real implementation [38]. The receiver structure employing a complex version of the modulator is shown in Figure 2.8. The specifics of the ΣΔ converters will be discussed later in this thesis.

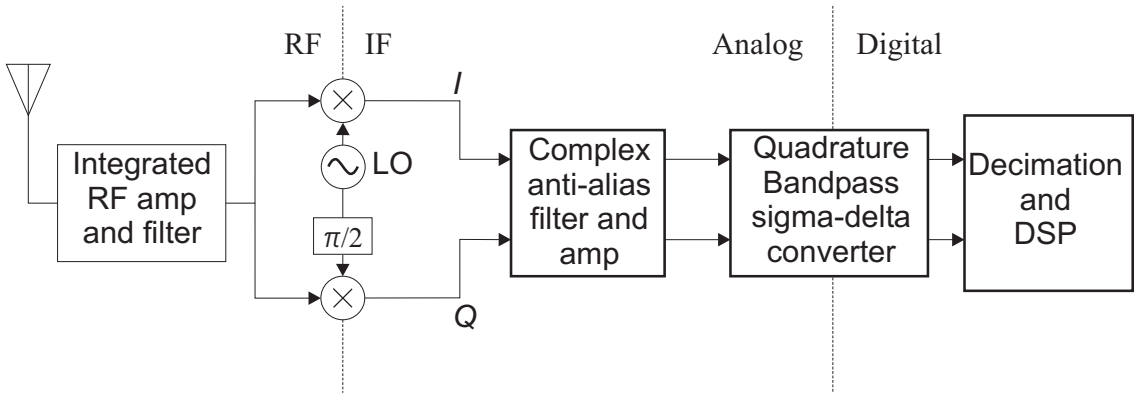

Figure 2.8 *IF receiver employing a quadrature bandpass ΣΔ ADC for signal digitization [34].*

The IF receiver implementation offers more flexibility compared to traditional superheterodyne. In addition to direct-conversion based multi-mode receivers, similar IF architectures have been proposed [29], [61] exploiting these features.

2.5. Direct-Sampling Architecture

Ultimate solution for the flexibility and simplifying the analog radio front-end would be direct RF-sampling. In the direct sampling architecture, the received signal is sampled straight from the antenna after some anti-alias filtering. Rest of the receiver processing and selectivity is then implemented in either analog discrete-time or digital domain. Texas Instruments has proposed and manufactured a discrete-time processor based RF sampling receiver utilizing so-called sampling mixer [9], [10], [27], [50]. Similar kind of structure has also been proposed in [30]. On the other hand, also an idea of ΣΔ modulator with RF-sampling inside the modulator loop has been presented [82].

The biggest challenge for direct sampling has been the sampling jitter, which easily distorts the signal on high frequencies such as the RF. In addition, noise aliasing should be taken into account when designing sub-sampling receivers. [56] In many ways, the direct sampling is the most challenging setup when considering the A/D conversion. Drive towards ultra-high speed samplers at the range of 100 GHz has been reported [42], but at this point sub-sampling seems to be the only reasonable possibility. At the same time, the wider the sampled bandwidth, the higher are the dynamics of the signal thus setting strict requirements also for the dynamic range of the converter and the preceding gain control, as mentioned already when discussing the IF receiver.

3. ΣΔ CONVERTER BASICS

When considering the concept of quadrature ΣΔ modulator, it is essential to understand the background of the ΣΔ principle and the modulators. The real ΣΔ modulator has a symmetric frequency response – either lowpass or bandpass. In addition, there are several different implementation methods presented in the existing scientific literature, e.g., [2], [7], [68].

In this chapter, the basics of ΣΔ modulation are presented. In addition, some comparisons are done and related implementation possibilities are taken into account. The main objective is to give an adequate technical background for the reader to understand the principles related to the quadrature ΣΔ modulator. Also, the farrago of terms and notation used in the existing scientific literature – and later in the thesis – will be clarified.

3.1. Quantization Process

Quantization is a process where the continuous amplitude values of the (analog) signal are represented with a finite set of codewords. This is usually done by choosing the nearest possible output code for the input value at hand at any given time instance. In digital communications, quantization is needed on the receiver side, when the analog input signal is digitized for the following stages. Generally, digital signals are represented with bits, thus enabling only finite range of amplitude values.

Transforming continuous amplitude range to the set of discrete values is always nonlinear operation. In other words, more than one input values are mapped to the same output code. A typical quantization scheme is demonstrated with the help of an ideal unipolar 3-bit ADC in Figure 3.1. The codewords are designed in such a way, that the quantization error is zero in the center of each interval. These are marked with dots in Figure 3.1. The center corresponding to the zero-error leads straightforwardly to the conclusion that the error is always between −0.5 LSB and +0.5 LSB, where LSB corresponds to equivalent range of the least significant bit. It is also worthwhile to note, that

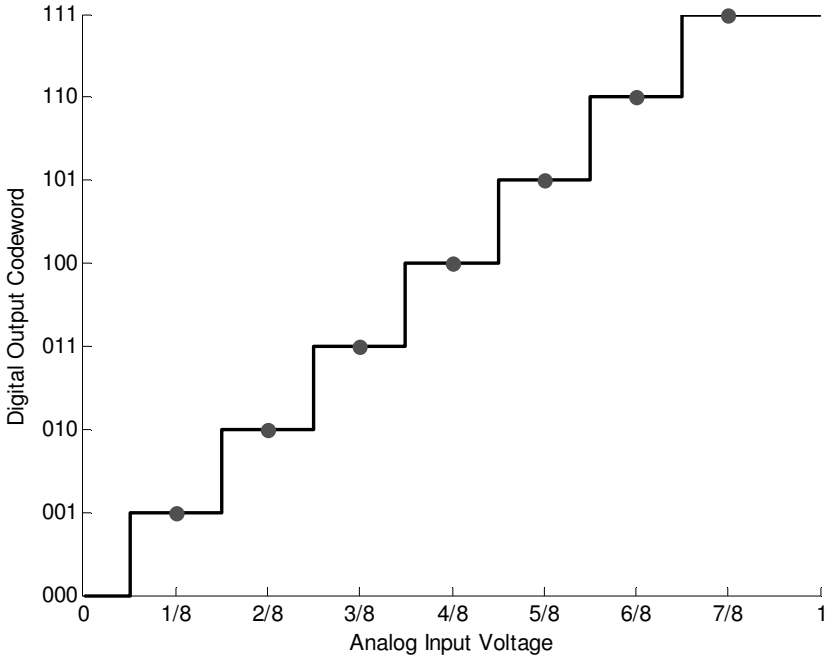

Figure 3.1 *Quantization levels of ideal unipolar 3-bit ADC.*

the width of the first code is only 0.5 LSB and correspondingly the last interval is 1.5 LSB. This is done to make the error zero-mean. Without this 0.5 LSB shift the potential error range would from 0 LSB to +1 LSB.

With practical waveforms, also the negative voltages need to be quantized. This is why bipolar quantizer are widely adopted to use instead of above shown unipolar system [2]. The simplest example of a bipolar quantizer is a sign operation, which corresponds to the 1-bit quantization. The other bit results from a negative input and the other from a positive one. Actually, this 1-bit quantizer is used in many ΣΔ solutions, when the quantization precision can be enhanced in other ways, as will be discussed in the next section.

On the other hand, the intervals of the codewords don't need to be uniform. A few non-uniform structures, such as logarithmic [25] and floating point [52] ADCs, are give in the literature. These are also adopted to use in certain applications, but are rare in communication systems.

The quantization error introduces always some loss of information, which is usually referred as quantization noise. This is the case even in the ideal converter as seen above. The effect of the noise is traditionally presented in proportion to the original signal power by the signal-to-noise ratio (SNR). In case of an ideal quantizer the SNR in decibels is defined as [36]

$$SNR = 20\log_{10}\frac{V_{in(rms)}}{V_{Q(rms)}}, \tag{3.1}$$

where $V_{in(rms)}$ is the root-mean-square value of the original input signal and $V_{Q(rms)}$ is the corresponding value of the quantization error. In the special case of a sinusoidal input, (3.1) can be simplified to the well-known form of

$$SNR = 6.02b + 1.76, \tag{3.2}$$

where b is the number of the available quantization bits. [36] Thus, it can be given as a rule of thumb, that 1-bit increase to the used bits gives 6 dB higher SNR.

Next, if we take oversampling and post-quantization filtering into account, the SNR can usually be improved. This is because the quantization noise is spread on a wider frequency band than the interesting signal and the out-of-band noise can be attenuated without loss of information. Using higher sampling rate means that the noise is spread on even wider band and therefore a greater part of it can be filtered out. This gain can be included in the SNR as

$$SNR = 6.02b + 1.76 + 10\log_{10}\left(\frac{f_S}{2f_B}\right), \tag{3.3}$$

where, f_S is the sampling frequency and f_B is useful signal bandwidth. This shows that increasing the sampling frequency improves the SNR. However, it should be noted that in real-life converters there is a tradeoff between the speed and the resolution. The fast ADCs tend to have lower resolution, and vice versa.

3.2. ΣΔ Principle

The principle of oversampling ADC with negative feedback has been invented decades ago and is still being developed further by scientists all over the world. Today's state-of-the-art converters have come a long way from the first ADCs employing ΣΔ principle in the 1960s. There is quite broad selection of ΣΔ oriented publications in literature since 1960s and early development phases have also been documented in a comprehensive manner, e.g., in [2], [7] and [68]. The discussion in this section is based on [2].

The origin of modern ΣΔ modulation is in delta modulation and differential pulse-code modulation (PCM). Delta modulation was invented in ITT laboratories in France in

1946, as was also the classical version of the PCM. Differential PCM system was patented in 1950 by Bell Telephone Labs.

In delta modulation, the term delta refers to transmitting only the changes between the consecutive samples. The delta modulator employs a 1-bit ADC and the feedback signal is fed through 1-bit digital-to-analog converter (DAC), whereafter it is subtracted from the input after an integrator as shown in Figure 3.2. In this kind of system output "1" means that input signal amplitude is raising and "0" indicates negative direction. Differential PCM uses same kind of structure as delta modulation, only difference being that single-bit ADC and DAC have been replaced with their multi-bit flash counterparts.

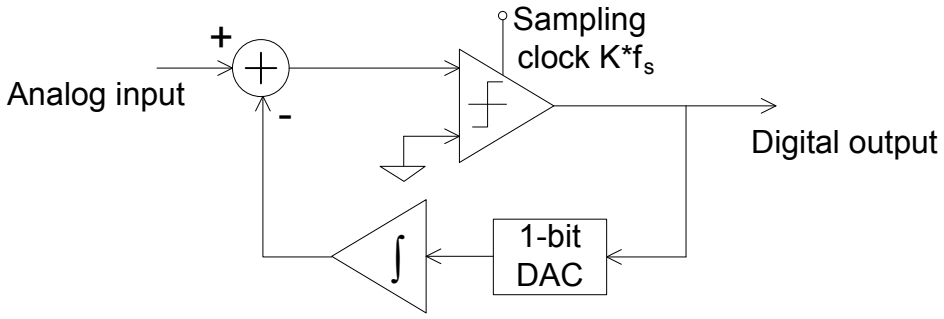

Figure 3.2 *Delta modulator block diagram [2].*

Since the output of the modulator depends only on the direction of change in the input signal, clipping effect can be avoided with a big enough step size and sampling rate. For that reason delta and differential PCM modulators usually demand sampling rates as high as 20 times the bandwidth of the interesting signal.

In the modern ΣΔ modulator, the integrator block does not operate on the feedback loop, but is transferred to the forward branch and thus operates on the error signal. Block diagram of ΣΔ modulator is shown in Figure 3.3. The publications of Inose and Yasuda [28] and van de Plassche [78] can be mentioned as examples of the earlier work on the topic.

In this kind of structure the integrator shapes quantization noise away from the band of interest by processing the error of the ADC and the DAC compared to the input. In this part the oversampling becomes significant, because in traditional Nyquist rate converter there is no extra frequency band where the noise could be pushed. With oversampling used in ΣΔ modulators there is always more band available than the one of the desired

signal. This extra band can be used for the noise spectrum shaping and thus the noise can be filtered out in digital domain after the conversion. Thus, it is possible to cope even with simple 1-bit quantization, if there is enough oversampling. The exact sampling speed requirements are of course application specific. After the filtering, the output signal can be decimated to lower rate or even down to the Nyquist rate, depending on the forthcoming signal processing stages.

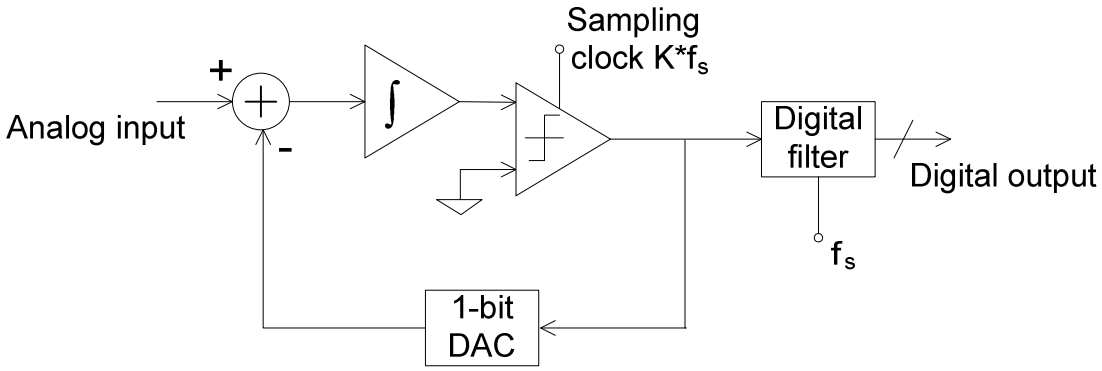

Figure 3.3 *Block diagram of ΣΔ converter (first-order structure with 1-bit quantization) [2].*

There's also been significant amount of discussion about the name of the described technique, whether it should be delta-sigma or sigma-delta. Original naming from 1962 is delta-sigma, because it was based on delta modulation. In 1970s AT&T adopted the term sigma-delta to use, though, term sigma being used as an adjective specifying the variant of delta modulation in question. Since that, both the terms have been used, sometimes even in confusing manner. Dan Sheingold reasons in [2] that in functional hierarchy the term sigma-delta describes the actions of the modulator, which computes the integral or summation of the difference signal as shown in Figure 3.4. The author's opinion is that this term describes the system best and so sigma-delta is adopted to use throughout this thesis.

Another point worth clarifying at this stage is that term ΣΔ modulator refers only to the actual feedback structure performing the quantization. At the same time ΣΔ converter

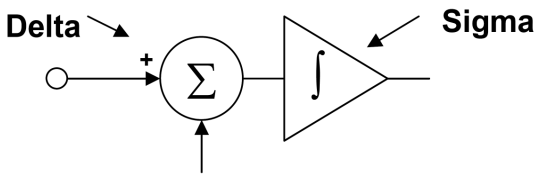

Figure 3.4 *Sigma-delta means an integral of the difference [2].*

consists of a ΣΔ modulator, a digital filter removing excess out-of-band noise and a decimator.

Bryant describes quantization noise of ΣΔ converter in [14] in such a manner that it can be understood without going to detailed mathematics. If oversampling would be the only way to reduce quantization noise, we would have to oversample the signal with a factor of 2^{2N} to obtain N-bit increase in resolution. In ΣΔ principle noise shaping properties fortunately ease the situation. The error signal, which is the difference of original input and the output of the feedback DAC, is fed to the forward integrator. In the integrator output, the noise is pushed towards the high end of Nyquist band, when considering lowpass type of ΣΔ modulator. The noise spectra of traditional Nyquist ADC, oversampling traditional ADC and oversampling ΣΔ ADC are compared in Figure 3.5.

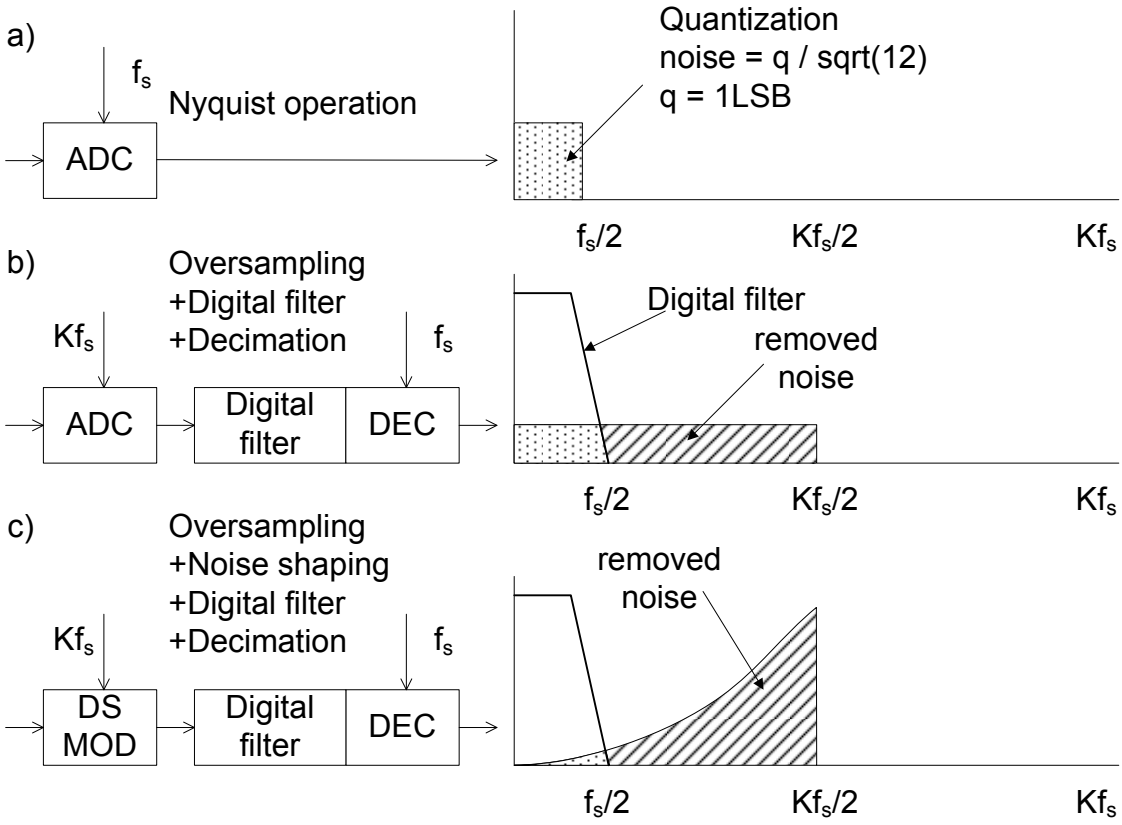

Figure 3.5 *Noise spectra of a) a Nyquist ADC, b) an oversampling traditional ADC and c) an oversampling ΣΔ ADC [2].*

Often the transfer function of the modulator is expressed in two parts. The noise shaping is described in noise transfer function (NTF), usually having one or more zeros on the band of interest. The behavior of desired signal itself depends on the signal transfer

function (STF), usually having unity gain. With these definitions the z-domain output of the converter can be described as

$$V[z] = STF[z]U[z] + NTF[z]E[z], \tag{3.4}$$

where $U[z]$, $E[z]$, $V[z]$, $STF[z]$ and $NTF[z]$ refer to the input, the quantization error, the output, the signal transfer function and the noise transfer function, respectively. [7]

3.3. Lowpass ΣΔ Modulator

A discrete-time block diagram for first-order feedback lowpass ΣΔ modulator is presented in Figure 3.6 to clarify the main principle. The quantizer is replaced with an additive noise source and the DAC is assumed ideal and thus replaced by a unity gain. For analysis purposes, the quantization error inside the modulator loop is assumed to be additive white Gaussian noise (AWGN) and to be uncorrelated with the input [68]. The assumption is not exactly accurate, as Gray found in [23] that the error actually is correlated with the input, but the uncorrelatedness offers a valid enough base for the analysis to be adopted in use.

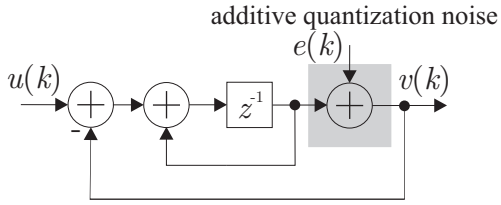

Figure 3.6 *Discrete-time linearized model of the first-order lowpass ΣΔ modulator [7].*

Based on the model the transfer function can be derived giving

$$V[z] = z^{-1}U[z] + (1 - z^{-1})E[z]. \tag{3.5}$$

It can be seen from the transfer function that for discussed structure $STF[z] = z^{-1}$ and $NTF[z] = 1 - z^{-1}$. Thus, the desired signal is only delayed on the way from input to output and some filtered noise is added to the signal. [7] NTF amplitude response is plotted on the left in Figure 3.7 and the related positions of the modulator zero and pole are given in the following zero-pole plot on the right side in Figure 3.7.

From the amplitude response, it is clear that the noise signal has attenuation at level of −60 dB on the zero-frequency. The zero-gain level, which would correspond to nonshaped noise is roughly at frequencies ± 0.166 relative to f_S. Thus, the band of 0.33

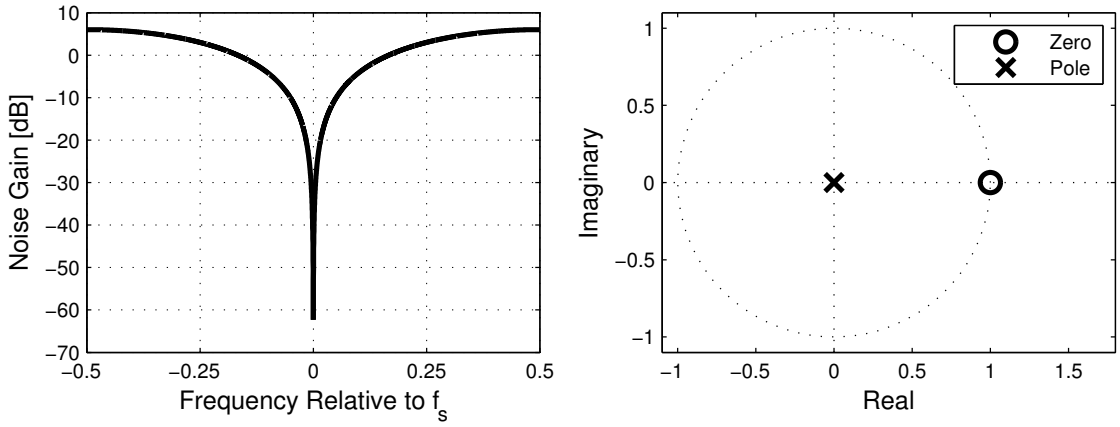

Figure 3.7 *Amplitude response (left) and zero-pole plot (right) of the NTF for a first-order lowpass ΣΔ modulator.*

relative to f_S has only attenuated noise present. The zero-pole plot confirms that the modulator zero lies at DC on the unit circle and the pole is in origin.

For a more detailed mathematical perspective, interested reader is advised to consult [24]. Therein, Gray gives a precise walk through the effects of quantization in single loop, two-stage and second-order ΣΔ converters. He also expands the discussion to the effects of dithering, higher-order modulation, leaky integration and multi-bit ADCs, in respective order.

In [7] Aziz et. al. have given the formulas for inband noise power and signal-to-noise ratio in case of single-bit quantizer and single-bit DAC assuming high enough oversampling ratio (OSR) to shape noise effectively. Reproducing their findings, the output inband noise power of first-order lowpass ΣΔ modulator becomes

$$\sigma_{ey}^2 = \sigma_e^2 \frac{\pi^2}{3}\left(\frac{2f_B}{f_S}\right)^3, \tag{3.6}$$

where σ_e^2 corresponds to the whole band quantization noise power, f_B and f_S are signal band and the sampling frequencies, respectively. This leads to the inband signal-to-noise ratio of

$$SNR = 10\log_{10}(\sigma_x^2) - 10\log_{10}(\sigma_e^2) - 10\log_{10}\left(\frac{\pi^2}{3}\right) + 30\log_{10}\left(\frac{f_s}{2f_B}\right) \tag{3.7}$$

in decibels, where σ_x^2 is desired signal power. If we still denote the oversampling ratio with $f_S \,/\, 2f_B = 2^r$ the equation becomes

$$SNR = 10\log_{10}(\sigma_x^2) - 10\log_{10}(\sigma_e^2) - 10\log_{10}\left(\frac{\pi^2}{3}\right) + 9.03r, \tag{3.8}$$

which in addition to analysis by Aziz et al. can be simplified to

$$SNR = 6.02b + 4.76 - CF_{dB} - 10\log_{10}\left(\frac{\pi^2}{3}\right) + 9.03r \tag{3.9}$$

by defining quantization noise power with a number of used bits b and crest factor CF_{dB} in decibels. Crest factor defines how much of the quantizer full-scale range can be utilized. As an example, the crest value for a sinusoidal signal is $CF_{dB} = 3\ \mathrm{dB}$. From (3.8) and (3.9) it can be seen that for every doubling of oversampling ratio, corresponding to increment of r by one, the SNR improves by 9 dB, which means 1.5 bits of effective resolution.

The effect of the NTF is confirmed by simulation with a single sine-wave input in Figure 3.8. The STF is assumed frequency-flat with unity response. In simulations, the quantization error is modeled as AWGN, as was the assumption deriving the linear model for the modulator. Variance of the noise is equivalent to the one of the theoretical quantization error produced by a 1-bit quantization. Thus, it is corresponding to the full-band SNR according to (3.2) of $6.02 \times 1 + 1.76 = 7.76\ \mathrm{dB}$. The plots clearly show the shaped noise spectrum. Highlighted 20 dB and 40 dB per decade slopes are consistent with the theoretical NTFs for first and second-order [68]. Noise floor is limited to −80 dB due to limited simulation precision and FFT properties.

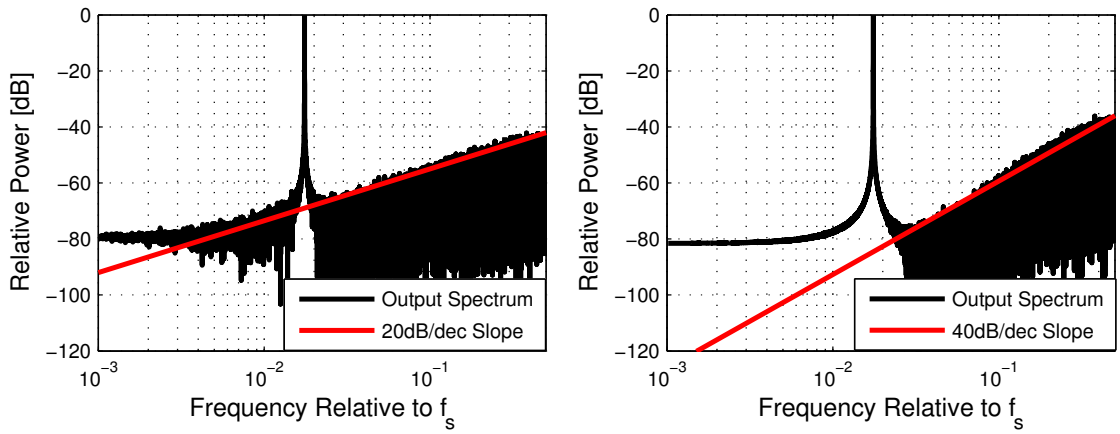

Figure 3.8 *Simulated output spectrum for the first- (left) and the second-order (right) lowpass ΣΔ modulators with a sine-wave input and an AWGN modeled quantization error.*

3.4. Real Bandpass ΣΔ Modulator

In a lowpass type ΣΔ modulator the quantization noise is pushed away from the low frequencies towards the high end of Nyquist band. Correspondingly, a bandpass converter shapes the noise towards Nyquist frequency and the DC, and thus away from the band of interest in the middle of Nyquist band. [2] This can be particularly useful in case of a low IF or an IF receiver.

The most well-known method to design a bandpass ΣΔ modulator is to transform a lowpass prototype to a nonzero center frequency. This can be done, e.g., with $z^{-1} \rightarrow -z^{-2}$ transformation. In other words, an additional delay is added to the integrator inside the modulator loop and the sign of the feedback is inversed. The resulting bandpass structure is presented in Figure 3.9. With described method the center frequency of the noise notch becomes $f_S / 4$. [62], [67]

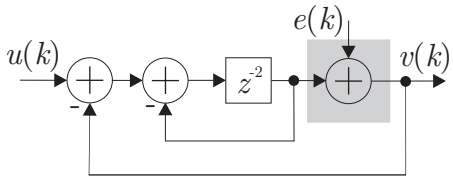

Figure 3.9 *Discrete-time linearized model of a first-order BP ΣΔ modulator [62].*

If the noise shaping characteristics are desired to be such that the notch frequency of the bandpass modulator differs from the quarter of the sampling frequency, more sophisticated transformation method has to be used. Tunable bandpass modulator based on switched-capacitor resonator was presented in [15]. The basic structure of the modulator is similar to one presented in Figure 3.9, but additional summation and tuning parameter is included in order to make arbitrary notch frequency possible. This is shown in Figure 3.10.

Bandpass transformation doubles the modulator order, which can be seen also from the zero-pole plot in the right-hand plot of Figure 3.11 as a doubled number of zeros and

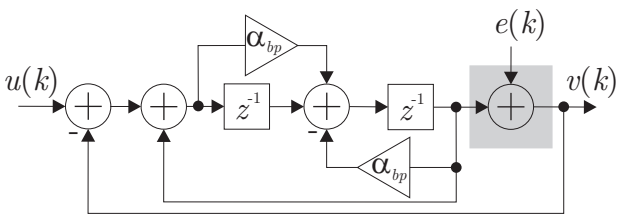

Figure 3.10 *Discrete-time linearized model of a first-order tunable BP ΣΔ modulator [15].*

poles. The corresponding NTF response is given on the left in Figure 3.11. The two zeros can be straightforwardly seen as two frequency-symmetric NTF notches in the amplitude response. The zeros – and the notches – are placed at a frequency ± 0.35 relative to the sampling frequency. Thus, in principle the number of active components is also doubled. However, in practice extra components compared to the lowpass receiver can be avoided by simplifying the overall receiver structure when utilizing a bandpass modulator. [62]

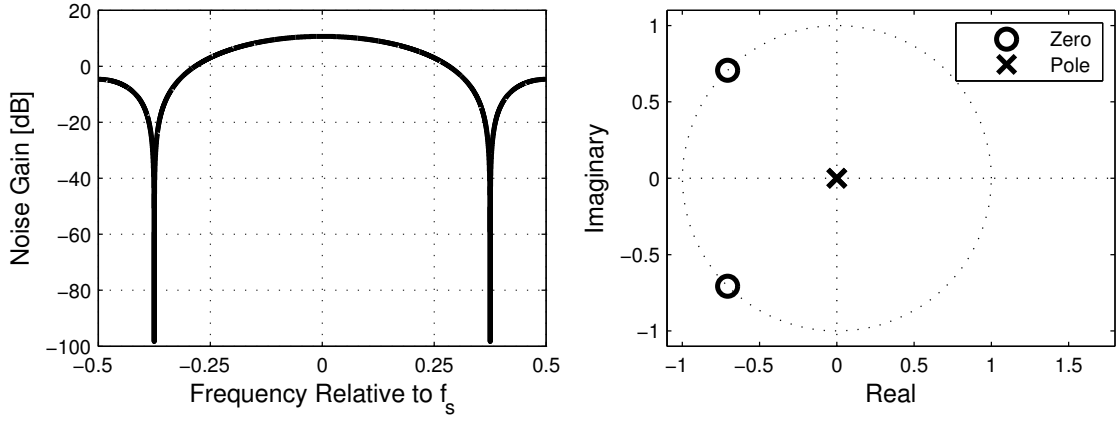

Figure 3.11 *Amplitude response (left) and zero-pole plot (right) of the NTF for a second-order real BP ΣΔ modulator.*

Doubling the modulator order also means that, when considering asymmetric complex bandpass signal to be converted, only half of the modulator zeros are on the desired band. This affects the expected SNR values on given modulator order when compared to the lowpass case. For lowpass modulator increasing the oversampling ratio by an octave gives $6L + 3$ dB better SNR, L being the modulator order. In case of bandpass ΣΔ modulator the corresponding value is $3L + 3$ dB, from where can be confirmed that double-order modulator is indeed needed in order to get similar enhancement in SNR. [35], [67]

As in the case of lowpass modulator, the noise shaping effect was confirmed by a simulation. The full-band signal-to-noise-ratio, and thus the noise variance, is again equivalent to the theoretical full-band SNR of 7.76 dB. The NTF applied in the simulation corresponds to the one demonstrated in Figure 3.11. Based on this, an output spectrum of the real bandpass modulator excited with sine-wave in Figure 3.12 verifies the NTF behavior.

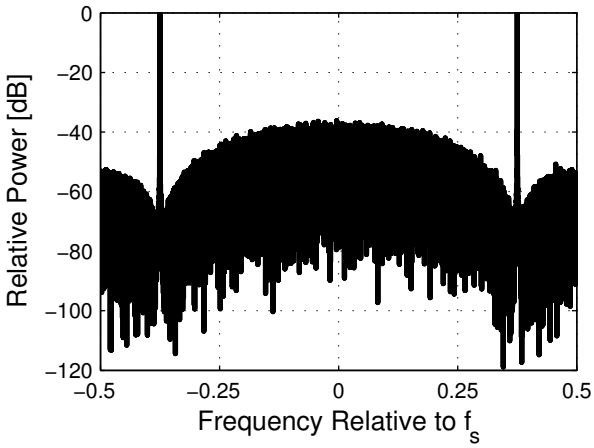

Figure 3.12 *Simulated output spectrum for a BP ΣΔ modulator with a sine-wave input and an AWGN modeled quantization error.*

3.5. Quadrature Bandpass ΣΔ Modulator

The basic principle of quadrature ΣΔ conversion was presented in [8] and [32]. Analysis of [32] was extended in [34] and circuit implementation was discussed therein. Considerations and results presented in [34] were complemented with the mismatch analysis of [33] and more thorough background theory in [30]. Schreier et al., working with Analog Devices Inc., have also issued a patent on the topic [66]. A conventional quadrature ΣΔ converter consists of an input branch, a loop filter(s) and a feedback branch. The main difference between the real and quadrature, or complex, modulator is that the quadrature modulator operates on complex input samples and similarly the output is given in complex form.

This complex processing enables asymmetric noise shaping around DC for the quadrature modulators. This of course implies also that the poles and the zeros of the modulator can be asymmetric about the real axis – and thus don't need to be complex conjugates. [68] These characteristics are demonstrated with zero-pole plot and amplitude response in Figure 3.13. Zero-pole plot on the right shows that the modulator zero is situated on positive frequency around 0.375 relative to the sampling frequency and lies on unit circle. The pole is in origin.

The zero seen in the below zero-pole plot makes the NTF amplitude response notch on that frequency. This single zero results in a single frequency-asymmetric notch in contrast to the symmetric twin-notches in the case of real bandpass modulation. If the desired complex signal is situated solely at the frequency of the notch, it is in a sense

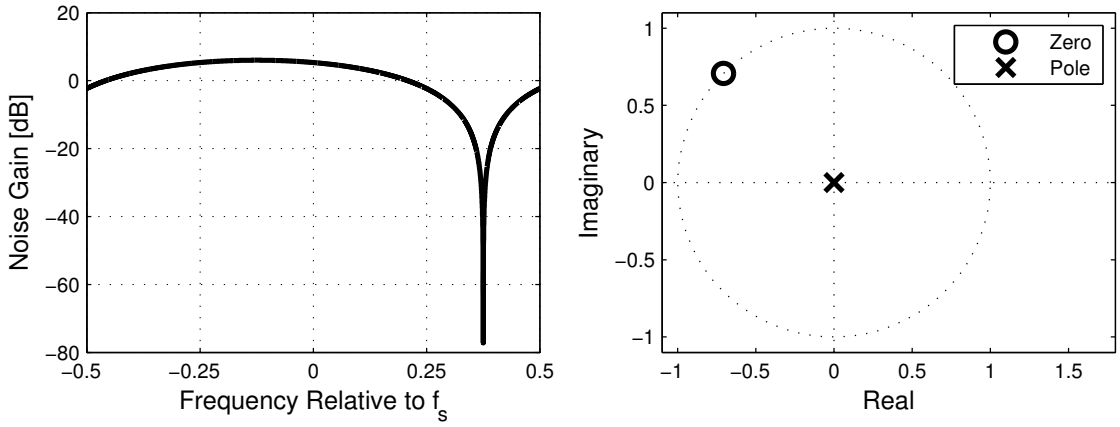

Figure 3.13 *Amplitude response (left) and zero-pole plot (right) of the NTF, where the noise notch is at a frequency 0.35 relative to* f_S.

more efficient to have notch only on that frequency. Twin quadrature modulators were found to have performance advantage over real bandpass modulator also in case of real inputs due to, e.g., not suffering from inband noise shaping degradation because of conjugate band zeros [38].

Realizing this kind of behavior can be done with a complex transfer function. Therefore, quadrature ΣΔ modulators are designed with complex loop filters as is presented in Figure 3.14. A complex modulator has two inputs, which describe the real and the imaginary part of complex signal. Correspondingly, output is composed of two real signals, which together form a complex one. [23]

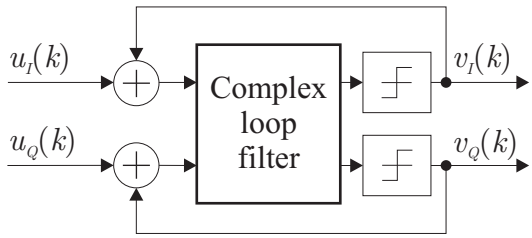

Figure 3.14 *Quadrature ΣΔ modulator structure with a complex loop filter [23].*

In principle, the noise shaping of a quadrature ΣΔ modulator can be thought as a lowpass ΣΔ response with complex frequency shift to some nonzero center frequency. First-order quadrature modulator has just as steep and wide noise transfer function notch as a corresponding lowpass modulator has on DC. This also means that the SNR equations (3.7)–(3.9) derived for the lowpass modulator can be applied also in case of quadrature modulator.

Modeling of the quadrature ΣΔ modulator will be discussed in more detail in Chapter 4. Simulation results verifying the concept presented above will also be given therein.

3.6. Discrete-Time vs. Continuous-Time

In [21] a comparison between switched-capacitor (SC) and continuous-time (CT) ΣΔ modulators is presented. The main difference between the two architectures is in loop filter, which can be, for example, an integrator. SC modulators use switched-capacitor filters with several nonidealities for integration. SC integrator limits for example the maximum bandwidth of the converted signal because of the settling time of the circuit.

In continuous-time architecture, the integration is done with high-order op-amp filter, which has purely resistive input. One of the major effects is that there is no acquisition phase and thus no need for sample-and-hold stage in the amplifier. The CT converters have been considered difficult to design and one drawback is that the characteristics of the integrator are not directly related to sample clock but depend on conventional rules of active filter design. So if the sampling frequency is changed to match new signal bandwidth the filter must be tuned again. [21] One clear advantage in CT modulator is that also the sampling jitter noise is shaped inside the modulator loop but, on the other hand, feedback DAC jitter may cause some problems [74].

CT ΣΔ modulators have not been widely available in commercial use. A long step forward was taken when National Semiconductor published [51] industry's first CT ΣΔ converter. It was claimed, that the converter offers 25 MHz alias-free sample bandwidth with 30 % less power consumption than competing devices with pipeline (discrete-time) architecture.

Generally, CT implementations have been considered faster than SC and thus fit for wideband applications. CT converter sampling rates have been increasing steadily and seem to be approaching a gigasample per second range [49], [71]. At the same time, highest SC modulator speeds have usually been in order of tens of megasamples [60], [62].

3.7. Single-bit vs. Multi-bit

Either a 1-bit or a multi-bit quantizer can be employed in the ΣΔ architecture. [1], [7], [24] The number of the bits is effectively changed in the forward line ADC and the feedback DAC. The 1-bit converter has an inherent linearity but a limited resolution, which demands high oversampling ratios in order to gain resolution of numerous effective bits. The multi-bit quantization can be seen as an attractive solution especially for wideband information signals when the achievable sampling rates limit the possible oversampling ratios [60].

On the other hand, multi-bit converter has better resolution, but the feedback DAC linearity limits the linearity of the whole converter. Element mismatches in the DAC cause a nonideal transfer function and nonlinear behavior. [39], [68] A few methods have been presented in the literature to compensate element mismatches in DAC, e.g., [22], [64] and [81].

3.8. Considerations on Modulator Order

The effects of the feedback order variations on a lowpass modulator have been documented quite extensively and analysis fit for purpose can be found from, e.g., [2] and [7]. The following analysis is based on [7]. In the basic ΣΔ principle, the negative feedback signal is fed straight back to single integrator on forward branch. At the same time, noise shaping characteristics of the modulator can be enhanced by increasing the order of the feedback. The second-order structure introduces another integrator with feedback of its own as shown in Figure 3.15.

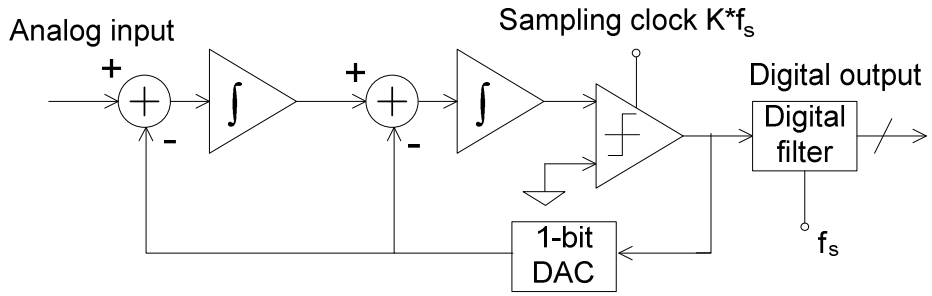

Figure 3.15 *Second-order ΣΔ converter [2].*

Following again the analysis of [7] for second-order feedback the inband SNR becomes

$$SNR = 10\log_{10}(\sigma_x^2) - 10\log_{10}(\sigma_e^2) - 10\log_{10}\left(\frac{\pi^4}{5}\right) + 50\log_{10}\left(\frac{f_S}{2f_B}\right) \tag{3.10}$$

and again substituting $f_S\,/\,2f_B = 2^r$ it can be found, that

$$SNR = 10\log_{10}(\sigma_x^2) - 10\log_{10}(\sigma_e^2) - 10\log_{10}\left(\frac{\pi^4}{5}\right) + 15.05r. \tag{3.11}$$

Based on (3.11) it is clear, that now every doubling of OSR increases SNR with approximately 15dB. So there is obvious improvement when compared to the findings for the first-order modulator in (3.7) and (3.8).

A higher-order feedback generates an even more aggressive NTF and steeper ascent of the SNR as a function of the OSR as is shown in Figure 3.16 for the first three orders.

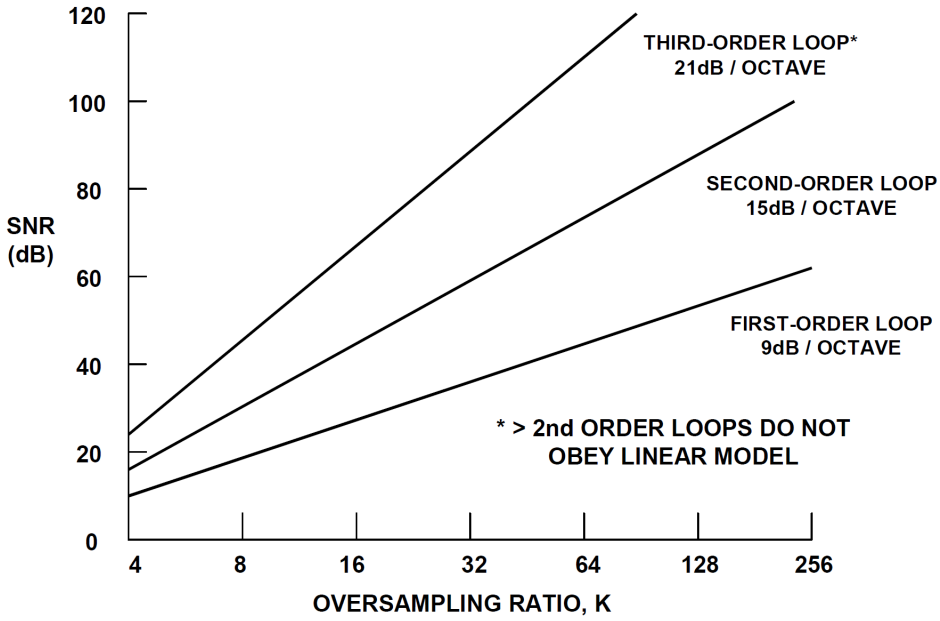

Figure 3.16 *SNR as a function of OSR for the first three orders of a ΣΔ modulator [2].*

The generalized version of SNR for *L*th-order modulator in [4] is given by

$$\begin{aligned} SNR = {} & 10\log_{10}(\sigma_x^2) - 10\log_{10}(\sigma_e^2) - 10\log_{10}\left(\frac{\pi^{2L}}{2L+1}\right) \\ & +(20L+10)\log_{10}\left(\frac{f_S}{2f_B}\right), \end{aligned} \tag{3.12}$$

which can again be simplified by defining quantization noise power as a function of used bits b and crest factor CF_{dB}

$$SNR = 6.02b + 4.76 - CF_{dB} - 10\log_{10}\left(\frac{\pi^{2L}}{2L+1}\right) + (20L+10)\log_{10}\left(\frac{f_S}{2f_B}\right). \tag{3.13}$$

In [2] some stability issues with higher than second-order architecture are reported, but [7] and particularly [26] give more thorough analysis on stability problems caused by raised feedback order. In brief, input values greater than certain limit can cause the quantizer to overload and thus risk the stability. On the other hand, the limit cycle oscillations may also cause the quantizer to overload [7].

3.9. Single-Stage vs. Multi-Stage

A higher-order noise transfer function and thus better noise shaping characteristics can be obtained also by employing cascaded modulators on a single input. The main principle is that the following stage extracts and digitizes the remaining error of the preceding stage(s). After the conversion, this error signal is subtracted from the previous output. If the latter stages operate also on ΣΔ principle, which isn't obligatory, also the noise of these stages is shaped. [68]

On the other hand, also a traditional Nyquist ADC, e.g., a flash converter, can be used as a following stage to simplify the system. This kind of structure, where the second stage converter has zero-order noise shaping, is usually noted as L-0 cascade, where L denotes the order of the first stage ΣΔ modulator. The L-0 cascade system is also called Leslie-Singh. In case of subsequent nonzero-order noise shaping stages, the structure is named MASH, which stands for Multi-stAge noise SHaping. [68] The principle can be extended to contain more than two stages, e.g., three stage MASH is proposed in [68].

These kinds of structures have been proposed particularly for wideband systems with limited oversampling possibilities. In addition, reconfigurable multi-stage converters for software defined radio receivers have been studied recently. Reconfigurability means that some parts or stages can be digitally tuned or turned on and off depending on the demands of the communication standard being received at each moment. [11], [59], [63]

The examples in following Sub-sections consider lowpass ΣΔ modulators for the sake of simplicity. However, multi-stage concept can be utilized also in case of real [17] or complex [13] bandpass modulators.

3.9.1. Leslie-Singh

An example of a Leslie-Singh structure consisting of a first-order ΣΔ modulator as a first stage is shown in Figure 3.17. Thus, this setup represents 1-0 cascade. The quantization noise of the first stage $e_1(k)$ is extracted by subtracting nonquantized signal $y_1(k)$ from the output of the first stage $v_1(k)$. Now this error signal is converted in order to obtain the digital version of the error as an output of the second stage $v_2(k)$.

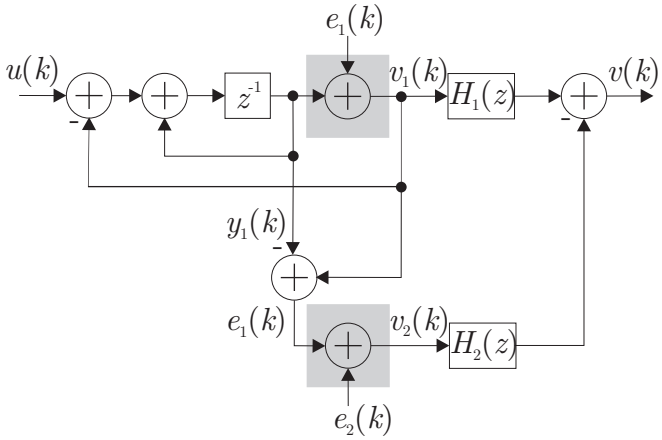

Figure 3.17 *Discrete-time linearized model for the 1-0 cascade (Leslie-Singh) multi-stage ΣΔ structure [68].*

To match the outputs of the stages, the output of the first stage must be delayed equally to the latency of the second stage. This is done with choosing $H_1[z] = z^{-k}$. On the other hand, also the digitized error signal must be made to match the shaped version of the first stage quantization noise in order to successfully remove it from the output signal. This is done digitally with selection of $H_2[z] = NTF_1[z]$. Now subtracting the filtered output of the second stage from the delayed output of the first stage gives the final output

$$\begin{aligned} V(z) &= H_1[z]V_1[z] - H_2[z]V_2[z] \\ &= z^{-k}[STF_1[z]U[z] + NTF_1[z]E_1[z]] \\ &\quad -z^{-k}NTF_1[z][E_1[z] + E_2[z]] \\ &= z^{-k}[STF_1[z]U[z] - NTF_1[z]E_2[z]]. \end{aligned} \tag{3.14}$$

Now, it can be seen that error in the output signal is the quantization noise of the second stage shaped by the NTF of the first stage. This can be assumed smaller than the original error because second stage ADC can easily have more resolution (e.g., multi-bit pipeline converter). [68]

3.9.2. Multi-Stage Noise Shaping (MASH)

If the second stage quantization error $e_2(k)$ is also shaped with a ΣΔ modulator, the structure is known as MASH, which is graphically demonstrated in Figure 3.18. This leaves the desired signal band relatively clean of the second stage noise also. The price is increased system complexity with the loop filter and the feedback. On the other hand, due to the noise shaping now also the second quantizer resolution can be possibly lowered.

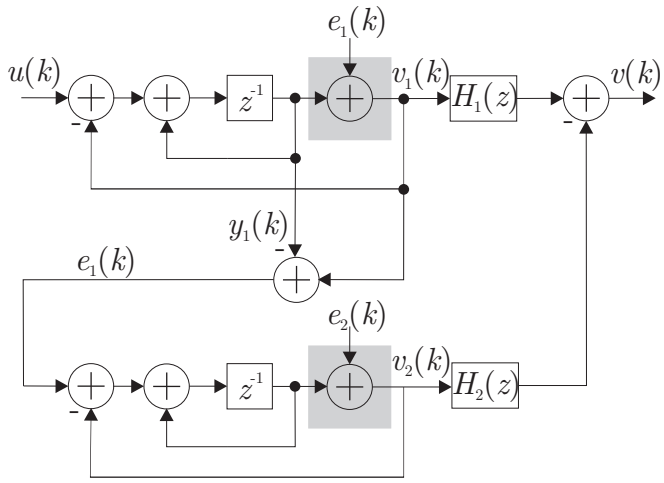

Figure 3.18 *Discrete-time linearized model for 1-1 MASH ΣΔ structure [68].*

The overall noise shaping done in the stages is of the order of summed orders of the stages. This can be shown, e.g., by assuming purely delaying signal transfer functions with $STF_1[z] = STF_2[z] = z^{-1}$ and lowpass noise shaping modulators with $NTF_1[z] = NTF_2[z] = 1 - z^{-1}$. With this setup, deriving the output of the whole system gives

$$\begin{aligned} V &= H_1[z]V_1[z] - H_2[z]V_2[z] \\ &= H_1[z](STF_1[z]U[z] + NTF_1[z]E_1[z]) \\ &\quad -H_2[z](STF_2[z]E_1[z] + NTF_2[z]E_2[z]) \\ &= STF_1[z]STF_2[z]U[z] - NTF_1[z]NTF_2[z]E_2[z] \\ &= z^{-1}U[z] - (1 - z^{-1})^2 E_2[z], \end{aligned} \tag{3.15}$$

if the condition

$$H_1[z]NTF_1[z] - H_2[z]STF_2[z] = 0 \tag{3.16}$$

holds. Thus, the noise shaping performance of the 1-1 MASH is similar to the second-order modulator, but the stability is of the first-order, because both the stages have only one feedback.

One practical solution for satisfying (3.16) is $H_1[z] = STF_2[z]$ and $H_2[z] = NTF_1[z]$, $STF_2[z]$ being often only a delay. This leads again to a matching of the digital $H_2[z]$ and the analog $NTF_1[z]$. Mismatches between the mentioned two transfer functions have been analyzed to cause noise leakage. Several methods have been developed to prevent this, e.g., adaptive filtering. [40], [41], [64], [81]

3.10. Modulator Stability

In case of first-order lowpass ΣΔ modulator, described in 3.3, employing real integrator as a loop filter the stability of the modulator depends on the input $u(k)$. For example, with 1-bit quantization and DC input $u = 1.3$ (or any input with continuous $|u| > 1$), the loop becomes unstable. Feedback DAC will give 1 with every step, but still a net of $1.3 - 1 = 0.3$ will enter the integrator. This will increase the integrator output without a bound and the loop becomes unstable. [68]

Schreier and Temes state in [68] also that the stable input range of the modulator is such the loop filter remains linear and the quantizer isn't heavily overloaded. This leads to a conclusion that the input range should be less or equal to the feedback DAC full-scale or, in case of a multi-stage noise shaping configuration, to the one of the first feedback DAC. A value in order of a few dB's below this full-scale is given as a rule of thumb, particularly for higher-order modulators.

Another factor affecting the loop stability is the amplitude response of the signal transfer function. For single-bit modulators, rule of thumb $\max_{\omega} \left| STF(e^{j\omega}) \right| < 2$ (where ω is the angular frequency) was given as stability criteria in [18] and tuned to $\max_{\omega} \left| STF(e^{j\omega}) \right| < 1.5$ in [68]. It should be also noted that the STF and the NTF designs should be such that the poles of the transfer functions lie inside the unit circle [7].

The FIR transfer functions of course fulfill this criterion due to inherent stability property [32]. Inside the unit circle, the pole positions can be used to shape the response.

Comprehensive stability theory of the ΣΔ modulators is quite complicated, especially in case of multi-bit quantization, and interested reader is advised to see, e.g., [5], [26], [58], [68]. In [68] Schreier and Temes also note that even very detailed model can't predict stability with absolute reliability and they suggest extensive simulations to ensure the properties, particularly in case of a high-order modulator.

4. MODELING OF QUADRATURE ΣΔ ADC

To understand more thoroughly the behavior of quadrature ΣΔ modulator, it is essential to know in detail, how the quantization noise and, on the other hand, the input signal are processed inside the modulator. The base for more detailed analysis is the derivation of the noise transfer function and the signal transfer function. With the help of these functions, the role of separate blocks can be analyzed from the viewpoint of the whole system. Transfer functions can also be used to simulate the input-output relationship of the modulator. The results of this analysis have been utilized also in [46] and [47].

This chapter will give an analytical model for the first and the second-order converters. In the last section, a model for ΣΔ modulator of an arbitrary-order will be discussed. The signal transfer function and the noise transfer function are derived for these three set-ups.

4.1. General Aspects

A quadrature ΣΔ modulator can be implemented with a complex input, loop filter, feedback and output as was discussed in 3.5. In this subchapter, the implementation of the loop filter is studied and further characteristics of the modulator are discussed.

A complex loop filter, employed in the quadrature modulator, can be realized as a complex integrator when considering the first-order modulator. Higher-order systems usually have multiple integrators included. Basic block diagram of a complex integrator is shown in Figure 4.1. The main principle is similar as in a real integrator used in lowpass ΣΔ modulators. Input samples are integrated over a unit delay, the difference to a real system being that the samples are complex valued, as is the loop gain.

The basics of complex signal processing were discussed in Chapter 3. Building on that base, the complex integrator is graphically presented using complex-valued signals and complex multiplier M on the left side in Figure 4.1. In addition, the same structure is

given with real signals and real multiplications to demonstrate the actual implementation of the integrator.

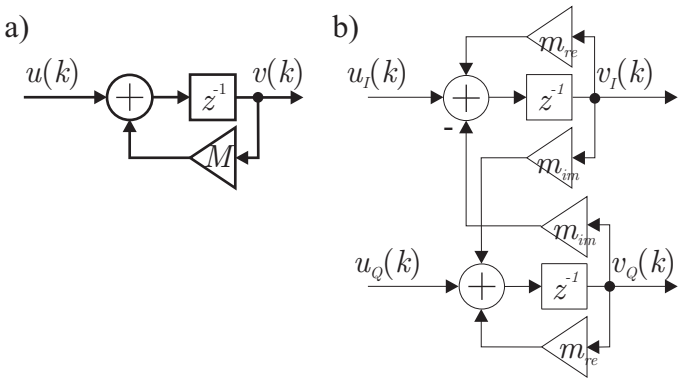

Figure 4.1 *Realization of complex integrator with a) complex signals and complex multiplication and b) real signals and real multiplications [23].*

The pole of such complex filter is determined by the feedback multiplier. The structure presented above leads to a transfer function $H[z]$ given by

$$H[z] = \frac{1}{z - M} = \frac{1}{z - (m_{re} + jm_{im})}, \tag{4.1}$$

where the terms M, m_{re} and m_{im} correspond to the illustration in Figure 4.1 denoting the complex multiplier and it's real and imaginary parts, respectively. The delaying nature of the integrator can be highlighted by expanding (4.1) to take the following form

$$H[z] = \frac{z^{-1}}{1 - Mz^{-1}} = \frac{z^{-1}}{1 - (m_{re} + jm_{im})z^{-1}}, \tag{4.2}$$

where the term z^{-1} in the numerator clearly presents unit delay of the system. The pole of the complex integrator defines the zero of the noise transfer function of the whole modulator as will be seen later in Sub-section 4.2.2.

4.2. First-Order Quadrature Modulator

The principle of quadrature ΣΔ conversion is demonstrated with analysis of first-order system. In addition, analytical equations will be derived for the NTF and the STF. By definition, the first-order system has one noise shaping stage, which enables placing one NTF zero at the frequency band in use. In addition, the STF may have a notch on chosen frequency as will be shown.

The output spectra of a first-order quadrature modulator with an exponential excitation are given in Figure 4.2. The left side plot is with 1-bit quantization. The right one has quantization replaced with AWGN corresponding to 1-bit theoretical full-band SNR of 7.76 dB. The signal transfer function is frequency flat with unity gain in both cases. The interference peaks visible at the left side plot around the relative frequency –0.125 match to the aliased third-order nonlinear distortion from the second Nyquist zone with the relative center frequency of $F_{3rd} = -3 \times 0.375 f_S + f_S = -0.125 f_S$.

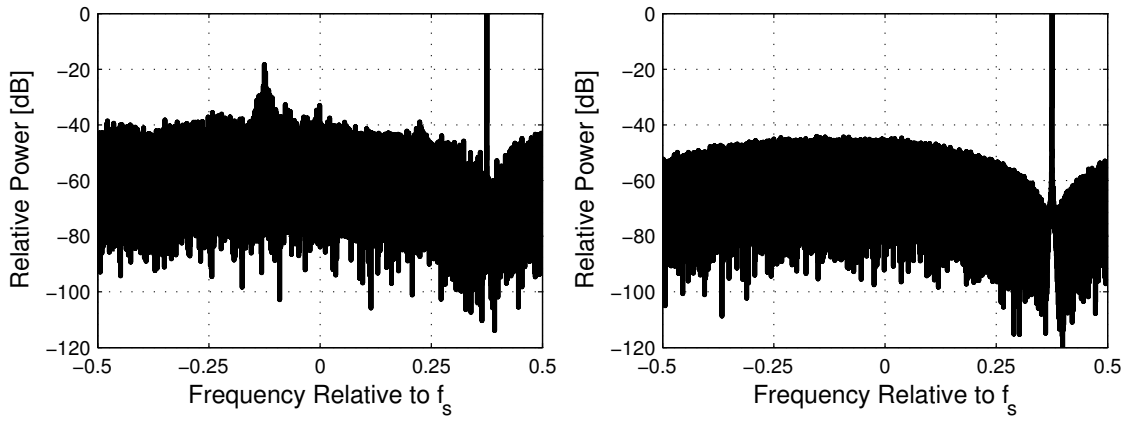

Figure 4.2 *Modulator output spectra with exponential input and the NTF notch at 0.375 relative to* f_S*, simulated with 1-bit quantization (left) and AWGN (right).*

The basic structure of the first-order ΣΔ modulator is presented in Figure 4.3, where $u(k)$, $e(k)$ and $v(k)$ are the complex input, the linearized complex quantization error and the complex output signals, respectively. The multipliers A, B and G are complex valued and affect the input signal fed straight to quantizer, the input signal fed to the loop filter $H[z]$ and the feedback signal from the output of the modulator, respectively.

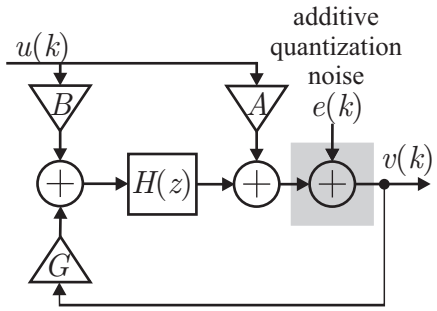

Figure 4.3 *First-order quadrature ΣΔ modulator with the loop filter* $H[z]$.

Based on this kind of structure, the *Z*-domain transfer function of the modulator can be derived. Thus, the output $V[z]$ of the modulator can be expressed with the input $U[z]$ and the quantization error $E[z]$ as

$$\begin{aligned} V[z] &= (A + BH[z])U[z] + E[z] + (GH[z])V[z] \\ &= \frac{A + BH[z]}{1 - GH[z]}U[z] + \frac{1}{1 - GH[z]}E[z], \end{aligned} \tag{4.3}$$

where A, B, G and $H[z]$ are as mentioned before and defined in Figure 4.3.

The loop filter $H[z]$ is a complex filter, which can be realized in either discrete-time switched-capacitor or continuous-time technique. Here we concentrate on SC realization of the filter. The main differences between SC and CT structures were discussed in Section 3.6. Integrator's feedback branch has complex multiplier M, which defines the pole – and thus the transfer function – of the integrator. [23]

Based on the complex structure presented in Figure 4.4, time domain behavior of the modulator can be analyzed. The system results in the discrete output $v(k)$, which can be expressed with help of the input $u(k)$ and the quantization error $e(k)$. The output is described by equation

$$\begin{aligned} v(k) = {} & Au(k) + (B - MA)u(k-1) + e(k) - Me(k-1) \\ & +(G + M)v(k-1). \end{aligned} \tag{4.4}$$

Transforming Equation (4.4) to the *Z*-domain results in the transfer function of the modulator. Output is thus given by an equation

$$\begin{aligned} V[z] &= [A + (B - MA)z^{-1}]U[z] + [1 - Mz^{-1}]E[z] + (G + M)z^{-1}V[z] \\ &= \frac{A + (B - MA)z^{-1}}{1 - (G + M)z^{-1}}U[z] + \frac{1 - Mz^{-1}}{1 - (G + M)z^{-1}}E[z], \end{aligned} \tag{4.5}$$

This result pronounces the significance of the specified coefficients. On the other hand, it corresponds to Equation (4.3), where the *Z*-domain output was derived with the loop filter marked with $H[z]$, being now $H[z] = 1/(z - M)$ as given in (4.1).

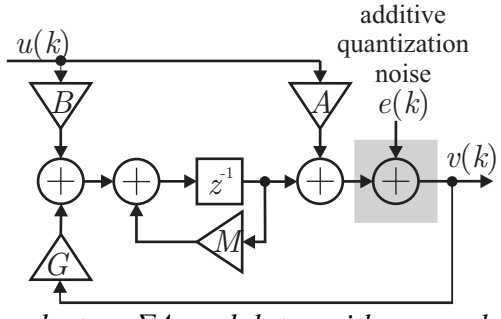

Figure 4.4 *First-order quadrature ΣΔ modulator with a complex integrator.*

More detailed analysis of the overall transfer function will be given in the following Sections, where the STF and the NTF are treated separately. However, already from (4.5) it can be noted that both transfer functions have common denominator, which affects the pole of the modulator giving the same pole for the STF and the NTF.

Placement of the NTF zero on the unit circle, in other words the angle of the zero, affects the frequency in which the notch is set. If the zero is pulled inwards from the unit circle, the notch flattens gradually.

At the same time the pole placement doesn't affect the frequency of the actual noise notch, but the shape of the frequency responses. This effect is demonstrated for the STF in Figure 4.5 with an amplitude response and a zero-pole plot. For the NTF similar plots are presented in Figure 4.6. When the pole is at the frequency of the zero and just inside the unit circle, amplitude response is flat except the notch, which is steep and relatively narrow. Pulling the pole towards the origin makes the notch wider. Anyway, if the STF and the NTF notches are placed on separate frequencies, there is always a tradeoff between the characteristics of the functions.

On the other hand, a flat STF passband would be desirable but at the same time placing the pole to the STF notch frequency gives rise to the noise gain at the NTF notch frequency. Ideally, this out-of-band noise gain would not drastically affect the system performance, but, e.g., under branch mismatch and resulting imbalance between in-phase and quadrature components this should be taken into account as will be seen later.

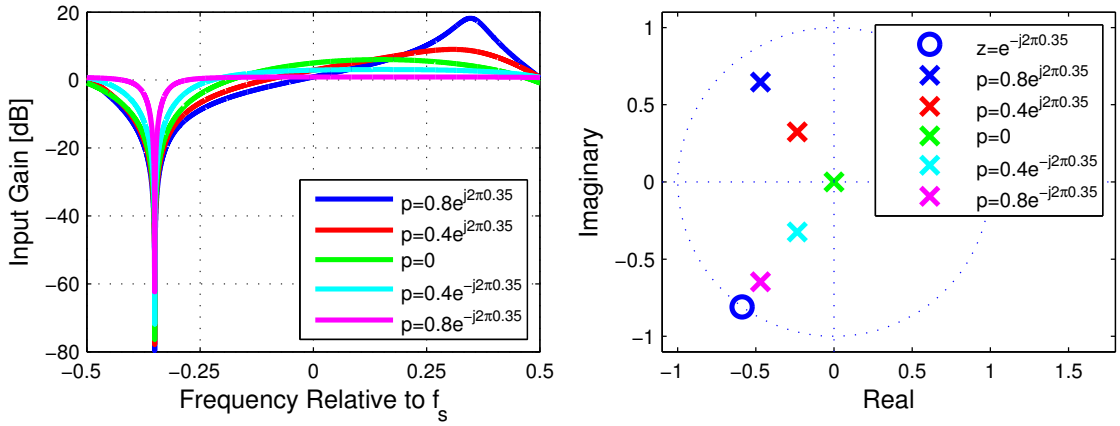

Figure 4.5 *On the left an amplitude response of the STF, where the zero is located at a frequency −0.35 relative to f_S, and on the right a corresponding zero-pole plot. The zero and the pole position(s) are marked with z and p, respectively.*

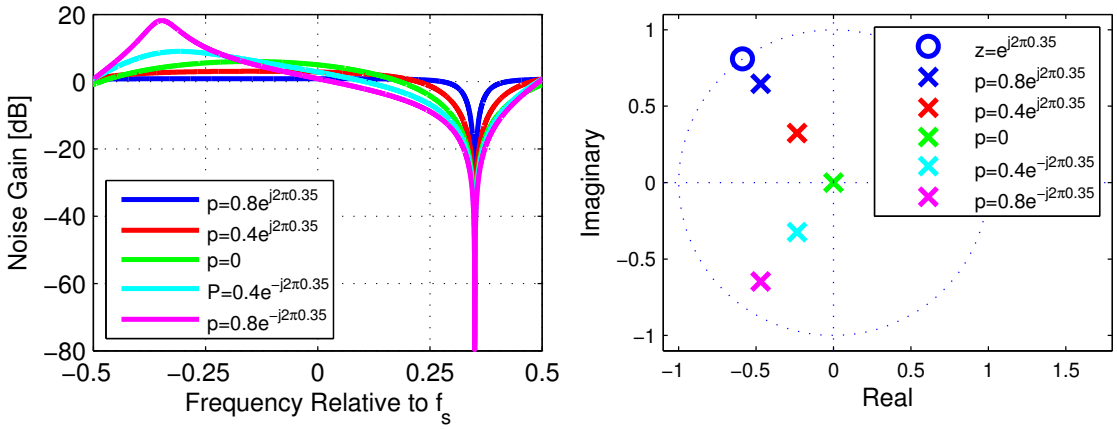

Figure 4.6 *On the left an amplitude response of the NTF, where the zero is located at a frequency 0.35 relative to* f_S*, and on the right a corresponding zero-pole plot. The zero and the pole position(s) are marked with* z *and* p*, respectively.*

Implementationwise, the complex structure of Figure 4.4, which was described by Equation (4.5), can be realized with two real inputs and outputs. Complex multipliers do also have two separate parts – real and imaginary. Thus, the real structure of a first order quadrature ΣΔ modulator is as presented in Figure 4.7 in time-domain.

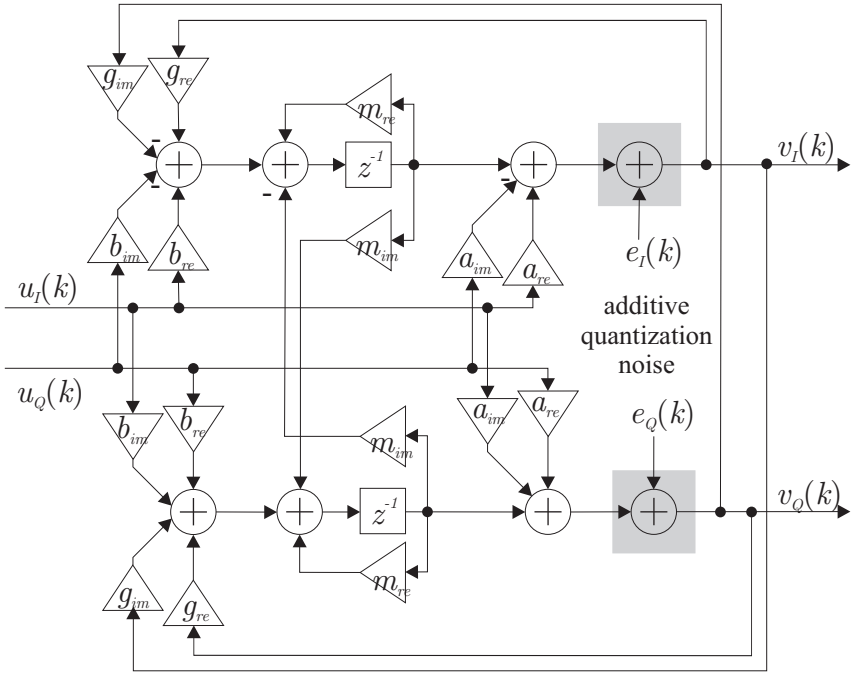

Figure 4.7 *First-order quadrature ΣΔ modulator with real coefficients and parallel real signals.*

The above figure depicts the coefficients of the structure in case of ideal matching between the I and Q branches. The effects of the inevitable mismatches in actual circuit implementation will be discussed in Chapter 5.

4.2.1. First-Order Signal Transfer Function

Signal transfer function shapes the input of the modulator, as already mentioned when discussing the basic principles of the ΣΔ modulation (Section 3.2). Thus, the output of the modulator – excluding quantization error at this point – is a filtered version of the input. The STF of the first-order modulator presented above in Figure 4.4 is given by the multiplier of the input $U[z]$ in Equation (4.5). Thus, resulting in a form

$$STF[z] = \frac{A + (B - MA)z^{-1}}{1 - (G + M)z^{-1}}. \tag{4.6}$$

From the above equation it can be seen, that in case of the first-order modulator one STF zero can be placed on the converted frequency band. The zero of the numerator, given by

$$z_{STF} = -\frac{B - MA}{A}, \tag{4.7}$$

defines the notch in amplitude response of the STF at a certain frequency. On the other hand, if the zero is placed in the origin, the resulting STF has a unity response and is thus frequency flat. The coefficients A and B can be used to tune the STF response independent of the NTF (as can be seen from (4.5)). Thus, these complex values define the actual STF zero $z_{STF} = e^{j2\pi\bar{f}_{int}}$, where $\bar{f}_{int}$ is the notch frequency relative to the f_S.

On the other hand, the denominator of the STF, defining the pole, affects the shape of the STF, as was shown in Section 4.2. The common pole of the NTF and the STF (p_{common}) can be solved from (4.6) straightforwardly and is thus defined by

$$p_{common} = G + M. \tag{4.8}$$

The parameter M, which is the pole of the complex integrator, is dominated by the desired noise shaping characteristics and the notch frequency, but the coefficient G can be chosen based on the desired signal transfer function characteristics.

The STF design example in Figure 4.8 highlights the filtering possibilities related to the zero placement. The tone on positive frequency is assumed to be the desired signal and the tone on the negative side of the spectrum is a noninteresting signal with interference potential. In case of I/Q imbalance some mirror-frequency interference would appear close to the frequency of the desired tone, originating from the opposite one.

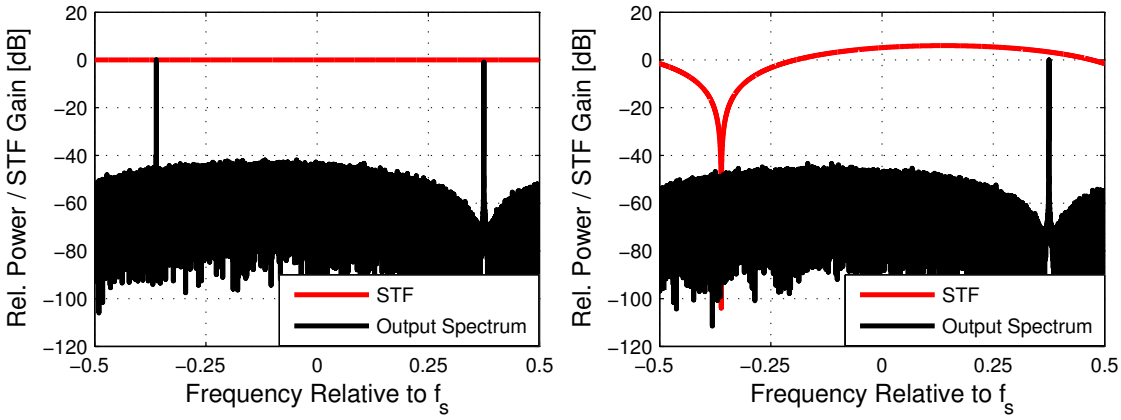

Figure 4.8 *Output spectra of the first order quadrature ΣΔ modulator with the unity STF (left) and with the STF zero on the negative side of the spectrum (right), the quantization noise modeled with AWGN of theoretical 1-bit variance.*

On the left side plot, the output spectrum is shown in case of the unity STF. Both the tones appear with similar amplitudes at the output. Right hand plot shows the case when STF zero is placed at the frequency of the tone on the negative side of the spectrum. The output spectrum clearly shows that this noninteresting signal and possible interference source is filtered efficiently enough to push the tone to the level of the noise floor.

4.2.2. First-Order Noise Transfer Function

The noise transfer function describes how the quantization error is shaped inside the modulator. Thereby it can be separated from the overall transfer function (4.5) as the multiplier of quantization error $E[z]$, resulting in an equation

$$NTF[z] = \frac{1 - Mz^{-1}}{1 - (G + M)z^{-1}}. \tag{4.9}$$

This shows that the NTF design is independent of the input coefficients A and B in the modulator structure described earlier. In the first-order modulator, the feedback branch and loop filter define the noise shaping characteristics. The NTF zero location is dominated by the integrator pole. The numerator zero of (4.9) confirms this giving

$$z_{NTF} = M. \tag{4.10}$$

This observation also confirms that the STF zeros can be set regardless of the NTF design with decent selection of the parameters A and B. This also gives freedom to the NTF zero design because the loop filter pole M can be selected solely on the noise shaping basis, to give $z_{NTF} = e^{j2\pi\overline{f}_{pass}}$, where $\overline{f}_{pass}$ is the NTF notch frequency rela-

tive to the f_S. On the other hand, the STF and the NTF share the same pole as was given in (4.8), which is defined by G and M. This common pole between the STF and the NTF gives rise to some optimization tradeoffs as was discussed in Section 4.2.

Simulation example of the first-order NTF is given in Figure 4.9. An exponential tone is used as an exciting input signal. The quantization error of the 1-bit ADC is modeled again as AWGN for simplicity and to highlight the phenomenon at hand. The left side plot shows the output spectrum without the noise shaping, so the NTF can be said to have a unity response. At the same time on the right side, a spectrum in case of the first-order complex NTF is given.

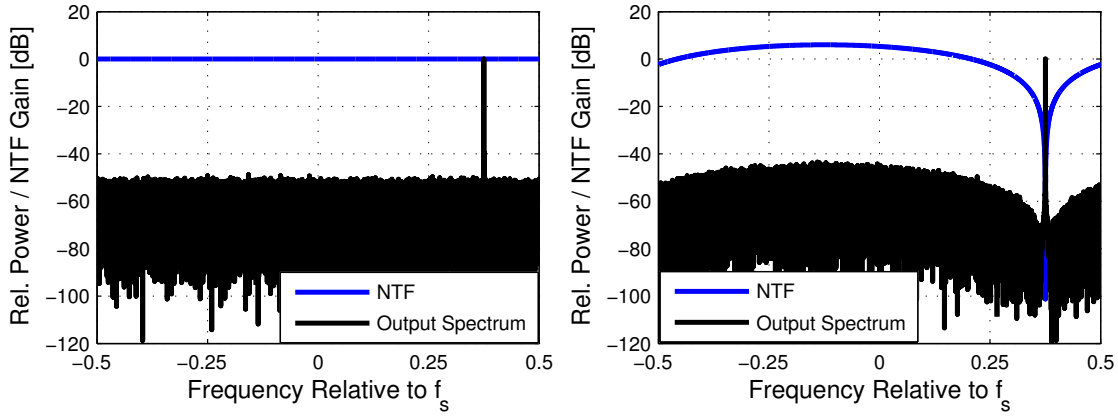

Figure 4.9 *Output spectra of the 1-bit ADC without noise shaping (left) and with the first-order quadrature NTF (right), the quantization noise modeled as AWGN of the theoretical 1-bit variance.*

The difference made by the noise shaping can be clearly seen from the above plots. The noise floor has dropped roughly 20 dB on the notch frequency. In modern digital communications, this makes a notable difference. On the other hand the noise between relative frequencies −0.25 and 0 has slightly risen, due to the amplifying NTF response on that frequency interval. Of course, in more sophisticated higher-order systems noise shaping can be designed to have more pronounced effect.

4.3. Second-Order Quadrature Modulator

In this chapter, the analysis is extended to deal with a second-order quadrature ΣΔ modulator. With this setup, the NTF and the STF can be built in more sophisticated way than in the first-order modulator. Raising the order by one enables placement of two zeros in the design of the NTF and the STF.

A block diagram of the second-order ΣΔ modulator is presented in Figure 4.10. From the figure, it is clear that the extension is realized by adding another integrator $H_2[z]$ to the structure. The input and the feedback signals are fed to this integrator via complex coefficients C and F, respectively.

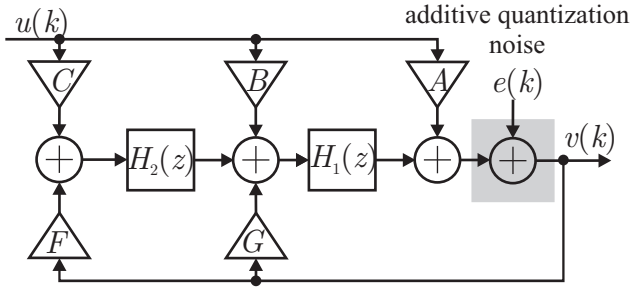

Figure 4.10 *Second-order quadrature ΣΔ modulator with the loop filters* $H_1[z]$ *and* $H_2[z]$.

Based on the structure in Figure 4.10, *Z*-domain transfer function can be derived for the second-order modulator. The analysis results in the equation

$$V[z] = \frac{A + BH_1[z] + CH_1[z]H_2[z]}{1 - (GH_1[z] + FH_1[z]H_2[z])}U[z] + \frac{1}{1 - (GH_1[z] + FH_1[z]H_2[z])}E[z]. \quad (4.11)$$

From (4.11), it can be seen that the feedback coefficients and the responses of the complex integrators are defining the poles of the transfer function and also the zeros of the NTF as in the first-order case. The input coefficients A, B and C are seen in the numerator of the STF and thus define the zeros of the signal response. When the complex integrators $H_1[z]$ and $H_2[z]$ of Figure 4.10 are implemented with a delay and a complex feedback multiplier, the block diagram takes the form presented in Figure 4.11.

In the below figure, the complex multipliers M and N represent the poles of the complex integrators. Based on the block diagram, time domain behavior of the modulator can be solved. Modulator output $v(k)$ can be given as a function of the present and

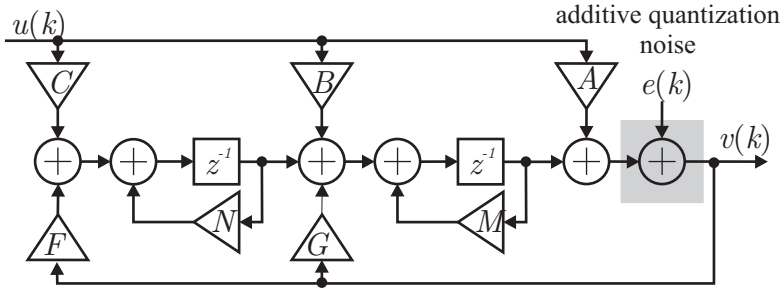

Figure 4.11 *Second-order quadrature ΣΔ modulator with two complex integrators.*

the previous versions of the input, the output and the quantization error with the equation

$$\begin{aligned} v(k) = {} & Au(k) + (B - NA - MA)u(k-1) + (C - NB + MNA)u(k-2) \\ & + e(k) - (M+N)e(k-1) + (MN)e(k-2) + (M+N+G)v(k-1) \\ & + (-MN - NG + F)v(k-2). \end{aligned} \tag{4.12}$$

After applying the *Z*-transform for (4.12) and some reformation, the output of the second-order ΣΔ modulator can be presented as

$$\begin{aligned} V[z] = {} & \frac{A + (B - NA - MA)z^{-1} + (C - NB + MNA)z^{-2}}{1 - (M+N+G)z^{-1} + (MN + NG - F)z^{-2}} U[z] \\ & + \frac{1 - (M+N)z^{-1} + (MN)z^{-2}}{1 - (M+N+G)z^{-1} + (MN + NG - F)z^{-2}} E[z]. \end{aligned} \tag{4.13}$$

Equation (4.13) shows, that poles of the transfer functions are determined by both integrator poles and by both feedback complex multipliers.

4.3.1. Second-Order Signal Transfer Function

In case of a second-order quadrature ΣΔ modulator, the signal transfer function has two zeros and two poles. From Equation (4.13), it can be seen that the input $U[z]$ is shaped with the STF given by

$$STF[z] = \frac{A + (B - NA - MA)z^{-1} + (C - NB + MNA)z^{-2}}{1 - (M+N+G)z^{-1} + (MN + NG - F)z^{-2}}. \tag{4.14}$$

The STF zeros can be solved based on the numerator of (4.14) and are thus given in a form

$$\begin{aligned} z_{STF}^{(1)} &= \frac{2C - 2BN + 2MN}{M - B + N + \sqrt{B^2 + M^2 + N^2 - 2BM + 2BN - 2MN - 4C}} \\ z_{STF}^{(2)} &= -\frac{2C - 2BN + 2MN}{B - M - N + \sqrt{B^2 + M^2 + N^2 - 2BM + 2BN - 2MN - 4C}}. \end{aligned} \tag{4.15}$$

From (4.15), it is clear that the complexity of the STF zero placement is clearly higher than in the first-order case discussed in Sub-section 4.2.1. Poles of the transfer functions – common to the STF and the NTF – are correspondingly given in form

$$p_{common}^{(1)} = \frac{G + M + N + \sqrt{G^2 + 2GM + 6GN + M^2 - 2MN + N^2 + 4F}}{2}$$
$$p_{common}^{(2)} = \frac{G + M + N - \sqrt{G^2 + 2GM + 6GN + M^2 - 2MN + N^2 + 4F}}{2}. \quad (4.16)$$

The above equation shows that also the complexity of the pole placement is notably increased when compared to the first-order case in 4.2.1.

The STF design in Figure 4.12 shows how the second-order STF gives more freedom when compared to the first-order case presented in 4.2.1. Left hand plot shows again the output spectrum in case of the unity STF. From there, it can be seen that there are two exponential tones on the negative frequencies. In the right plot, the STF is attenuating most of the negative frequencies. In addition, the assumed desired signal has a magnitude gain of 20 dB due to pole placement on surrounding frequencies. The tones on the negative frequencies have been clearly attenuated. The other one lying directly on the STF notch frequency has been pushed down to the noise floor and the other one has almost 40 dB of relative attenuation when compared to the desired positive-frequency tone. More detailed discussion on STF design possibilities can be found from [37].

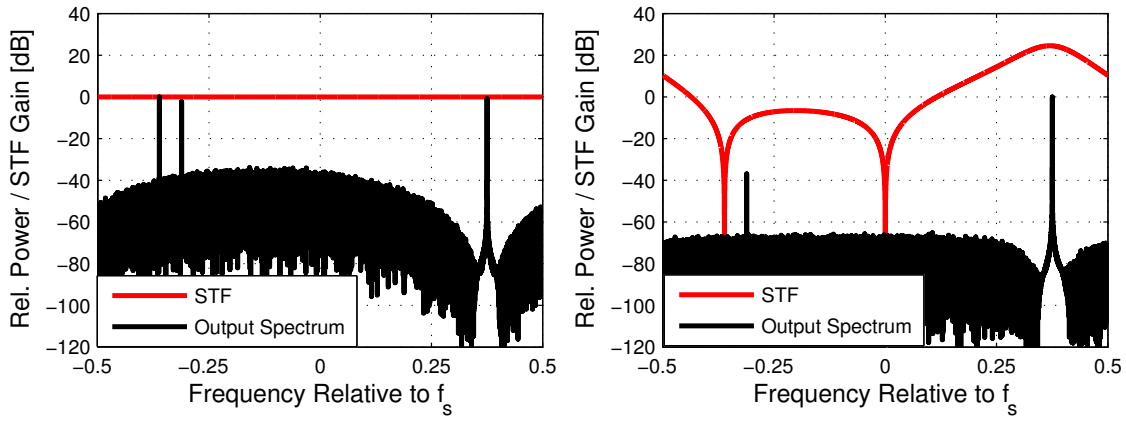

Figure 4.12 *Output spectra of the second-order quadrature ΣΔ modulator with a unity STF (left) and with the STF zeros on the negative side of the spectrum and on DC (right), quantization noise modeled as AWGN of the theoretical 1-bit variance.*

4.3.2. Second-Order Noise Transfer Function

The second-order modulator structure gives possibilities to more efficient noise shaping. Noise transfer function is in this case

$$NTF[z] = \frac{1 - (M + N)z^{-1} + (MN)z^{-2}}{1 - (M + N + G)z^{-1} + (MN + NG - F)z^{-2}}. \quad (4.17)$$

As a follow-up from (4.17) the NTF zeros can be solved and are given by

$$\begin{aligned} z_{NTF}^{(1)} &= M \\ z_{NTF}^{(2)} &= N. \end{aligned} \tag{4.18}$$

which is truly an expected result and confirms that the poles of the loop filters define the notch frequencies in the NTF. The exact shape of the NTF depends also on the common poles given in (4.16).

Schreier found in [65] that in case of a second-order modulator, optimal placement of the zeros gives 3.5 dB advantage when compared to coincident zeros. For third-order modulator the difference would be already 8 dB. Figure 4.13 demonstrates this principle with simulation example. Left side plot shows the output spectrum with two coincident zeros. On the right side the zeros have been spread symmetrically around the tone frequency. Close inspection of the noise floor shows that the spread zeros shape the noise more efficiently away from the notch. Close to the frequencies of the spread zeros the difference in the noise floor level is around 3 dB and no observable additional noise can be seen between the zeros when compared to coincident zeros. Thus, the simulated response presented below agrees nicely with the literature.

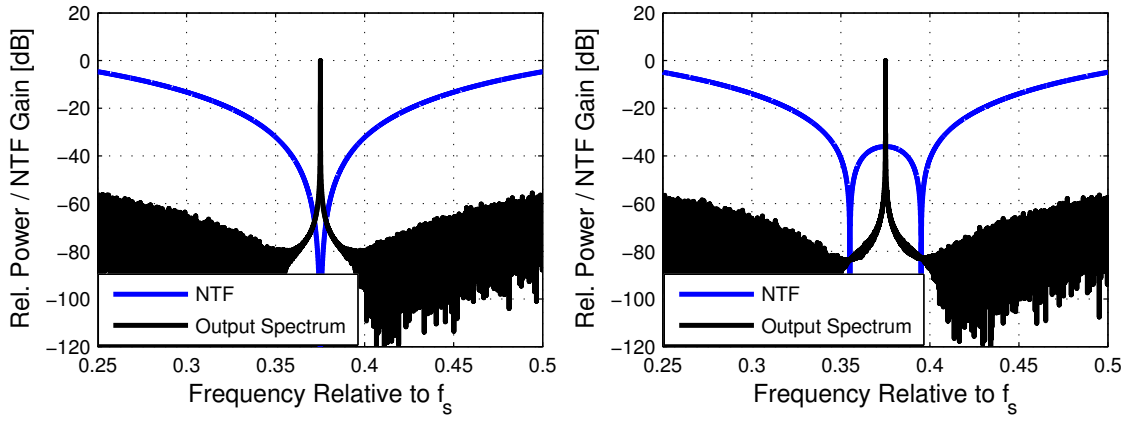

Figure 4.13 *Output spectra of the 1-bit ADC with second-order noise shaping in case of the coincident NTF zeros (left) and the symmetrically spread NTF zeros (right), quantization noise modeled as AWGN of the theoretical 1-bit variance.*

4.4. Higher-Order Quadrature Modulator

A general model for a quadrature ΣΔ modulator of an arbitrary-order can be derived by adding N loop filters from $H_1[z]$ to $H_N[z]$ and corresponding input (from A_0 to A_N)

and feedback (from G_1 to G_N) branches to the structure. This is illustrated in Figure 4.14. With *N*th-order modulator, *N* zeros and poles can be used to shape the STF and the NTF.

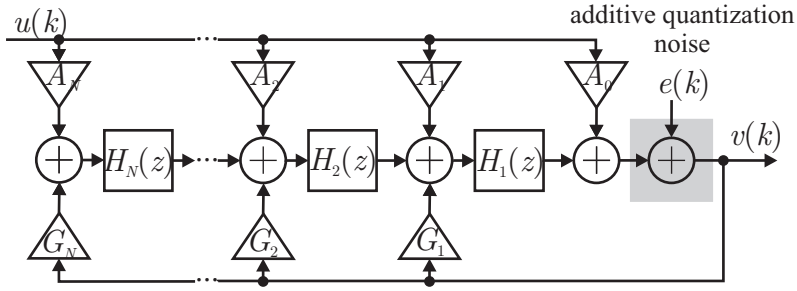

Figure 4.14 *Nth-order quadrature ΣΔ modulator.*

Next, the overall transfer function is derived for an the above *N*th order structure. The analysis of the modulator output $v(k)$ and *Z*-domain version $V[z]$ results in the following *Z*-domain equation:

$$\begin{aligned} V[z] &= \left(A_0 + \sum_{i=1}^{N} A_i \prod_{j=1}^{i} H_j[z] \right) U[z] + \left(\sum_{k=1}^{N} G_k \prod_{l=1}^{k} H_l[z] \right) V[z] + E[z] \\ &= \frac{A_0 + \sum_{i=1}^{N} A_i \prod_{j=1}^{i} H_j[z]}{1 - \sum_{k=1}^{N} G_k \prod_{l=1}^{k} H_l[z]} U[z] + \frac{1}{1 - \sum_{k=1}^{N} G_k \prod_{l=1}^{k} H_l[z]} E[z]. \end{aligned} \tag{4.19}$$

Based on the above formula, the STF and the NTF of the *N*th-order modulator are given by

$$STF[z] = \frac{A_0 + \sum_{i=1}^{N} A_i \prod_{j=1}^{i} H_j[z]}{1 - \sum_{k=1}^{N} G_k \prod_{l=1}^{k} H_l[z]} \tag{4.20}$$

and

$$NTF[z] = \frac{1}{1 - \sum_{k=1}^{N} G_k \prod_{l=1}^{k} H_l[z]}, \tag{4.21}$$

respectively.

As mentioned above, this kind of structure allows theoretically N separate zeros for the NTF and the STF. However, practical order of the modulator is limited, e.g., by the stability of the whole structure (see Section 3.8). Highest well-accepted order in true circuit implementation proposed in the literature has been four [30], [34]. Considerations on optimal zero placements were given earlier in Section 4.3 with examples on the second-order modulator.

5. I/Q IMBALANCE ON QUADRATURE ΣΔ ADC

The main effects of I/Q mismatch in radio receivers are quite extensively documented in scientific literature [45], [48], [55], [56], [75], [76], [84] and were discussed earlier in Sub-section 2.1.4 at preliminary level. In this chapter, the main objective is to obtain an analytical model for the imbalance effects in case of a quadrature ΣΔ modulator. The effects will be studied based on the model of the first-order system derived in 4.2. Both the input signal and quantization noise components are taken into account and considerations are given separately from the STF and the NTF point of view. Selected results of this analysis have been published in [46]. In addition, more thorough full-length journal article [47] is submitted and under review at this moment.

The modulator structure with possible mismatches between the I and Q branches is presented in Figure 5.1, where subscripts 1 and 2 separate the possibly mismatched realizations of the ideally symmetric coefficients in each branch. The structure shows that mismatches are possible in either of the inputs, in the feedback of the loop filter or in the feedback of the modulator. The feasible IRR range in practical quadrature receivers

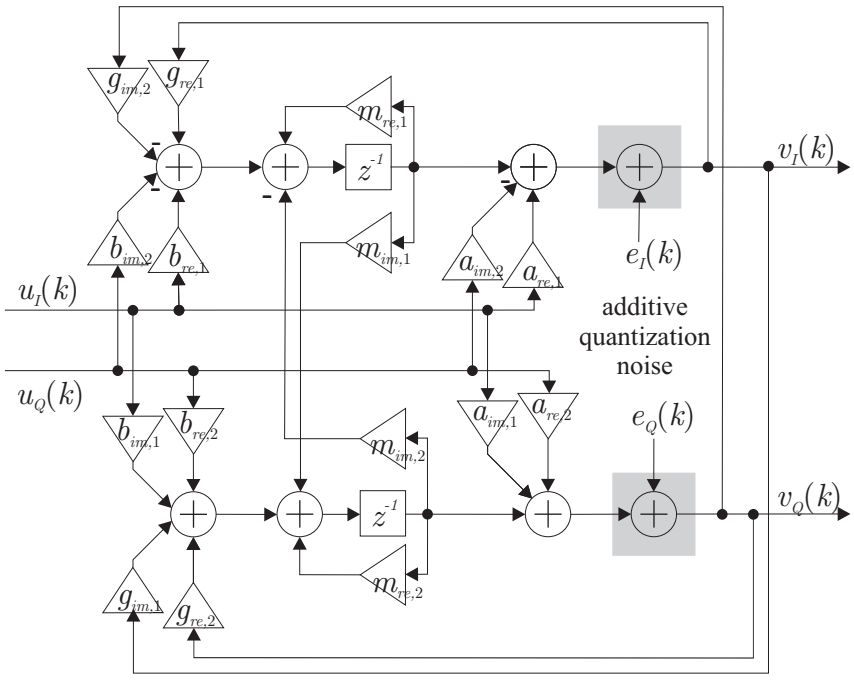

Figure 5.1 *First-order quadrature ΣΔ modulator with mismatched real coefficients.*

as a whole is typically reported to be around 20–40 dB [1], [20], [77], which consider ing a gain mismatch between the real coefficients of the branches means values in theorder of 0.1–10 %. Because the IRR of a single receiver component should be higher than that of the whole receiver with multiple mirror-frequency interference sources, mismatches from 10^{-1} to 10^{-5} will be considered to cover the realistic range.

In Section 4.2 it was concluded that a mismatch in complex multiplication causes mirror frequency interference due to a conjugate response for the input signal. This is the case also for the ΣΔ modulator. On the other hand, the quantization noise, generated inside the modulator loop has also an image response in case of the mismatch. This results, in addition to the STF and the NTF, in two additional transfer functions, which are called an image signal transfer function (ISTF) and an image noise transfer function (INTF). [30], [33], [72]

It should also be emphasized that only the differential error is causing the mirroring effect. This means that the deviation from nominal value is opposite in the two channels. If the error is common and parallel between the branches, the desired response is affected but no mirror frequency interference is present (for more detailed presentation, see Sub-section 2.1.4). [33]

Taking the possible mismatch into account the real outputs of the modulator $v_I(k)$ and $v_Q(k)$ can be derived, resulting in equations

$$\begin{aligned} v_I(k) = {} & a_{re,1}u_I(k) - a_{im,2}u_Q(k) \\ & +(b_{re,1} - m_{re,1}a_{re,1} + m_{im,2}a_{im,1})u_I(k-1) \\ & -(b_{im,1} - m_{re,1}a_{im,2} - m_{im,2}a_{re,2})u_Q(k-1) \\ & +e_I(k) - m_{re,1}e_I(k-1) + m_{im,2}e_Q(k-1) \\ & +(g_{re,1} + m_{re,1})v_I(k-1) - (g_{im,2} + m_{im,2})v_Q(k-1) \end{aligned} \tag{5.1}$$

and

$$\begin{aligned} v_Q(k) = {} & a_{im,1}u_I(k) + a_{re,2}u_Q(k) \\ & +(b_{im,2} - m_{re,2}a_{im,1} - m_{im,1}a_{re,1})u_I(k-1) \\ & +(b_{re,2} - m_{re,2}a_{re,2} + m_{im,1}a_{im,2})u_Q(k-1) \\ & +e_Q(k) - m_{re,2}e_Q(k-1) - m_{im,1}e_I(k-1) \\ & +(g_{im,1} + m_{im,1})v_I(k-1) + (g_{re,2} + m_{re,2})v_Q(k-1), \end{aligned} \tag{5.2}$$

which define the in-phase and the quadrature components of the complex output signal, respectively.

5.1. General Imbalance Model

Based on the model presented in Figure 5.1 and the I and Q outputs defined in (5.1) and (5.2), the transfer functions of a mismatched modulator will be derived. The output of the analysis will be the four transfer functions (STF, ISTF, NTF and ISTF), which define the characteristics of the modulator. Output of the modulator is formed by the transfer functions according to the equation

$$V[z] = STF[z]U[z] + ISTF[z]U^*[z^*] + NTF[z]E[z] + INTF[z]E^*[z^*], \tag{5.3}$$

where $U^*[z^*]$ denotes the *Z*-transform of the input signal conjugate $u^*(k)$ and $E^*[z^*]$ denotes the *Z*-transform of the quantization noise conjugate $e^*(k)$.

After the *Z*-transformation for (5.1) and (5.2), the output of the I-branch is given by

$$\begin{aligned} V_I[z] = & \frac{a_{re,1} + (b_{re,1} - m_{re,1}a_{re,1} + m_{im,2}a_{im,1})z^{-1}}{1 - (g_{re,1} + m_{re,1})z^{-1}} U_I[z] \\ & - \frac{a_{im,2} + (b_{im,1} - m_{re,1}a_{im,2} - m_{im,2}a_{re,2})z^{-1}}{1 - (g_{re,1} + m_{re,1})z^{-1}} U_Q[z] \\ & + \frac{1 - m_{re,1}z^{-1}}{1 - (g_{re,1} + m_{re,1})z^{-1}} E_I[z] + \frac{m_{im,2}z^{-1}}{1 - (g_{re,1} + m_{re,1})z^{-1}} E_Q[z] \\ & - \frac{(g_{im,2} + m_{im,2})z^{-1}}{1 - (g_{re,1} + m_{re,1})z^{-1}} V_Q[z]. \end{aligned} \tag{5.4}$$

To simplify the presentation, the numerators and the denumerators, defining the zeros and the poles of each component of the above equation, respectively, are represented according to the following equalities:

$$\begin{aligned} \alpha_I[z] &= a_{re,1} + (b_{re,1} - m_{re,1}a_{re,1} + m_{im,2}a_{im,1})z^{-1}, \\ \beta_I[z] &= a_{im,2} + (b_{im,1} - m_{re,1}a_{im,2} - m_{im,2}a_{re,2})z^{-1}, \\ \varepsilon_I[z] &= 1 - m_{re,1}z^{-1}, \\ \eta_I[z] &= m_{im,2}z^{-1}, \\ \rho_I[z] &= (g_{im,2} + m_{im,2})z^{-1}, \\ \gamma_I[z] &= 1 - (g_{re,1} + m_{re,1})z^{-1}. \end{aligned} \tag{5.5}$$

Above $\alpha_I[z]$, $\beta_I[z]$, $\varepsilon_I[z]$, $\eta_I[z]$, and $\rho_I[z]$ define the zeros of the multipliers of the I branch input, the Q branch input, the I branch quantization noise, the Q branch quantization noise and the Q branch output, respectively. These together form the signal in the I branch output. The coefficient $\gamma_I[z]$ presents the pole and is common to all the terms of (5.4). When combining (5.4) and (5.5) the equation for the I branch output $V_I[z]$ is reduced to the form

$$V_I[z] = \frac{\alpha_I[z]}{\gamma_I[z]}U_I[z] - \frac{\beta_I[z]}{\gamma_I[z]}U_Q[z] + \frac{\varepsilon_I[z]}{\gamma_I[z]}E_I[z] + \frac{\eta_I[z]}{\gamma_I[z]}E_Q[z] - \frac{\rho_I[z]}{\gamma_I[z]}V_Q[z]. \tag{5.6}$$

At the same time, the *Z*-domain output for the Q-branch can be derived, resulting in

$$\begin{aligned} V_Q[z] = & \frac{a_{im,1} + (b_{im,1} - m_{re,2}a_{im,1} - m_{im,1}a_{re,1})z^{-1}}{1 - (g_{re,2} + m_{re,2})z^{-1}}U_I[z] \\ & + \frac{a_{re,2} + (b_{re,2} - m_{re,2}a_{re,2} + m_{im,1}a_{im,2})z^{-1}}{1 - (g_{re,2} + m_{re,2})z^{-1}}U_Q[z] \\ & - \frac{m_{im,1}z^{-1}}{1 - (g_{re,2} + m_{re,2})z^{-1}}E_I[z] + \frac{1 - m_{re,2}z^{-1}}{1 - (g_{re,2} + m_{re,2})z^{-1}}E_Q[z] \\ & + \frac{(g_{im,1} + m_{im,1})z^{-1}}{1 - (g_{re,2} + m_{re,2})z^{-1}}V_I[z]. \end{aligned} \tag{5.7}$$

Again new notation is introduced to simplify the presentation, similarly as for the I branch output. Later following notations are used:

$$\begin{aligned} \alpha_Q[z] &= a_{re,2} + (b_{re,2} - m_{re,2}a_{re,2} + p_{im,1}a_{im,2})z^{-1}, \\ \beta_Q[z] &= a_{im,1} + (b_{im,1} - m_{re,2}a_{im,1} - m_{im,1}a_{re,1})z^{-1}, \\ \varepsilon_Q[z] &= 1 - m_{re,2}z^{-1}, \\ \eta_Q[z] &= m_{im,1}z^{-1}, \\ \rho_Q[z] &= (g_{im,1} + m_{im,1})z^{-1}, \\ \gamma_Q[z] &= 1 - (g_{re,2} + m_{re,2})z^{-1}. \end{aligned} \tag{5.8}$$

Above $\alpha_Q[z]$, $\beta_Q[z]$, $\varepsilon_Q[z]$, $\eta_Q[z]$, and $\rho_Q[z]$ define the zeros of the multipliers of the Q branch input, the I branch input, the Q branch quantization noise, the I branch quantization noise and the I branch output, respectively, which altogether form the signal in the Q branch output. Coefficient $\gamma_Q[z]$ presents the pole and is common to all the terms

of (5.7). Again when combining (5.7) and (5.8) the equation for Q-branch output $V_Q[z]$ is simplified to a form

$$V_Q[z] = \frac{\beta_Q[z]}{\gamma_Q[z]}U_I[z] + \frac{\alpha_Q[z]}{\gamma_Q[z]}U_Q[z] + \frac{\varepsilon_Q[z]}{\gamma_Q[z]}E_Q[z] - \frac{\eta_Q[z]}{\gamma_Q[z]}E_I[z] + \frac{\rho_Q[z]}{\gamma_Q[z]}V_I[z]. \quad (5.9)$$

Now both the outputs, $V_I[z]$ and $V_Q[z]$, depend on the previous values of each other. In order to modify the equations to a usable form some more substitutions are needed. When replacing the $V_Q[z]$ term in (5.7) with (5.9) we end up to a following equation for the I branch output:

$$\begin{aligned} V_I[z] = &\frac{\gamma_Q[z]\alpha_I[z] - \rho_I[z]\beta_Q[z]}{\gamma_I[z]\gamma_Q[z] + \rho_I[z]\rho_Q[z]}U_I[z] - \frac{\gamma_Q[z]\beta_I[z] + \rho_I[z]\alpha_Q[z]}{\gamma_I[z]\gamma_Q[z] + \rho_I[z]\rho_Q[z]}U_Q[z] \\ &+ \frac{\gamma_Q[z]\varepsilon_I[z] + \rho_I[z]\eta_Q[z]}{\gamma_I[z]\gamma_Q[z] + \rho_I[z]\rho_Q[z]}E_I[z] - \frac{\rho_I[z]\varepsilon_Q[z] - \gamma_Q[z]\eta_I[z]}{\gamma_I[z]\gamma_Q[z] + \rho_I[z]\rho_Q[z]}E_Q[z], \end{aligned} \quad (5.10)$$

which describes the dependency of I branch output $V_I[z]$ on I branch input $U_I[z]$, Q branch input $U_Q[z]$, I branch quantization error $E_I[z]$ and Q branch quantization error $E_Q[z]$.

On the other hand, substituting $V_I[z]$ of (5.6) to (5.9) gives a following form for $V_Q[z]$:

$$\begin{aligned} V_Q[z] = &\frac{\gamma_I[z]\beta_Q[z] + \rho_Q[z]\alpha_I[z]}{\gamma_I[z]\gamma_Q[z] + \rho_Q[z]\rho_I[z]}U_I[z] + \frac{\gamma_I[z]\alpha_Q[z] - \rho_Q[z]\beta_I[z]}{\gamma_I[z]\gamma_Q[z] + \rho_Q[z]\rho_I[z]}U_Q[z] \\ &+ \frac{\rho_Q[z]\varepsilon_I[z] - \gamma_I[z]\eta_Q[z]}{\gamma_I[z]\gamma_Q[z] + \rho_Q[z]\rho_I[z]}E_I[z] + \frac{\gamma_I[z]\varepsilon_Q[z] + \rho_Q[z]\eta_I[z]}{\gamma_I[z]\gamma_Q[z] + \rho_Q[z]\rho_I[z]}E_Q[z]. \end{aligned} \quad (5.11)$$

Above the Q branch output $V_Q[z]$ is given similarly as $V_I[z]$ was in (5.10).

Now the complex output signal $V[z]$ of the modulator can be formed by having $V_I[z]$ as the real part and $V_Q[z]$ as the imaginary part. Output of the modulator is thus given by

$$V[z] = V_I[z] + jV_Q[z]. \quad (5.12)$$

Now, Combining (5.10) and (5.11) as shown in (5.12) results in the following equation for the complex-valued output of the modulator:

$$
\begin{aligned}
V[z] = & \frac{\gamma_Q[z]\alpha_I[z] - \rho_I[z]\beta_Q[z]}{\gamma_I[z]\gamma_Q[z] + \rho_I[z]\rho_Q[z]} U_I[z] - \frac{\gamma_Q[z]\beta_I[z] + \rho_I[z]\alpha_Q[z]}{\gamma_I[z]\gamma_Q[z] + \rho_I[z]\rho_Q[z]} U_Q[z] \\
& + \frac{\gamma_Q[z]\varepsilon_I[z] + \rho_I[z]\eta_Q[z]}{\gamma_I[z]\gamma_Q[z] + \rho_I[z]\rho_Q[z]} E_I[z] - \frac{\rho_I[z]\varepsilon_Q[z] - \gamma_Q[z]\eta_I[z]}{\gamma_I[z]\gamma_Q[z] + \rho_I[z]\rho_Q[z]} E_Q[z] \\
& + j\left[\frac{\gamma_I[z]\beta_Q[z] + \rho_Q[z]\alpha_I[z]}{\gamma_I[z]\gamma_Q[z] + \rho_I[z]\rho_Q[z]} U_I[z] + \frac{\gamma_I[z]\alpha_Q[z] - \rho_Q[z]\beta_I[z]}{\gamma_I[z]\gamma_Q[z] + \rho_I[z]\rho_Q[z]} U_Q[z] \right. \\
& \left. + \frac{\rho_Q[z]\varepsilon_I[z] - \gamma_I[z]\eta_Q[z]}{\gamma_I[z]\gamma_Q[z] + \rho_I[z]\rho_Q[z]} E_I[z] + \frac{\gamma_I[z]\varepsilon_Q[z] + \rho_Q[z]\eta_I[z]}{\gamma_I[z]\gamma_Q[z] + \rho_I[z]\rho_Q[z]} E_Q[z] \right].
\end{aligned}
\tag{5.13}
$$

Taking the conjugation effect due to the nonideal matching of the branches into account according to (2.9), (5.13) can be further modified to

$$
\begin{aligned}
V[z] = & \left[\frac{\gamma_Q[z]\alpha_I[z] + \gamma_I[z]\alpha_Q[z] - \rho_Q[z]\beta_I[z] - \rho_I[z]\beta_Q[z]}{2(\gamma_I[z]\gamma_Q[z] + \rho_I[z]\rho_Q[z])} \right. \\
& \left. + j\frac{\rho_I[z]\alpha_Q[z] + \rho_Q[z]\alpha_I[z] + \gamma_Q[z]\beta_I[z] + \gamma_I[z]\beta_Q[z]}{2(\gamma_I[z]\gamma_Q[z] + \rho_I[z]\rho_Q[z])} \right] U[z] \\
& + \left[\frac{\gamma_Q[z]\alpha_I[z] - \gamma_I[z]\alpha_Q[z] + \rho_Q[z]\beta_I[z] - \rho_I[z]\beta_Q[z]}{2(\gamma_I[z]\gamma_Q[z] + \rho_I[z]\rho_Q[z])} \right. \\
& \left. + j\frac{\rho_Q[z]\alpha_I[z] - \rho_I[z]\alpha_Q[z] + \gamma_I[z]\beta_Q[z] - \gamma_Q[z]\beta_I[z]}{2(\gamma_I[z]\gamma_Q[z] + \rho_I[z]\rho_Q[z])} \right] U^*[z^*] \\
& + \left[\frac{\gamma_Q[z]\varepsilon_I[z] + \gamma_I[z]\varepsilon_Q[z] + \rho_I[z]\eta_Q[z] + \rho_Q[z]\eta_I[z]}{2(\gamma_I[z]\gamma_Q[z] + \rho_I[z]\rho_Q[z])} \right. \\
& \left. + j\frac{\rho_I[z]\varepsilon_Q[z] + \rho_Q[z]\varepsilon_I[z] - \gamma_Q[z]\eta_I[z] - \gamma_I[z]\eta_Q[z]}{2(\gamma_I[z]\gamma_Q[z] + \rho_I[z]\rho_Q[z])} \right] E[z] \\
& + \left[\frac{\gamma_Q[z]\varepsilon_I[z] - \gamma_I[z]\varepsilon_Q[z] + \rho_I[z]\eta_Q[z] - \rho_Q[z]\eta_I[z]}{2(\gamma_I[z]\gamma_Q[z] + \rho_I[z]\rho_Q[z])} \right. \\
& \left. + j\frac{\gamma_Q[z]\eta_I[z] - \gamma_I[z]\eta_Q[z] + \rho_Q[z]\varepsilon_I[z] - \rho_I[z]\varepsilon_Q[z]}{2(\gamma_I[z]\gamma_Q[z] + \rho_I[z]\rho_Q[z])} \right] E^*[z^*].
\end{aligned}
\tag{5.14}
$$

Now it is straightforward to distinguish the original non-conjugate ($U[z]$, $E[z]$) and conjugate ($U^*[z^*]$, $E^*[z^*]$) terms in (5.14). These $U^*[z^*]$ and $E^*[z^*]$ are the possible interference components, whose power should reduce to zero in case of perfect I/Q balance.

Still, the above equation can be simplified by denoting the differential error between the zeros and poles of the branches with a subscript *diff*. At the same time, the nominal value and the common-mode error are then combined to a multiplier of the non-conjugated terms with a subscript *nom*. Thus, based on (2.10) and (2.11) the equation takes the form

$$
\begin{aligned}
V[z] = & \frac{(\gamma\alpha)_{nom}[z] - (\rho\beta)_{nom}[z] + j[(\rho\alpha)_{nom}[z] + (\gamma\beta)_{nom}[z]]}{\gamma^2_{nom}[z] - \gamma^2_{diff}[z] + \rho^2_{nom}[z] - \rho^2_{diff}[z]} U[z] \\
& + \frac{(\gamma\alpha)_{diff}[z] - (\rho\beta)_{diff}[z] + j[(\rho\alpha)_{diff}[z] + (\gamma\beta)_{diff}[z]]}{\gamma^2_{nom}[z] - \gamma^2_{diff}[z] + \rho^2_{nom}[z] - \rho^2_{diff}[z]} U^*[z^*] \\
& + \frac{(\gamma\varepsilon)_{nom}[z] + (\rho\eta)_{nom}[z] + j[(\rho\varepsilon)_{nom}[z] - (\gamma\eta)_{nom}[z]]}{\gamma^2_{nom}[z] - \gamma^2_{diff}[z] + \rho^2_{nom}[z] - \rho^2_{diff}[z]} E[z] \\
& + \frac{(\gamma\varepsilon)_{diff}[z] + (\rho\eta)_{diff}[z] + j[(\rho\varepsilon)_{diff}[z] - (\gamma\eta)_{diff}[z]]}{\gamma^2_{nom}[z] - \gamma^2_{diff}[z] + \rho^2_{nom}[z] - \rho^2_{diff}[z]} E^*[z^*],
\end{aligned}
\tag{5.15}
$$

where $(\cdot\cdot)_{nom}$ and $(\cdot\cdot)_{diff}$ denote the nominal value (including the common-mode error) and the differential error of the product of the terms inside the brackets, respectively. Now it can be seen that the lines of (5.15) correspond to the transfer functions of the modulator, namely STF, ISTF, NTF and INTF, respectively. It is also worth noting that ISTF and INTF, given by

$$
ISTF[z] = \frac{(\gamma\alpha)_{diff}[z] - (\rho\beta)_{diff}[z] + j\big[(\rho\alpha)_{diff}[z] + (\gamma\beta)_{diff}[z]\big]}{\gamma^2_{nom}[z] - \gamma^2_{diff}[z] + \rho^2_{nom}[z] - \rho^2_{diff}[z]} \tag{5.16}
$$

and

$$
INTF[z] = \frac{(\gamma\varepsilon)_{diff}[z] + (\rho\eta)_{diff}[z] + j[(\rho\varepsilon)_{diff}[z] - (\gamma\eta)_{diff}[z]]}{\gamma^2_{nom}[z] - \gamma^2_{diff}[z] + \rho^2_{nom}[z] - \rho^2_{diff}[z]} \tag{5.17}
$$

reduce to zero in case of perfect matching between the branches. This is obviously indicated by the numerators of the image transfer functions, which consist of the differential error terms only.

Image rejection ratio of the modulator can be now found based on the four transfer functions. Input signal and quantization noise IRR are given by

$$
IRR_{STF}(e^{j2\pi fT_S}) = \frac{\left|STF(e^{j2\pi fT_S})\right|^2}{\left|ISTF(e^{j2\pi fT_S})\right|^2} \tag{5.18}
$$

and

$$
IRR_{NTF}(e^{j2\pi fT_S}) = \frac{\left|NTF(e^{j2\pi fT_S})\right|^2}{\left|INTF(e^{j2\pi fT_S})\right|^2}, \tag{5.19}
$$

respectively.

More detailed analysis, based on (5.18) and (5.19), will be given in the following subchapters separately for the flat STF and an experimental mirror frequency rejecting STF design, respectively. The effect of the latter design is studied as a mirror-frequency interference mitigation method.

5.2. IRR Analysis and Interpretations with Flat STF Design

In this Section, STF, ISTF, NTF and INTF will be illustrated in different mismatch scenarios based on the analysis in Section 5.1. These functions are derived for the modulator having ideally a unity STF and NTF notch at a frequency $\overline{f}_{pass} = 0.375$ relative to the sampling frequency. The unity STF is achieved with following complex gain values: $A = 1$, $B = MA$ and $G = -M$, based on (4.6). At the same time, M is selected to tune the notch of the NTF (now $M = e^{j2\pi\overline{f}_{pass}}$). Mismatch effects will be considered both from the noise shaping effectiveness and signal distortion point of view. IRR values are given for the STF and the NTF when appropriate.

The STF and the NTF affecting the original non-conjugated version of the input and the quantization noise are marked with the solid lines in the following transfer function figures. The dashed lines present the ISTF and the INTF, if such are non-zero in a certain mismatch scenario. Based on the transfer functions for the original and the conjugated signal, the IRRs are calculated and presented in the separate figures for the respective case. In the figures, the assumed desired signal band is marked with solid black line.

5.2.1. Effects of Input Coefficient Mismatches

A mismatch between the gains and the phases of the I and Q rails in the modulator input branches results in a conjugate response of the original input signal in the modulator output. These mismatches don't affect the noise shaping properties, because quantization noise is not processed in these parts.

First, the phenomenon is studied in a case, where the mismatch is in the gains of the branches feeding the input straight to the quantizer. This gain has been previously marked with A. In case of the frequency flat STF, this coefficient is all real and ideally unity. With mismatch Δ_A, the realized gains are $a_{re,1} = (1 + \Delta_A)a_{re}$ and $a_{re,2} = (1 - \Delta_A)a_{re}$, where a_{re} is the ideal real part and $a_{re,1}$ and $a_{re,2}$ are the mis-

matched implementation values in the I and Q branches, respectively. Resulting STF, ISTF and NTF with 10 % mismatch, to emphasize the effects, are presented in Figure 5.2. As seen on the left in the figure below, the ISTF notch is rejecting the conjugate signal energy at specified desired signal band (marked with black lines). This behavior is thus diminishing mirror frequency interference from the negative frequencies, emerging from the image band. As a result, this shape can also be seen in the IRR presented in Figure 5.3. It should also be noted that no INTF response is visible in Figure 5.2. This is because the quantization noise isn't processed in the input branches of the modulator.

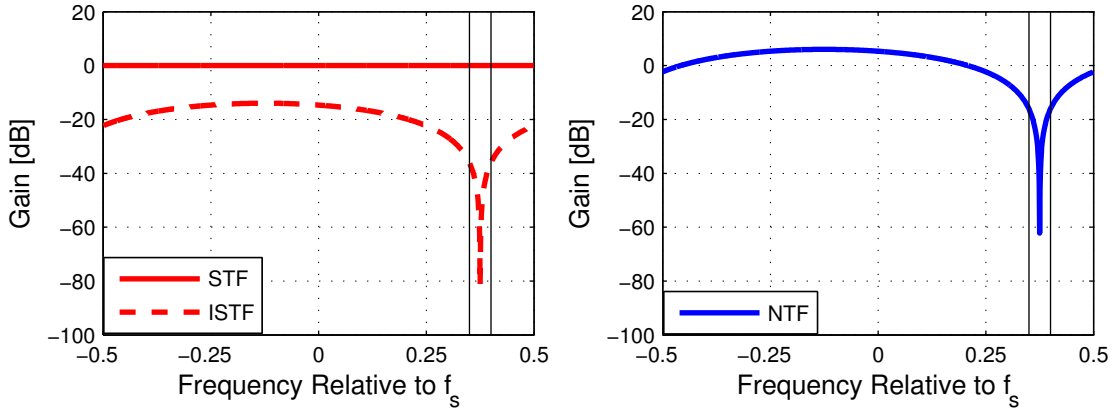

Figure 5.2 *The modulator STF and ISTF (left) and the modulator NTF (right) with 10 % mismatch in the input branch feeding the signal to the quantizer (A). The INTF doesn't exist because the mismatch in question doesn't affect the noise shaping.*

The frequency flat STF and the ISTF with a notch shape the IRR to give high values exactly on the NTF notch band, which is considered to include the desired signal. Thus, it can be said that the considered modulator structure itself is mitigating imbalance effects from the desired signal point of view in case of mismatch in the quantizer-feeding branch.

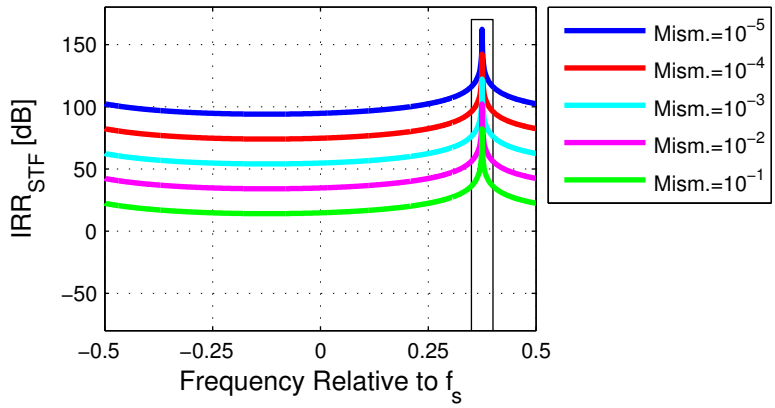

Figure 5.3 *Signal IRR as a function of frequency relative to f_S with mismatch in the input branch feeding the signal to the quantizer (A).*

The following case highlights the effects of the mismatch between the rails in the branch feeding the signal to the loop filter. Ideally, the complex gain value B in the branch is the same as M in the feedback of the complex loop integrator. In case of the quadrature modulator the integrator feedback gain and thus also the input gain B, are both complex valued, when considering non-zero NTF notch frequencies. With mismatch Δ_B the implementation values are as follows: $b_{re,1} = (1 + \Delta_B)b_{re}$, $b_{re,2} = (1 - \Delta_B)b_{re}$, $b_{im,1} = (1 + \Delta_B)b_{im}$ and $b_{im,2} = (1 - \Delta_B)b_{im}$. Symmetric mismatches in both real and imaginary parts were chosen for simplicity of analysis. However, it was confirmed in simulations that no significant differences appear between the mirroring effects with symmetric and asymmetric mismatches. Thus, the choice of symmetricity is considered just. This applies also in the forthcoming scenarios.

Based on the plots presented in Figure 5.4 it can be concluded that the mismatch in this branch does cause mirror interference for the input signal with 20 dB attenuation per matching decade. No conjugate version of quantization noise is present in this case either.

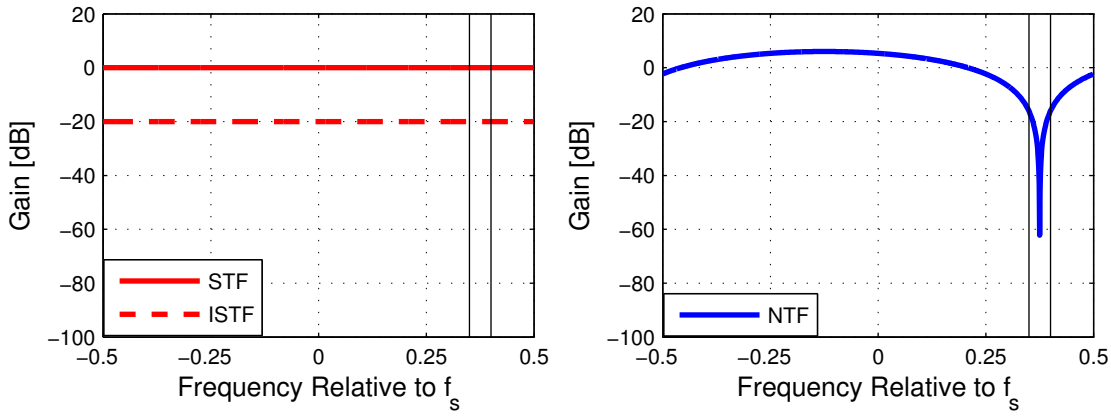

Figure 5.4 *The modulator STF and ISTF (left) and the modulator NTF (right) with 10 % mismatch in the input branch feeding the signal to the loop filter (B). The INTF doesn't exist, because the mismatch in question doesn't affect the noise shaping.*

The STF and the ISTF given above result in the IRR presented in Figure 5.5. With 10 % mismatch the IRR is frequency flat 20 dB and while the matching gets more precise, IRR values increase with a constant 20 dB per decade rate. Based on these results it can be said, that mismatch in the branch feeding the loop filter is causing frequency flat mirror frequency distortion when considering the input signal. The attenuation of the conjugate signal is straightforwardly dependent on the matching of the gain values. No con-

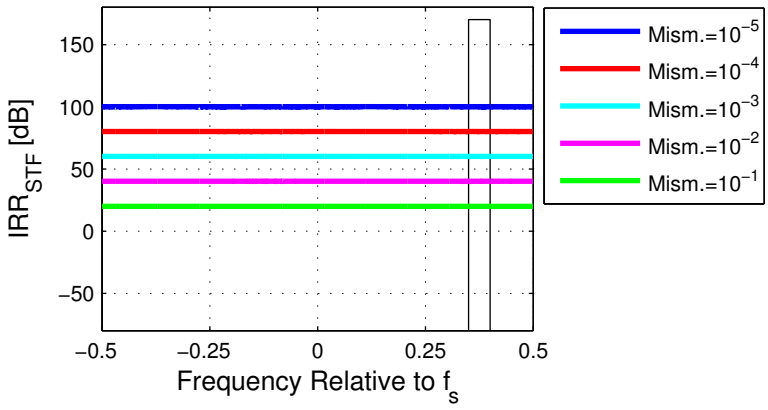

Figure 5.5 *Signal IRR as a function of frequency relative to* f_S *with mismatch in the input branch feeding the signal to the loop filter (* B *).*

jugate noise is present due to this phenomenon as was the case in both the input branches.

5.2.2. Effect of Loop Filter Mismatch

The main difference in case of loop filter coefficient mismatch compared to the two cases of the input mismatches presented in Sub-section 5.2.1 is that no conjugate response of the input signal is generated. This holds for the unity STF structure when the circuitry is considered otherwise ideal but for the mismatch in question. Now, with the mismatch Δ_M the nonideal real and imaginary parts result in the following: $m_{re,1} = (1+\Delta_M)m_{re}$, $m_{re,2} = (1-\Delta_M)m_{re}$, $m_{im,1} = (1+\Delta_M)m_{im}$ and $m_{im,2} = (1-\Delta_M)m_{im}$.

Image transfer function exists only for the quantization noise and is presented on the right in Figure 5.6 in case of 10 % mismatch between the real coefficients of the I and Q rails. The resulting INTF is frequency flat as can be seen from the below plot. This means that the conjugated version of the noise is seen in the output of the modulator without any selectivity. Thus, with relatively high values of mismatch the conjugate noise can be more significant on the desired signal band than the original non-conjugated noise, which is shaped by the noise transfer function. As a practical example, assume 60 dB of noise attenuation for the original NTF notch and −20 dB noise IRR at the desired band, thus the conjugated quantization noise signal is attenuated by only 60−20=40 dB defining the overall noise floor level in this case. In addition, it should be noted that 0 dB NTF IRR at the desired band indicates that the levels of the

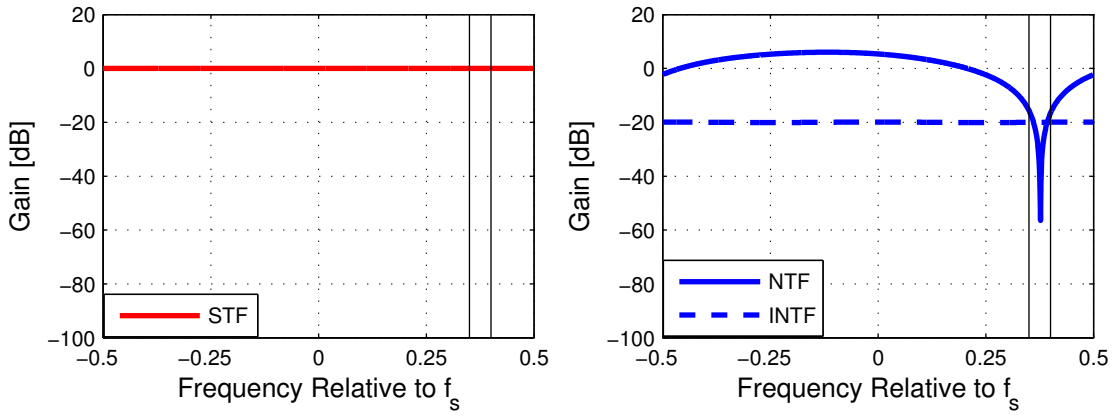

Figure 5.6 *The modulator STF (left) and the modulator NTF and INTF (right) with 10 % mismatch in the loop filter (M). The ISTF doesn't exist in this case, because the signal isn't fed through the loop filter.*

original noise and the mirrored noise are similar, which, in case of efficient noise shaping, means that both are well attenuated.

One thing to note also is that the frequency of the NTF notch is slightly transformed from the original 0.375 normalized frequency to around 0.377. This, of course, degrades the noise shaping characteristics, when compared to ideal case. With extreme case of 50 % mismatch the notch frequency exceeds 0.4 and the notch is lowered to give only 20 dB of attenuation.

In the absence of the image signal transfer function, the IRR for quantization error can be evaluated based on the noise transfer functions, or on the other hand the attenuation can be assumed to be infinite. This is given in Figure 5.7. The negative IRR values on the NTF notch frequency present the situation where the response of the INTF is larger than NTF's and thus conjugated noise has less attenuation, as stated also above.

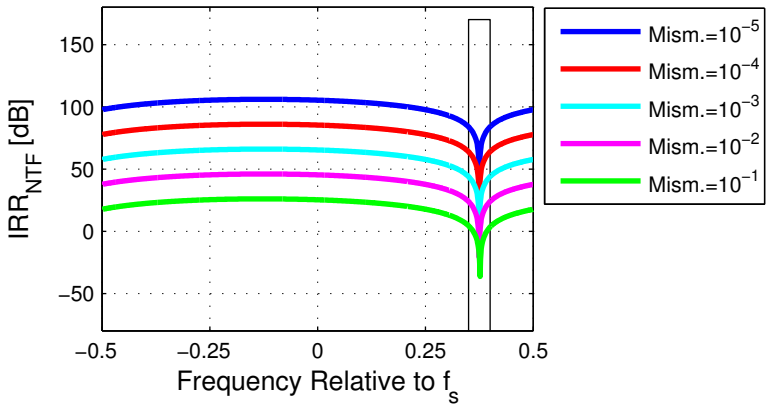

Figure 5.7 *Quantization noise IRR as a function of the frequency relative to f_S with a mismatch in the loop filter (M).*

5.2.3. Effect of Feedback Coefficient Mismatch

In case of modulator feedback branch I/Q imbalance, both the input signal and the quantization noise are causing mirror frequency interference. Here the mismatch source is assumed to be the complex multiplier G, wherein the mismatch Δ_G in the implementation results in the following values: $g_{re,1} = (1 + \Delta_G)g_{re}$, $g_{re,2} = (1 - \Delta_G)g_{re}$, $g_{im,1} = (1 + \Delta_G)g_{im}$ and $g_{im,2} = (1 - \Delta_G)g_{im}$.

While having a frequency flat STF, also the ISTF appears frequency flat, as demonstrated on the left side of Figure 5.8. Attenuation for the ISTF is increasing 20 dB per decade when matching between the branches improves. On the right side of Figure 5.8 the modulator NTF and INTF are given. The shape of the INTF is following the complex conjugate of the original NTF with some attenuation. The level of this attenuation is similar to the one seen in the case of STF and ISTF. Thus, it increases 20 dB per matching decade.

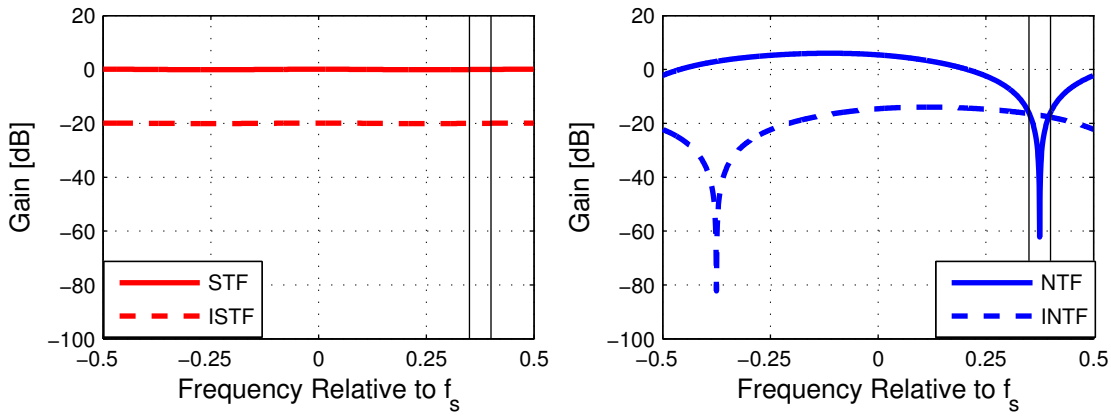

Figure 5.8 *The modulator STF and ISTF (left) and the modulator NTF and INTF (right) with a 10 % mismatch in the modulator feedback branch (G).*

As in the previous cases, the IRR values are calculated based on the transfer- and the image transfer functions. With modulator feedback mismatch both the STF and the NTF IRR values are affected and thus presented in Figure 5.9. From the below figure, it can be seen that IRR is flat in case of the input signal mirror interference, which is easily explained by the flat shape of the STF and the ISTF. The IRR is increasing with better matching of the branches and is following nicely the aforementioned 20 dB per decade rule.

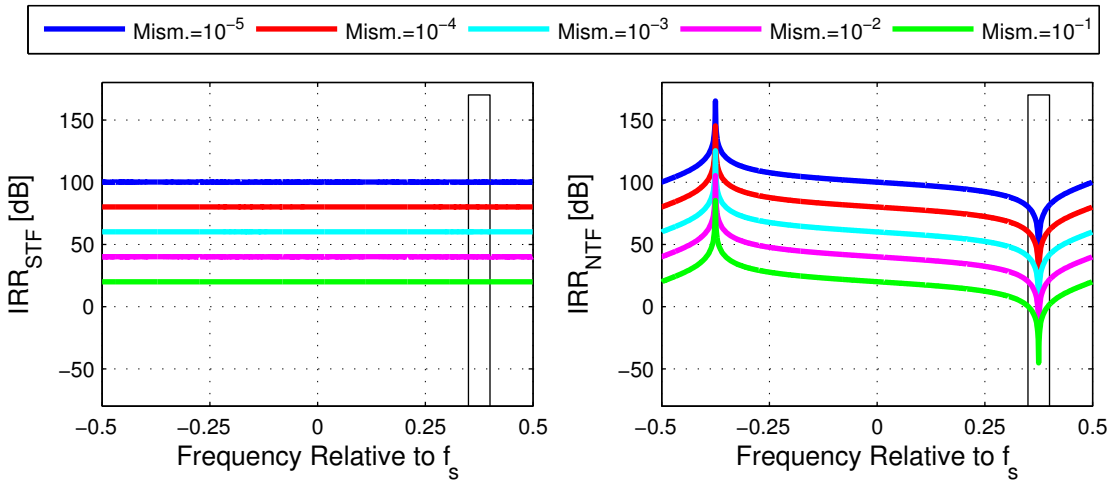

Figure 5.9 *Signal (left) and quantization noise (right) IRRs as a function of frequency relative to* f_S *with mismatch in the modulator feedback branch (*G*).*

The quantization noise IRR has high values on the mirror frequencies of the considered desired signal around 0.35 relative to f_S. This is because of the original NTF notch,which is shaping the noise away from the desired band. After this shaped noise is conjugated, there is significantly less noise power and thus less mirror interference on that frequency band. Similarly, the notch in IRR values on the desired band is explained by the relationship of original quantization noise power and the power of conjugate noise signal. There is hardly any original noise present and the conjugate signal has only attenuation of roughly 20 dB. Neither is the NTF attenuating the noise on the mirror frequencies. With high mismatch values this can lead to a situation where the conjugate noise is more severe threat to the signal quality than the original non-conjugated quantization noise.

5.3. IRR Analysis and Interpretations with Mirror Band Rejecting STF Design

In this Section the STF, ISTF, NTF and ISTF behavior will be examined in case of selective STF. The STF is designed in such a way, that there is a notch at a frequency $\overline{f}_{int} = -0.361$ relative to the sampling frequency with an assumption of a known strong blocking signal there. The chosen frequency is intentionally shifted away from the exact mirror band ($-\overline{f}_{pass} = -0.375$) of the desired signal for illustration purposes. In this way, the conjugate of the blocking signal and the original desired signal can be separated, and vice versa. This transfer function design is realized with following choic-

es of the parameters: $A = 1$, $B = M + e^{j2\pi(0.5-\bar{f}_{int})}$ and $G = -M + e^{-j2\pi\bar{f}_{pass}}/2$. At the same time $M = e^{j2\pi\bar{f}_{pass}}$ is again the placement of the NTF zero.

The purpose of the study is to demonstrate that the mirror frequency rejecting STF can be used to mitigate the I/Q imbalance effects in a quadrature ΣΔ modulator. The resulting transfer functions and IRRs are presented in similar manner as in the flat STF case in Section 5.2. In addition, the modulator mismatches are defined similarly as was done for the flat STF design above.

5.3.1. Effects of Input Coefficient Mismatches

When considering the mismatch in the input branch feeding the signal to the quantizer, the main characteristics of the ISTF remain the same with the selective STF as in the case of a frequency flat STF. This can be seen in Figure 5.10 when compared to Figure 5.2. The shape of the ISTF is slightly altered but the notch frequency remains the same. Thus, the only feature clearly affecting the IRR from input signal point of view is the STF notch, which is rejecting input power on that frequency band. The NTF is similar as in the previous cases and the INTF has infinite attenuation in this case too, because quantization noise doesn't suffer from the mismatch in question.

The STF notch effect in the IRR can be seen in Figure 5.11. The modest IRR values on the STF notch frequency band are due to the high attenuation of the input signal and the relatively low rejection of the conjugate signal. However, the frequencies being mostly

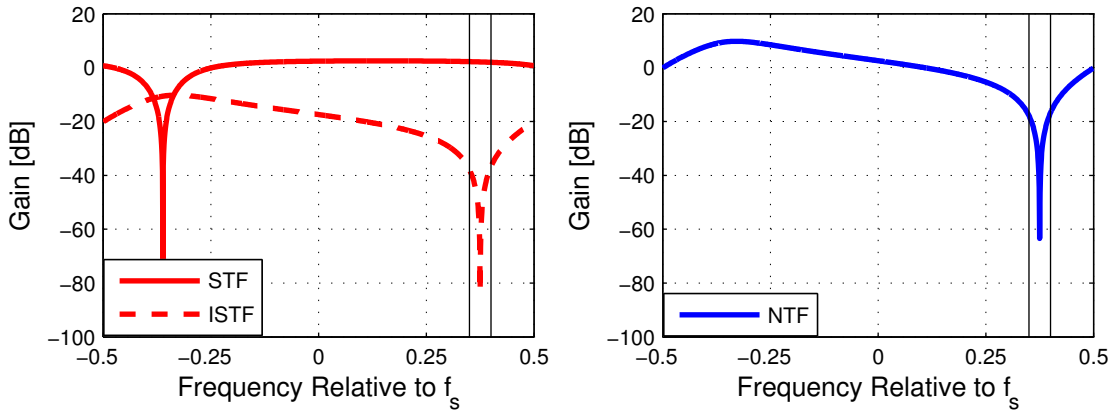

Figure 5.10 *The modulator STF and ISTF (left) and the modulator NTF (right) with a 10 % mismatch in the input branch feeding the signal to the quantizer (A). The INTF doesn't exist in this case, because the mismatch in question doesn't affect the noise shaping.*

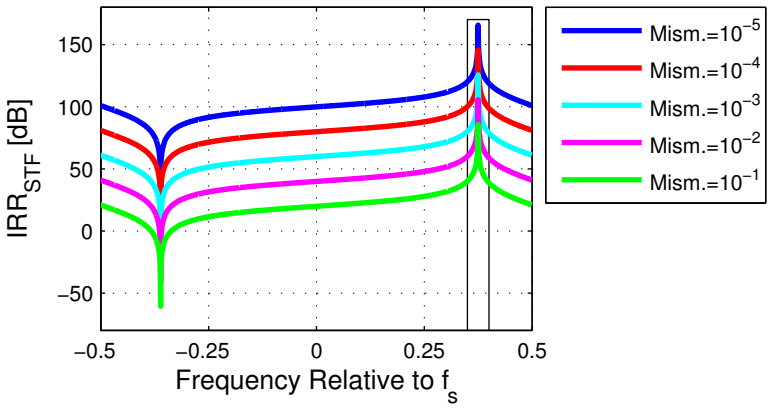

Figure 5.11 *Signal IRR as a function of the frequency relative to f_S with a mismatch in the input branch feeding the signal to the quantizer (A).*

interesting have high IRR values because of the ISTF notch on the desired band. Even with as severe as 10 % mismatch the IRR peaks at the level of 60 dB, which is usually considered adequate. From this point of view, the mismatch behavior is remarkably similar as was in the case of the flat STF, discussed in Sub-section 5.2.1.

In case of mismatch in the branch feeding the input to the loop filter and the frequency flat STF, the ISTF was similarly frequency flat as stated above. Now in the case of the notched STF, the ISTF shape is slightly altered but the main characteristics remain the same. The ISTF has the highest attenuation in the middle of the STF passband, in this case around frequencies 0.1 relative to the sampling frequency. Anyway, variations do not exceed 10 dB range even over the whole Nyquist band as can be seen from the left plot in Figure 5.12.

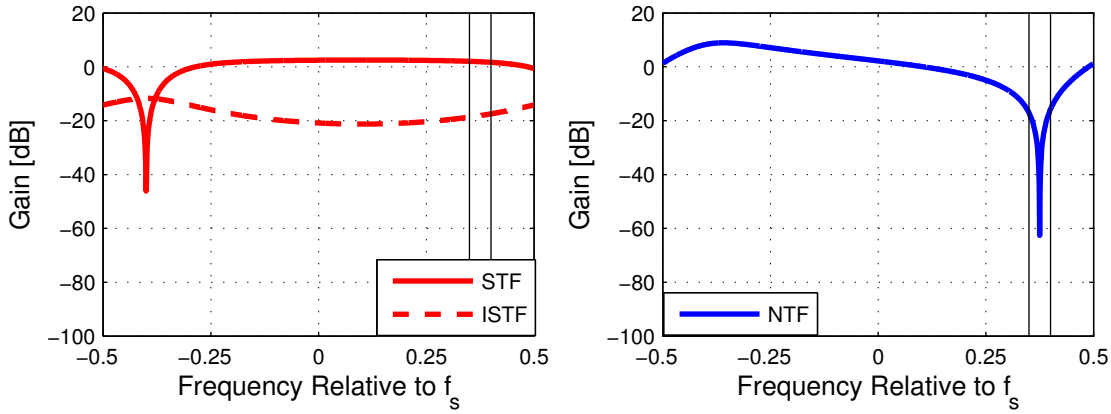

Figure 5.12 *The modulator STF and ISTF (left) and the modulator NTF (right) with a 10 % mismatch in the input branch feeding the signal to the loop filter (B). The INTF doesn't exist in this case, because the mismatch in question doesn't affect noise shaping.*

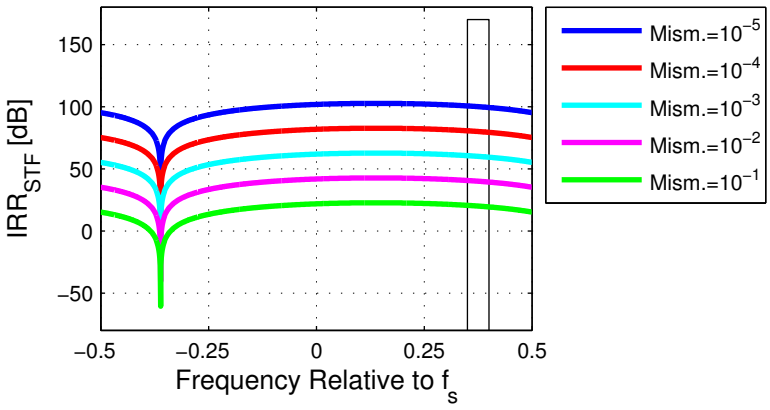

Figure 5.13 *Signal IRR as a function of the frequency relative to* f_S *with mismatch in the input branch feeding the signal to the loop filter (* B *).*

The resulting IRR curves are presented in Figure 5.13. The lower IRR values on the mirror band are due to the STF notch, which is rejecting the original input, and the relatively flat ISTF. Though, this can be seen irrelevant from the desired signal point of view, which is again assumed to be located around 0.375 relative to the sampling frequency. At that frequency band, the image rejection ratios seem to follow the 20 dB per decade rule of thumb quite nicely.

5.3.2. Effect of Loop Filter Mismatch

Designing the signal transfer function to reject the mirror frequencies affects the IRR behavior significantly in case of mismatch in the loop filter of the modulator. With the frequency flat STF in Sub-section 5.2.2, the input signal didn't suffer from mirror interference because the modulator feedback cancelled the input to the loop filter. When considering the mirror-frequency rejecting STF design this is not the case and thus the mismatch in the filter is adding a conjugate response for the input signal as well. This will be demonstrated in the following.

On the other hand, nonideal matching of the integrator coefficients is also affecting the effectiveness of the original STF and NTF. When compared to the previous cases with input branch mismatches, given above, both the notches have become lower. Attenuation in the middle of the STF notch has reduced more than 20 dB, as can be seen when comparing Figure 5.14 to the frequency flat case in Figure 5.6. The effect isn't pronounced in the same scale in the NTF, but however the alteration is notable. In addition, the frequency of the STF notch has been altered as was the case also with the flat STF in Sub-section 5.2.2.

Both the ISTF and the INTF are relatively flat as a function of the frequency in Figure 5.14, having slightly more attenuation close to the baseband. Because of the gently sloping behavior, most of the IRR characteristics are defined by the STF and the NTF, as shown in Figure 5.15. The IRR curves have notches on the frequencies of the original transfer function notches. The notches describe the rejection of the desired band quantization noise and the image band input signal power. Similarly to the previous case of the mismatch in the loop filter-feeding branch, IRR_{STF} is behaving quite smoothly on the desired signal band and giving image attenuation in the order of 20 dB per matching decade.

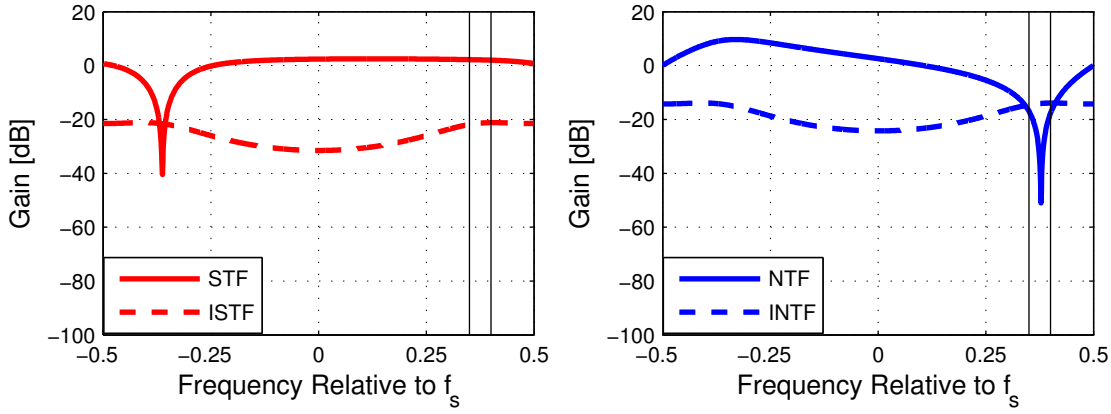

Figure 5.14 *The Modulator STF and ISTF (left) and the modulator NTF and INTF (right) with the 10 % mismatch in the loop filter (M).*

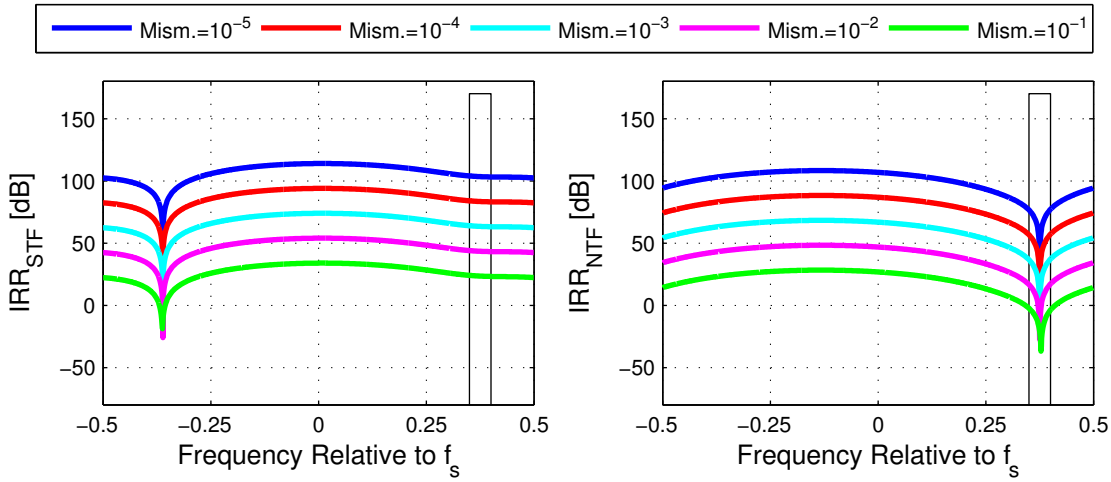

Figure 5.15 *Signal (left) and quantization noise (right) IRRs as a function of the frequency relative to f_S with mismatch in the loop filter (M).*

5.3.3. Effect of Feedback Coefficient Mismatch

The mirror frequency rejecting STF has the most effect on the generated mirror frequency distortion when considering the case of mismatched modulator feedback branch. The resulting ISTF has a notch directly on the mirror frequency of the specified STF

notch (in this case close the NTF notch). Thus, this kind of design is effectively rejecting the input based mirror interference from the opposite band of the original STF notch. This is shown in Figure 5.16 along with the noise transfer functions.

In case of mismatch in the input branch feeding the quantizer, there was similar kind of notch in the observed ISTF. The difference between these two cases is that, when considering the above input mismatch scenario the notch is directly on the desired signal band (specified by the NTF notch) whereas in this case, the ISTF notch is located at the mirror frequency of the STF notch. However, if the STF notch is designed to be on the image band of the desired signal, these two cases notch the ISTF at the same frequencies.

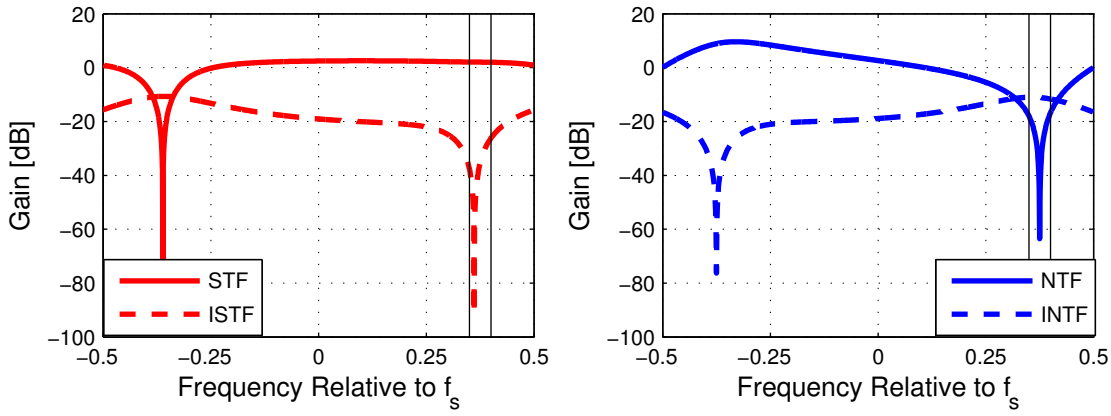

Figure 5.16 *The modulator STF and ISTF (left) and the modulator NTF and INTF (right) with the 10 % mismatch in the modulator feedback branch (G).*

The shape of the STF and the ISTF result in the input signal IRR presented in Figure 5.17. IRR peaks on the positive frequencies are due to the ISTF notch. This notch, and thus also peak IRR frequencies, can be tuned with the selection of the original STF notch frequency. This is because STF and ISTF notches are on the opposite frequencies, symmetrically around DC. From the quantization noise point of view, the situation is quite similar. The INTF notch in Figure 5.16 is on the opposite frequency when compared to the NTF notch. This results in the IRR curves plotted on the right side of Figure 5.17. The IRR values are modest on the desired band, which has been seen also in several previous cases.

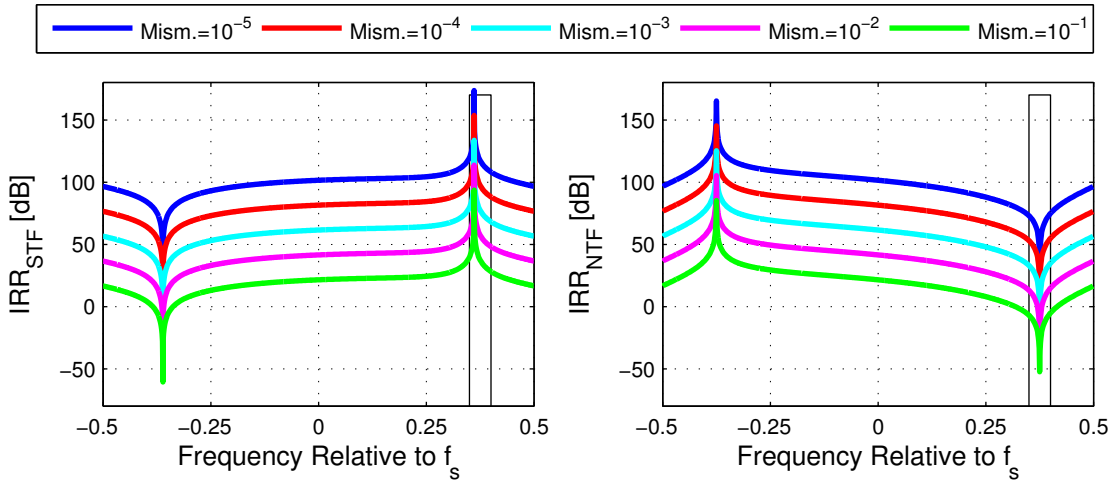

Figure 5.17 *Signal (left) and quantization noise (right) IRRs as a function of the frequency relative to* f_S *with the mismatch in the modulator feedback branch (*G*).*

6. SIMULATION EXAMPLES AND RESULTS

The purpose of this chapter is to confirm and further illustrate the previous analysis by the means of computer simulations. In this way, the validity of the derived models can be confirmed. The main emphasis is exactly on the I/Q imbalance modeling and the results are divided into Sub-sections based on the location of mismatched values. The effects of the mismatch in a first-order quadrature ΣΔ modulator are simulated based on the transfer functions derived in Chapter 5. The mismatch is modeled as an imbalance in the real gains on the I and Q rails.

In Section 6.1 the NTF simulation results are given based on the simulations on the conjugate response of the quantization noise. After that, the mirror frequency interference originating from the modulator input is reviewed in Section 6.2. Finally, in Section 6.3 the mitigation of the mirror frequency interference in quadrature ΣΔ converters is considered.

The length of the FFT employed for the spectral analysis, as well as the signal length itself, is $2^{16} = 262144$ samples. The signal is windowed with a Hann-window, whose length matches the signal length, when calculating the FFTs for the spectrum figures. The STF related IRR values given in the following are obtained based on spectral analysis and the power margin between the mirror components in question.

6.1. NTF and Quantization Noise Mirroring Study

First, the correspondence of the analytic noise transfer functions and the simulated output of the modulator is studied. The behavior of the modulator is examined with a zero-input and AWGN modeled quantization error. Thus, the noise shaping characteristics can be examined in more detail without distraction of the input signal related phenomena. The input branch mismatches don't affect the noise shaping and thus only two cases are considered: the loop filter and the feedback coefficient mismatches. The NTF and the INTF don't depend on the STF selection and thus only a flat STF is simulated. The results are averaged over 50 independent realizations of the random noise signal. The

spectra of the output noise signals in mismatched scenarios are compared to the corresponding ideal spectra. At the same time, the mismatched spectra are compared to the analytic NTFs and INTFs to examine the analogies.

With nonideal matching, depending of the INTF shape, it is possible that the conjugate response of the quantization noise becomes dominant on the desired signal band when compared to the non-conjugated noise shaped by the NTF. If the INTF is, e.g., frequency flat and additional interference is to avoided, the matching of the component values must be precise enough to give equally good attenuation for the INTF as the NTF notch has.

6.1.1. Effect of Loop Filter Mismatch

Mismatch in the feedback of the loop filter, i.e. complex integrator, produces mirror frequency interference by introducing the INTF besides the designed NTF. In addition, the described mismatch distorts the original NTF shape and transfers the notch frequency slightly off the original value.

The right side magnification on the NTF notch in Figure 6.1 shows the situation with an emphasized 10 % mismatch. The black and green spectra represent the ideal and the mismatched modulator outputs, respectively. The NTF and the INTF, the solid and the dashed blue lines, are both evaluated for the mismatched scenario based on the analysis in Chapter 5. The ideal NTF is presented with a dotted blue line for reference.

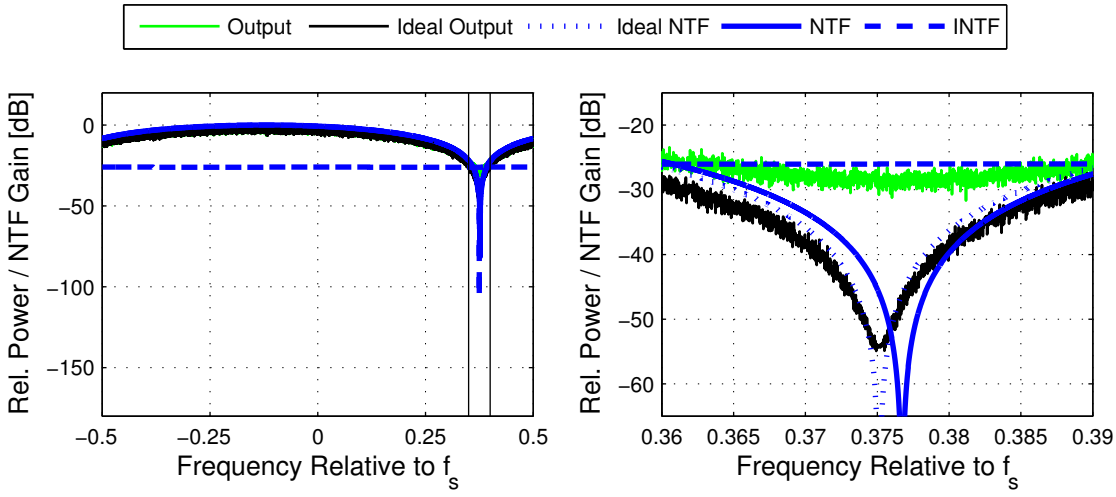

Figure 6.1 *Simulated output noise spectrum and the NTFs with 10 % mismatch in the loop filter (M). The right hand plot zoomed to the assumed desired signal band.*

From the above figure, it can be seen, that on the desired signal band, which is again assumed to be on the frequencies of the original NTF notch, the noise level is following the INTF in the mismatched case. Outside the ideal notch frequencies, the NTF is dominant and the noise level is following it neatly.

When decreasing the mismatch by a decade, the noise level clearly drops on the notch-frequencies, as is shown in Figure 6.2. In this case, the NTF is practically ideal and the continuous and dotted blue lines can hardly be separated. The figure below shows that with a 1 % mismatch the analytical NTF and INTF match with reasonable precision to the simulated noise spectrum, similarly as in the 10 % case. With this more precise matching, the INTF response has dropped 20 dB when compared to the previous case. However, the conjugate noise is still dominant inside the NTF notch.

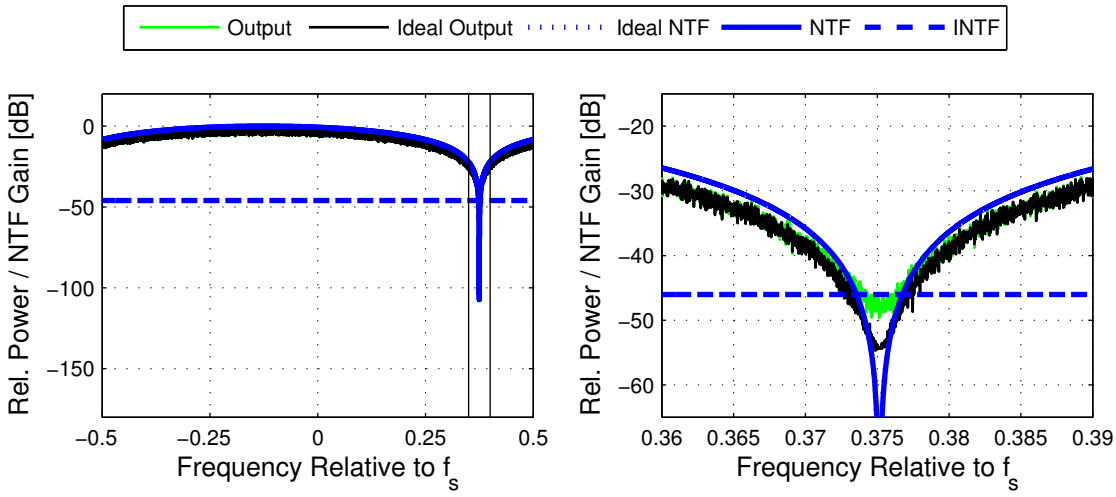

Figure 6.2 *Simulated output noise spectrum and the NTFs with 1 % mismatch in the loop filter(M). The right hand plot zoomed to the assumed desired signal band.*

Based on these observations, it can be concluded that analytical model for the NTF and the INTF holds for the case of the loop filter mismatch. The simulated noise spectra and the predicted noise transfer functions are giving coincident results.

6.1.2. Effect of Feedback Coefficient Mismatch

The main difference in the case of a mismatch in the modulator feedback branch, when compared to the loop filter mismatch discussed above, is that the NTF notch frequency remains intact. The INTF shape differs also, but when considering phenomena related to the band of the interesting signal, the findings are relatively similar.

Figure 6.3 presents the simulation results and related analytical noise transfer functions in the case of the emphasized mismatch of 10 %. The ideal output drawn with black is seen to fit well with the NTF shape. With the mismatch present, the NTF remains intact and the blue dotted line cannot be separated from the continuous one. Anyway, the mismatch generates the INTF response, which affects the output in the nonideal setup. The output noise level is dominated by the conjugate response on the interesting band, as can be seen from the magnification on the right side in the Figure 6.3.

Again, when decreasing the mismatch to 1 %, the basic phenomena remain the same. The significant change is the INTF attenuation improvement of 20 dB, which can be seen from Figure 6.4. In this case, the magnification shows the mismatched noise spec-

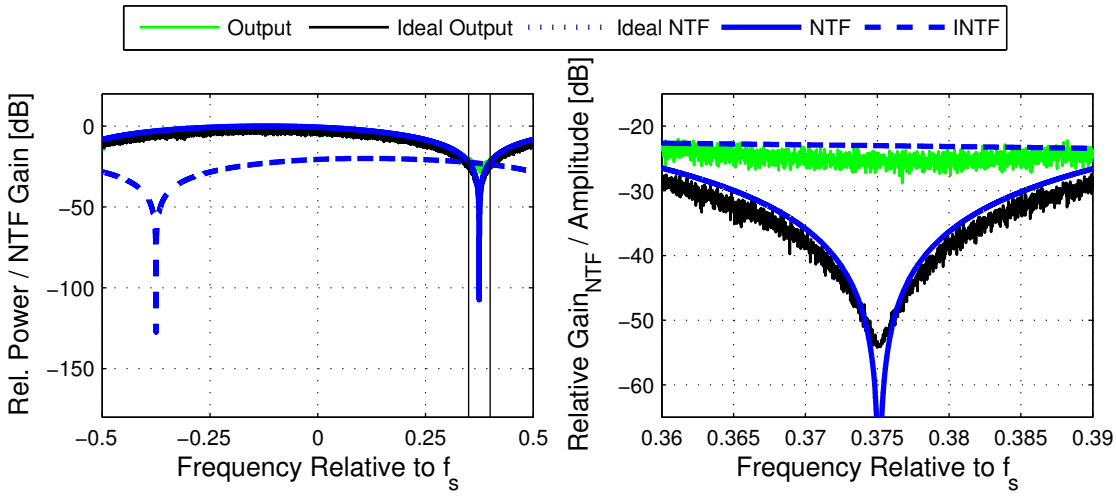

Figure 6.3 *Simulated output noise spectrum and the NTFs with 10 % mismatch in the feedback branch (G). The right hand plot zoomed to the assumed desired signal band.*

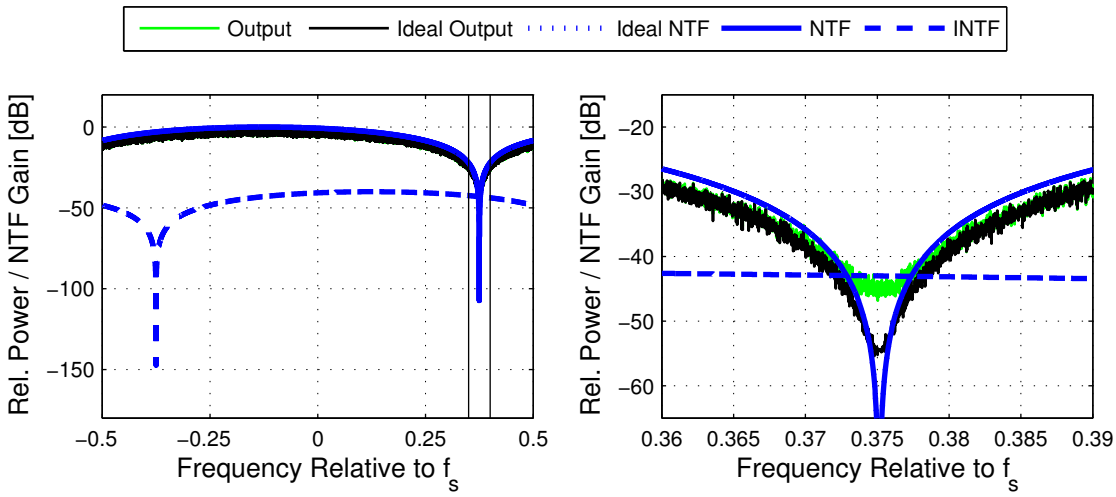

Figure 6.4 *Simulated output noise spectrum and the NTFs with 1 % mismatch in the feedback branch (G). The right hand plot zoomed to the assumed desired signal band.*

trum crossing the INTF response level on the sides of the notch due to the increasing gain of the NTF. Thus, the INTF is the most dominant in the middle of the NTF notch.

Based on the simulation results presented above, it can be said that analytical derivations considering the noise shaping characteristics, i.e. NTF and INTF response, are valid. As the main finding, the possible dominance of the conjugated version of the quantization error on the desired signal band should be highlighted.

6.2. STF and Input Signal Mirroring Study

The complex input signal used in the STF simulations consists of two exponential tones approximately at the normalized frequencies $\overline{f}_{pass} = 0.375$ and $\overline{f}_{int} = -0.361$. Spectrum of the input signal is shown in Figure 6.5.

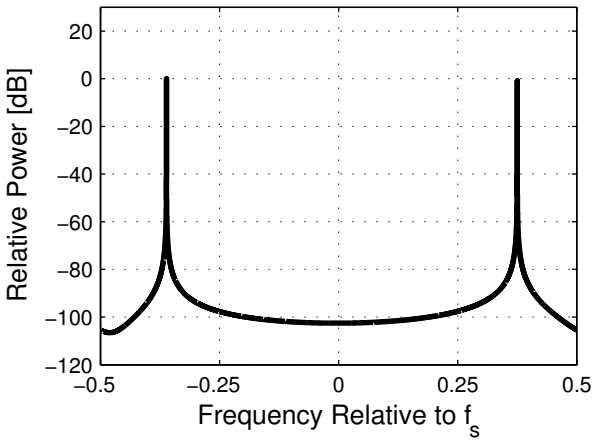

Figure 6.5 *Spectrum of the input signal used in the I/Q imbalance STF simulations, exponential tones at 0.375 and −0.361 relative to the sampling frequency.*

The NTF notch of the first-order modulator is located exactly at the frequency of the positive frequency exponential. Thus, the IRR can be estimated by measuring the difference of the frequency components at 0.375 and 0.361, which represent the original tone at the NTF passband and the mirror interference component from the negative frequency tone, respectively. The simulations were done with an ignorable level of additive noise modeling quantization error to highlight the STF related phenomena.

The IRR plots presented in the following Sub-sections represent the averaged IRR values over random phases of the exponential tones in the input signal. The data for each plot consists of 50 independent phase realizations to smoothen random variations in the acquired IRR results and thus provides more reliable data. For comparison, a spectrum

of the output with the 10 % mismatch in the input branch feeding the quantizer highlighting the phenomenon is presented in Figure 6.6. In addition, the calculated STF and ISTF are plotted.

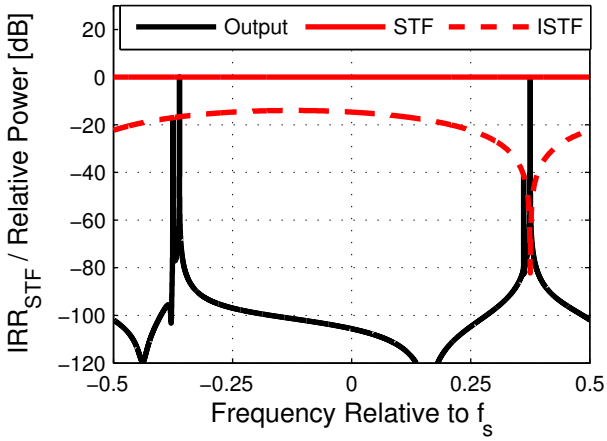

Figure 6.6 *Output spectrum of the described simulation setup with a 10 % mismatch in the input branch feedin the quantizer (A).*

From the above figure, it can be seen, that the predicted transfer functions are matching nicely with the output components. The mirror-frequency interference component is attenuated by the ISTF and the original input by the STF.

The IRR values calculated based on the analytical model are plotted in the figures in the following Sub-sections with circles and crosses for the flat and the selective case, respectively. These calculations are done at one-decade intervals. The analytical results are compared to the simulated values to find out the reliability of the analysis. The Fourier transform accuracy and the available word length are limiting perceivable image attenuation values to roughly 80 dB level. This is the level when mirror interference component is pushed to the noise level and thus cannot be observed anymore. The following simulation ranges are tuned considering this limitation.

6.2.1. Effects of Input Coefficient Mismatches

A mismatch between the coefficients on the input branches of the I and Q rails results in a conjugate response for the input signal. The image rejection ratios of the modulator with different values of the mismatch in the branch feeding the input signal to the loop filter are presented in Figure 6.7. The IRR was simulated with the all-flat STF and with the STF notch at the frequency of the interfering mirror frequency signal. These results are given with blue and red lines, respectively.

The analytical predictions of the corresponding IRR values are given with intervals of one mismatch decade. The calculated results are drawn with circles and crosses, for the flat and the mirror frequency rejecting signal transfer functions, respectively. The curves show that the results obey the traditional 20 dB per matching decade attenuation increase. Also the correspondence between the simulated and calculated values is good.

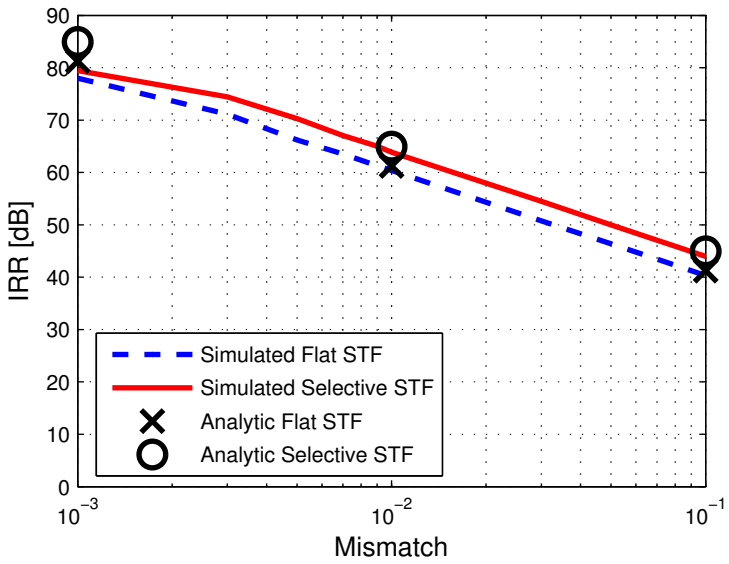

Figure 6.7 *Output IRR as a function of the mismatch in the input branch feeding the signal to the quantizer (A).*

Similarly, the IRR is simulated based on the mismatch in the branch feeding the input signal straight to the quantizer, bypassing the loop filter. These results are shown in Figure 6.8. The IRR level is roughly 20 dB lower than in the previous case, but the slope remains on the 20 dB per decade level. Just as in the previous scenario, the analytical and simulated results are coherent.

Based on the results it can be said that designing the STF notch on the mirror interference frequency doesn't decrease the experienced interference in cases of the input branch mismatches. In addition, it should be noted that the mismatch in the branch feeding the input to the loop filter is causing more rapid degradation in the IRR values when compared to mismatch in the quantizer-feeding branch. This results from the fact that parameter A is purely real gain in the simulation setup in case of both the STF de-

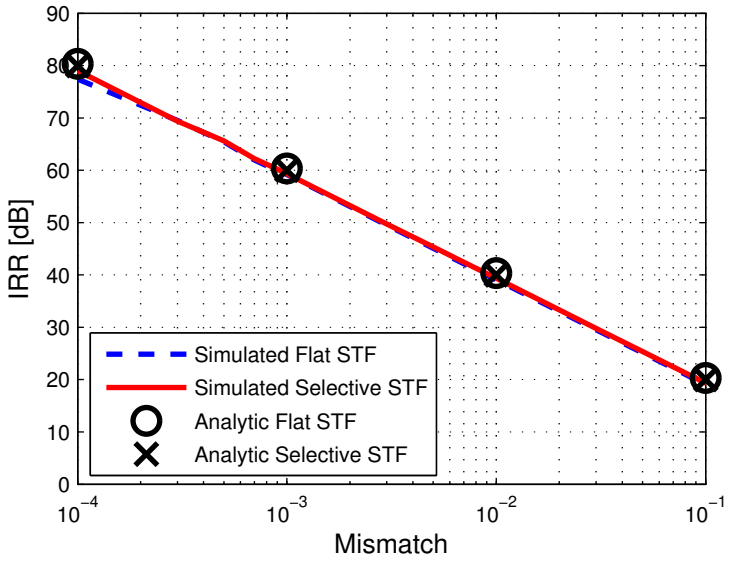

Figure 6.8 *Output IRR as a function of the mismatch in input branch feeding the signal to the loop filter (B).*

signs. Mismatch in the complex parameter B is causing more severe imbalance effects because the I and Q rails are also cross-connected, resulting in two real multiplications instead of two. This behavior was visible also in the IRR plots in Sub-sections 5.2.1 and 5.3.1.

6.2.2. Effect of Loop Filter Mismatch

The I/Q imbalance in the complex loop filter of the quadrature ΣΔ modulator results in a conjugate response in the modulator output. The mismatch is simulated as a differential error in the coefficients of the feedback gain of the complex integrator. The resulting IRR values are presented in Figure 6.9.

The below figure clearly shows that in case of selective STF the IRR slope is again 20 dB per mismatch decade. The analytic calculations marked with circles clearly agree with this. In the case of flat STF, the analytic results are in the order of hundreds of decibels. Theoretically, image attenuation should be infinite due to the reasons described earlier in Sub-section 5.2.2. Anyway, because of the limited word length effects, some high but finite values are observed. From the simulation point of view, the 80 dB floor of the IRR is resulting from, among others, the properties of the FFT.

Thus, the analytical IRR results being on such a high level and the simulation results giving values close to the maximum achievable level with used precision, the analysis can be assumed coherent. In this way, the simulations confirm the conclusion that in the

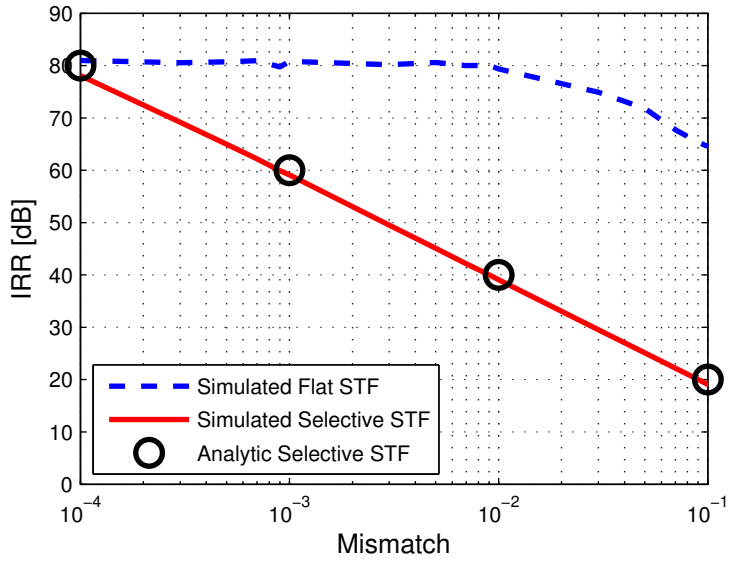

Figure 6.9 *Output IRR as a function of the mismatch in the loop filter (M).*

case of the all-flat STF, the mismatch in the feedback of the complex integrator doesn't produce conjugate interference from the input signal point of view.

6.2.3. Effect of Feedback Coefficient Mismatch

When the feedback branch of the quadrature ΣΔ modulator contains mismatch between the I and Q branches, the conjugates of both the input signal and the quantization noise are present at the output. In addition to previous analytic derivations in Sub-sections 5.2.3 and 5.3.3 for the flat and the mirror frequency rejecting STF, respectively, the mirror interference due to the input conjugation is simulated.

In the case of image-band rejecting STF, the IRR is significantly increased, as can be seen from Figure 6.10. This is because the frequency components causing the mirror interference are filtered from the signal before it is fed to the mismatched feedback branch.

With the flat STF, simulation results are clearly coherent with the analytic calculations marked with crosses in the below figure. The figure shows that in case of the feedback mismatch the IRR is significantly increased with the mirror frequency rejecting STF design. Even with 10 % mismatch the IRR remains above the 70 dB level.

The analytic IRR values for the mirror frequency rejecting STF range from slightly above 90 dB to around 150 dB with the mismatch decreasing from 10 % to 0.01 % (as was shown in Sub-section 5.3.3) and are therefore off the figure scale. The flat STF re-

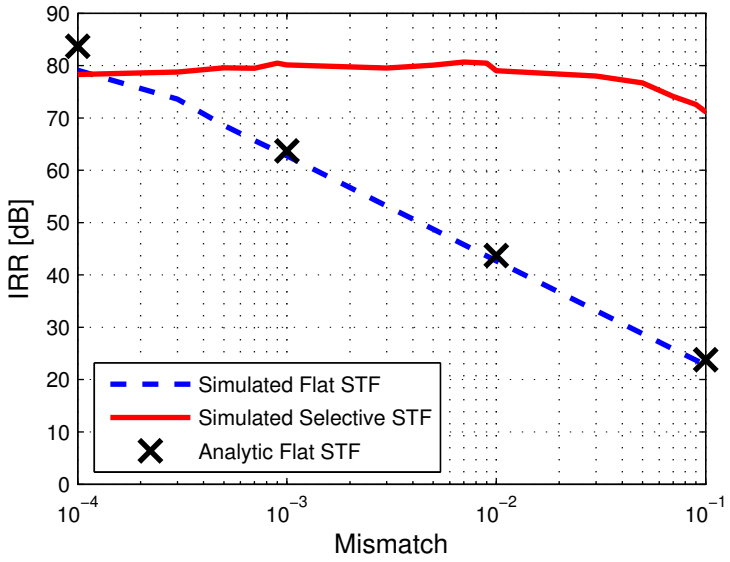

Figure 6.10 *Output IRR as a function of the mismatch in the modulator feedback branch (G).*

sults match the previous analysis considerably well, and in the case of the selective STF, the difference results from the limited simulation precision. Thus, the analytic model can be assumed valid also in this case.

6.3. Interpretations on Mirror Interference Post-Compensation

The purpose of this section is to highlight some characteristics of quadrature ΣΔ conversion related to the I/Q imbalance compensation. The imbalance is assumed to appear inside the quadrature ΣΔ modulator or in the preceding quadrature mixer applied to the down-conversion of the RF signal. Three different mismatch scenarios will be discussed below. These include a mixer mismatch with an ideal traditional A/D-conversion, a mixer mismatch with an ideal quadrature ΣΔ converter and an ideal mixer with a mismatched quadrature ΣΔ converter. The mismatch of the quadrature mixer is modeled with a gain and a phase error resulting in a 20 dB image-rejection in order to highlight the phenomenon. Similarly, the quadrature ΣΔ converter is assumed to give 20 dB IRR for the input signal, which results from the 10 % mismatch in the modulator feedback loop.

A complex exponential on a negative frequency of roughly –0.375 relative to the sampling frequency f_S is modeling a strong blocking signal on the mirror frequency of the

desired signal. Thus, the desired band is assumed to be located around +0.375 relative to f_S. In case of the quadrature ΣΔ conversion, the noise notch is located on this frequency.

The method used to compensate the mirror frequency interference is proposed in [3]. In the literature, some ΣΔ specific analog mitigation methods are proposed, but they usually include implementing additional analog electronics [12], [57] or time-sharing of the components [53]. The former affects the receiver size and power dissipation and the latter one the sampling characteristics. A digital post processing method, such as in [3], would be a desirable way to compensate possible interference, because no alteration of the original modulator structure would be needed. In this way, the characteristics of the converter wouldn't be degraded and, on the other hand, the size, the power consumption and the integrability would remain intact.

Now a block-based estimation algorithm is applied to compensate the frequency-independent interference, which is the case in the following examples. The basic principle in this algorithm is to sum a weighted version of the conjugate signal to the original signal in order to remove the interference. Anttila et al. showed this to be effective in a case of the frequency-independent mixer mismatch. The calculation of the optimum compensation factor ω_{OPT} is based on expected values of the squared signal and the squared absolute values of the signal over the chosen block of samples. Thus, ω_{OPT} is given by

$$w_{OPT} = -\frac{E\left[x(k)^2\right]}{E\left[\left|x(k)\right|^2\right] + \sqrt{E\left[\left|x(k)\right|^2\right]^2 - \left|E\left[x(k)^2\right]\right|}}, \tag{6.1}$$

where $x(k)$ is the quantized complex-valued discrete-time signal. Thereafter, ω_{OPT} is used in the compensation structure illustrated in Figure 6.11. For further details and the related derivations, interested reader is advised to the original publication [3].

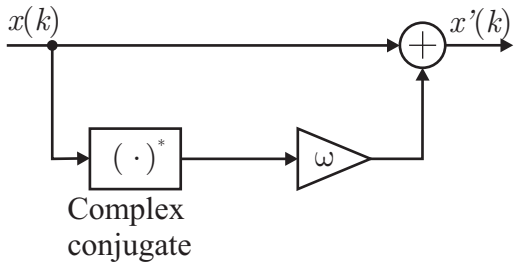

Figure 6.11 *Basic principle of the mirror frequency interference compensator in [3].*

6.3.1. Mismatched Quadrature Mixer with Traditional ADCs

The I/Q imbalance in a quadrature mixer structure results in a nonideal frequency translation. Optimally, the frequency shift is truly asymmetric with a local-oscillator frequency f_{LO}. However, the imbalance creates an attenuated mirror image, which will be transferred in the opposite direction $-f_{LO}$ in frequency. This phenomenon leads to the mirror frequency interference. For example, if we assume an IF receiver with the desired signal around the RF frequency $f_{LO} + f_{IF}$, the ideal IF for the desired signal will be $f_{LO} + f_{IF} - f_{LO} = f_{IF}$. Now we can see that the mismatched mixer creates also an interfering image from the negative frequencies with the frequency shift $-f_{LO} + f_{IF} + f_{LO} = f_{IF}$, resulting in mirror image at f_{IF} from original $-f_{LO} + f_{IF}$. This is shown graphically in Figure 6.12

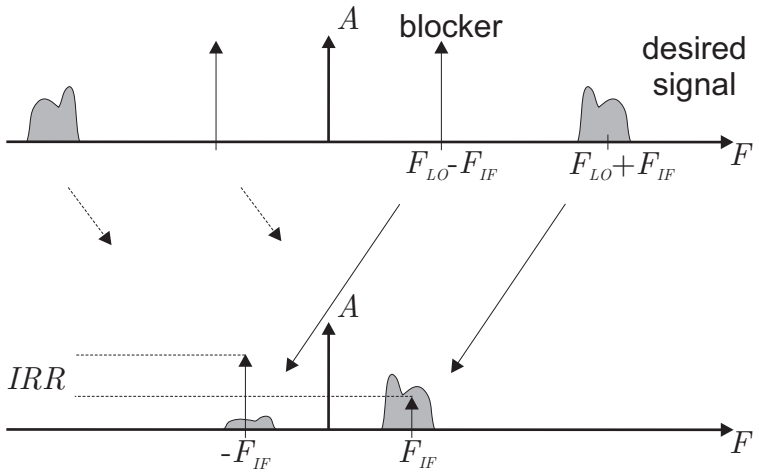

Figure 6.12 *The principle of mismatched quadrature mixing, where the mismatch-originated reverse frequency shift by $-f_{LO}$ is depicted with a dashed line.*

In the following simulations, the desired signal IF f_{IF} is assumed to be around 0.375 relative to the sampling frequency f_S and then the amount of generated interference on that frequency is studied. The interference source is expected to be a complex blocking tone at the frequency $-f_{LO} + f_{IF}$, thus creating a mirror image on f_{IF} in the down-conversion. The setup corresponds to the simplified situation where an exponential tone is situated on the mirror frequency $-f_{IF} = -0.375 f_S$ and the desired signal is omitted to simplify illustration. Now the imbalance effects of this complex tone are examined to evaluate the IRR levels before and after the compensation. A principal block diagram of the simulation setup is given in Figure 6.13. Gain and phase mismatches resulting in 20 dB IRR are assumed in the simulations.

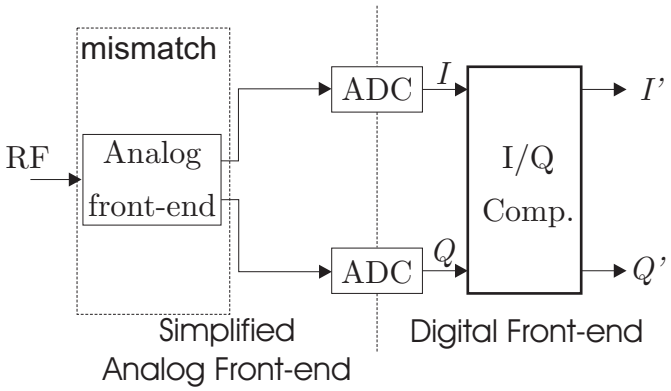

Figure 6.13 *Principal block diagram of the simulation setup in case of mismatched quadrature mixer and traditional ADCs.*

The simulation results are shown in Figure 6.14. The noise is assumed AWGN whose level is scaled to match the level of the first-order ΣΔ modulator noise shaping to match full band noise power. The expected 20 dB IRR before compensation is visible in the left hand figure. On the other hand, from the right side figure it can be seen that the compensation algorithm is clearly able to mitigate the distortion and the mirror component is pushed to the noise floor. Thus, the IRR after compensation is more than 80 dB, giving over 60 dB of improvement.

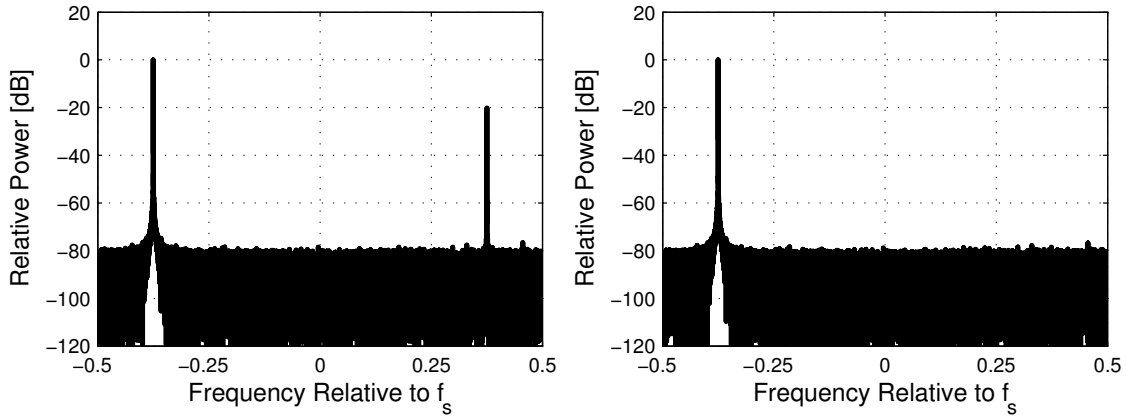

Figure 6.14 *Spectrum of the signal before (left) and after (right) the I/Q imbalance compensation in case of mixer mismatch and ideal traditional ADCs.*

6.3.2. Mismatched Quadrature Mixer with Ideal Quadrature ΣΔ ADC

The following scenario presents a similar mismatch source as in Sub-section 6.3.1 with a quadrature ΣΔ converter employed to digitize the signal. The noise transfer function notch is placed on the assumed desired signal band around 0.375 relative to f_S and the signal transfer function of the modulator has a unity response. Principal block diagram of the simulation setup is given in Figure 6.15. Similar 20 dB pre-compensation signal IRR is assumed as in Sub-section 6.3.1.

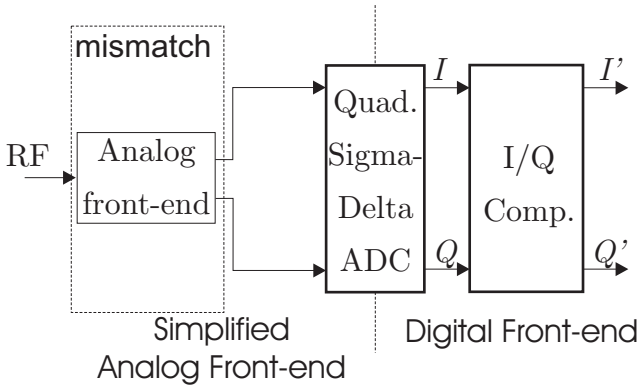

Figure 6.15 *Principal block diagram of the simulation setup in case of mixer mismatch and ideal quadrature ΣΔ ADC.*

The simulation results in Figure 6.16 show that in case of quadrature ΣΔ conversion the compensation algorithm doesn't mitigate the imbalance effects as well as in the case with traditional ADCs. The compensation increases the IRR of the tone to around 30 dB giving only 10 dB of improvement. In addition, when applying the compensation, more noise is pushed to the notch frequency, which also degrades the SNR of the desired signal on that frequency. The noise rise in the notch is in the order of 10 dB.

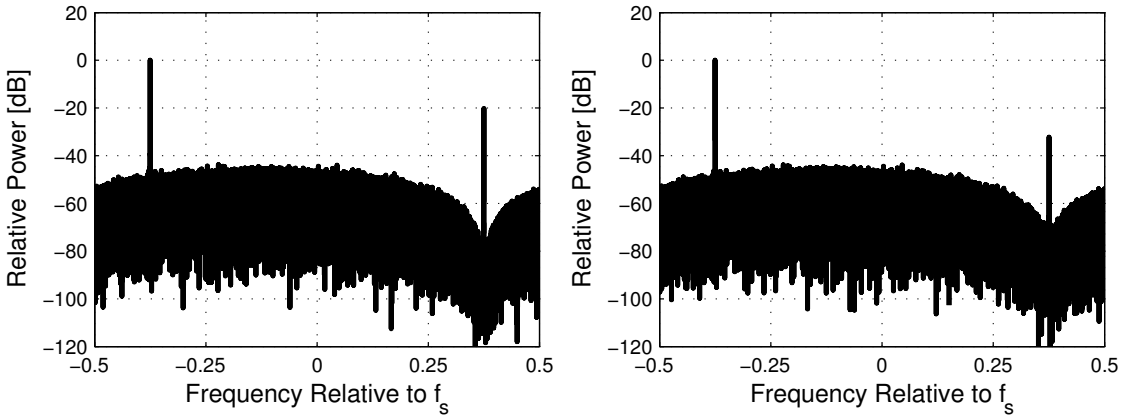

Figure 6.16 *Spectrum of the signal before (left) and after (right) the I/Q imbalance compensation in case of mixer mismatch and ideal quadrature ΣΔ ADC.*

The degradation of the compensation performance is due to the shaped and non-conjugated quantization noise. The algorithm handles the signal as a one entity and isn't able to separate the noise and the input signal. Thus, the quantization noise on the negative frequencies is disturbing the compensation of the mirror signal component, because there is no mirror correspondence for the noise part. The resulting compensated signal can be said to be a kind of compromise between the mirror interference compensation and degrading the noise shaping characteristics.

6.3.3. Ideal Quadrature Mixer with Mismatched Quadrature ΣΔ ADC

In this Sub-section, the mismatch in the quadrature ΣΔ converter feedback branch is considered. In order to highlight the related phenomena, a 10 % gain mismatch between the I and Q rails is applied and the preceding quadrature mixer is expected to be ideal. Thus, the input signal of the ΣΔ modulator is an ideal complex exponential. The corresponding principal block diagram is given in Figure 6.17.

The resulting modulator output spectrum on the left in Figure 6.18 shows that from the input signal point of view the IRR is again at the level of 20 dB. The clear difference when compared to the results of Sub-section 6.3.2 is however, that also the noise has been distorted. Comparing Figure 6.16 and Figure 6.18 shows more than 10 dB difference in the noise level at the center of the NTF notch. This is because the mixer mismatch didn't affect the noise part in any way, but the mismatch in the modulator feedback adds also the image noise transfer function response for the conjugated version of the noise, as was seen in Sub-section 5.2.3.

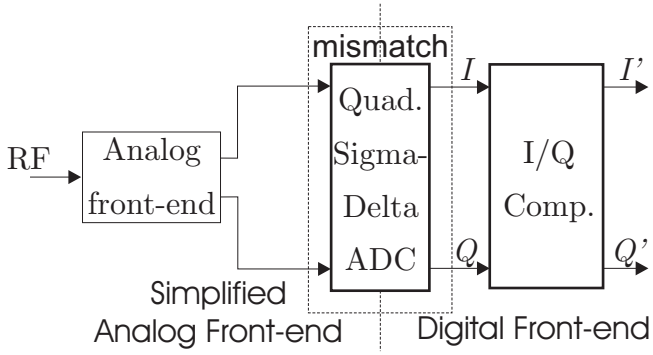

Figure 6.17 *Principal block diagram of the simulation setup in case of quadrature ΣΔ ADC feedback mismatch.*

The results after applying the compensation are quite similar as in Sub-section 6.3.2 when considering the overall performance. The algorithm pushes the mirror tone down by some 10 dB. Additionally, in this case, the noise floor is lowered due to the conjugated nature of the pre-compensation noise spectrum, as seen in the right plot of Figure 6.18. The main reason for sub-optimal compensation result is the different mirroring occurrences of the signal and noise components. The image signal and the image noise transfer functions were presented in Sub-section 5.2.3. The ISTF is frequency flat whereas the INTF has a notch on the negative frequencies making the combined compensation challenging.

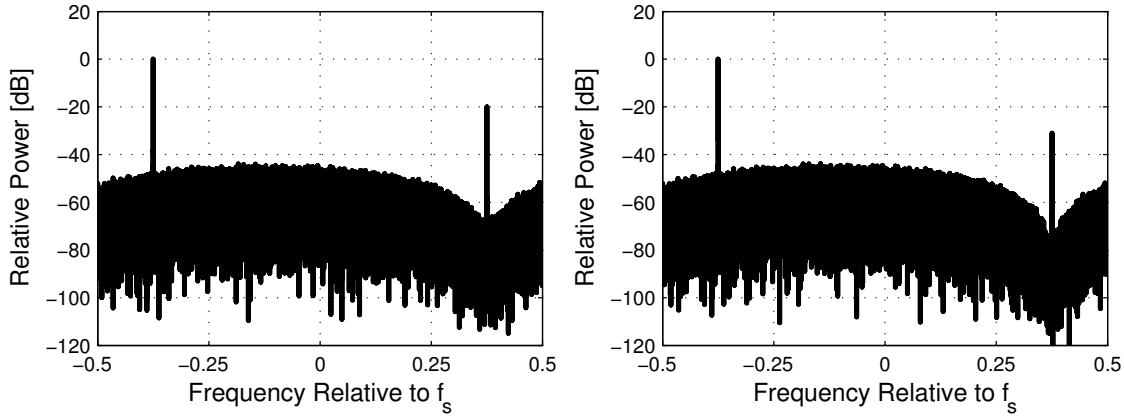

Figure 6.18 *The spectrum of the signal before (left) and after (right) the I/Q imbalance compensation in the case of the quadrature ΣΔ ADC feedback mismatch.*

Only feedback coefficient mismatch is considered here. The reasoning for this choice is based on the previous mismatch analysis and obtained results (in Chapter 5). There, it was found that mismatch in the input branches of the modulator correspond – from the post-compensation point of view – mismatched input for the whole modulator structure, which was considered above in Sub-section 6.3.2. On the other hand, the mirror interference effects in cases of mismatched loop filter and mismatched feedback are relatively similar, again from the post-compensation viewpoint.

7. CONCLUSIONS

The main purpose of this thesis was to clarify the design aspects and the possibilities of a quadrature ΣΔ modulator in radio receiver concept and to study the effects of I/Q imbalance in the modulator structure. The quadrature modulator provides an efficient possibility for analog-to-digital conversion in radio receivers employing the IF sampling architecture. So-called STF filtering seems to offer also possibilities to relax the requirements for the preceding analog filtering stages. The benefits over the real modulator have been shown in the literature, but some additional challenges still exist. Maintaining adequate I/Q separation is one example of the possible threats and has been chosen for the main theme of this study.

The basic theory related to the ΣΔ modulation was presented in Chapter 3 and analytic models for the first, the second and an arbitrary-order modulator were given (in Chapter 4). After this, the first-order case was expanded to include mismatches of the I and Q branches. An analytical model for the imbalanced modulator output was derived in Chapter 5, which was then utilized to determine the image rejection ratios for the input signal and the quantization error. The results were confirmed with simulations in Chapter 6. The derived models and the simulations were concluded to be consistent.

One of the main findings in the thesis was the different mirroring properties of the input signal carrying the information and the quantization error shaped inside the ΣΔ loop. The analysis revealed that depending on the exact location of the mismatch the amount of experienced mirror frequency interference varies notably. In addition, the effects are dependent on the choice of the modulator transfer function (the signal and the noise transfer functions) design. One practical example of this is that when considering the mismatched modulator feedback, the mirror frequency rejecting STF gives clear improvement in the IRR of the complex input signal.

Considering the simulated mismatch values and the dynamic range of the modern wideband receivers, the component mismatches and the resulting I/Q imbalance can be said to be a noteworthy problem in quadrature ΣΔ modulators. At the presence of a strong

blocking signal on the mirror frequency band, even slight mismatches, which could be practically ignored in a narrowband receiver, can cause severe distortion on the desired signal with weaker power level.

The I/Q imbalance mitigation algorithms proposed in literature are able to compensate efficiently the mirror frequency interference originating, e.g., from a non-ideal quadrature mixer. However, different mirroring effects on the input signal and the quantization error make the situation noticeably more complicated. Some examples of the simulated mitigation performance were given in Chapter 6 and it can be concluded that the used digital post-processing algorithm results in a sub-optimal compromise-like solution between the input signal and the quantization error mirroring. Thus, employing a quadrature ΣΔ modulator for the A/D conversion makes also the compensation of the quadrature mixer imbalance more challenging as was seen in Chapter 6.

When considering a wideband receiver with reduced analog filtering and a quadrature ΣΔ converter, novel mismatch compensation ideas should be developed, in addition to the one presented in this thesis, to guarantee reliable operation under the risk of strong blocking signals. In addition, the stability of the modulator in case of rapid and large input power fluctuations due to the out-of-band blocking signals should be studied further. However, these points are left for the future work together with expanding the mismatch analysis to cover the higher-order modulators and the continuous-time implementations of the structure.

REFERENCES

[1] A. A. Abidi, “Direct-conversion radio transceivers for digital communications,” *IEEE J. Solid-State Circuits*, vol. 30, vo. 12, pp. 1399-1410, Dec. 1995.

[2] Analog Devices, The Data Conversion Handbook, W. Kester, Ed. Burlington, MA: Newnes, 2004.

[3] L. Anttila, M. Valkama and M. Renfors, “Blind moment estimation techniques for I/Q imbalance compensation in quadrature receivers,” *IEEE 17th Int. Symp. Personal Indoor Mobile Radio Commun.*, Helsinki, Finland, 2006. pp. 1-5.

[4] L. Anttila, M. Valkama and M. Renfors, ”Circularity-based I/Q imbalance compensation in wideband direct-conversion receivers,” *IEEE Trans. Veh. Technology*, vol. 57, no. 4, pp. 2099-2113, July 2008.

[5] S. H. Ardalan and J. J. Paulos, “Analysis of nonlinear behavior in delta-sigma modulators,” *IEEE Trans. Circuits and Syst.*, vol. 34, no. 3, pp. 593-603, June 1987.

[6] J. Arias, P. Kiss, V. Prodanov, V. Boccuzzi, M. Banu, D. Bisbal, J. San Pablo, L. Quintanilla, and J. Barbolla, “A 32-mW 320-MHz continuous-time complex delta-sigma ADC for multi-mode wireless-LAN receivers,” *IEEE J. Solid-State Circuits*, vol. 41, no. 2, 339-351, Feb. 2006.

[7] P. A. Aziz, H. V. Sorensen and J. van der Spiegel, “An overview of sigma-delta converters: how a 1-bit ADC achieves more than 16-bit resolution,” *IEEE Signal Processing Mag.*, vol. 13, no. 1, pp. 61-84, Sept. 1996.

[8] P. A. Aziz, H. V. Sorensen and J. van der Spiegel, “Performance of complex noise transfer functions in bandpass and multi band sigma delta systems” *IEEE Int. Symp. Circuits and Syst.*, Seattle, WA, 1995. pp. 641-644.

[9] R. Bagheri, A. Mirzaei, M. E. Heidari, S. Chehrazi, M. Lee, M. Mikhemar, W. K. Tang, and A. A. Abidi, “Software-defined radio receiver: dream to reality,” *IEEE Commun. Mag.*, vol. 44, no. 8, pp. 111-118, Aug. 2006.

[10] R. Bagheri, A. Mirzaei, S. Chehrazi, M. E. Heidari, M. Lee, M. Mikhemar, W. K. Tang, and A. A. Abidi, “An 800-MHz–6-GHz software-defined wireless receiver in 90-nm CMOS,” *IEEE J. Solid-State Circuits*, vol. 41, no. 12, pp. 2860-1876, Dec. 2006.

[11] A. Baschirotto, F. Campi, R. Castello, G. Cesura, R. Guerrieri, L. Lavagno, A. Lodi, P. Malcovati, and M. Toma, "Baseband analog front-end and digital back-end for reconfigurable multi-standard terminals," *IEEE Circuits and Syst. Mag.*, vol. 6, no. 1, pp. 8-28, 1st quarter 2006.

[12] L. J. Breems, E. C. Dijkmans and J. H. Huijsing, "A quadrature data-dependent DEM algorithm to improve image rejection of a complex ΣΔ modulator," *IEEE J. Solid-State Circuits*¸ vol. 36, no. 12, Dec. 2001.

[13] L. J. Breems, R. Rutten, R. H. M. van Veldhoven and G. van der Welde, "A 56 mW continuous-time quadrature cascaded ΣΔ modulator with 77 dB DR in a near zero-IF 20 MHz band," *IEEE J. Solid-State Circuits*, vol. 42, no. 12, pp. 2696–2705, Dec. 2007.

[14] J. D. Bryant. (2006, June). How a Σ-Δ ADC Works. [Online]. Available: http://www.analog.com/analog_root/static/raq/moreInfo/How_a_S-D_ADC_Worksv2.pdf

[15] L. Cardelli, L. Fanucci, Y Kempe, E Mannozzi and D. Strle, "Tunable band-pass sigma delta modulator using one input parameter," *Electronics Lett.*, vol. 39, no. 2, pp. 187-189, Jan. 2003.

[16] A. B. Carlsson, *Communication Systems,* 3rd ed. New York: McGraw-Hill, 1986.

[17] T.-H. Chang and L.-R. Dung, "Fourth-order cascaded ΣΔ modulator using tri-level quantization and bandpass noise shaping for broadband telecommunication applications," *IEEE Trans. Circuits And Systems I: Regular Papers*, vol. 55, no. 6, pp. 1722–1732. July 2008.

[18] K. C. H. Chao, S. Nadeem, W. L. Lee and C. G. Sodini, "A higher order topology for interpolative modulators for oversampling A/D conversion," *IEEE Trans. Circuits and Syst.*, vol. 37, no. 3, pp 309-318, Mar. 1990.

[19] J. Crols and M. S. J. Steyaert, "A single-chip 900 MHz CMOS receiver front-end with a high performance low-IF topology," *IEEE J. Solid-State Circuits*, vol. 30, no. 12, Dec. 1995.

[20] J. Crols and M. S. J. Steyaert, "Low-IF topologies for high-performance analog front ends of fully integrated receivers," *IEEE Trans. Circuits and Syst. II: Analog and Digit. Signal Process.*, vol. 45, no. 3, pp. 269-282, Mar. 1998.

[21] Electronic Design. (2005, October) [Technology Report] Continuous-Time Delta-Sigma Converters. Available: http://electronicdesign.com/Articles/ArticleID/11289/11289.html

[22] G. Gagnon, "Continuous compensation of binary-weighted DAC nonlinearities in bandpass delta-sigma modulators," Ph.D. dissertation, Dept. Electronics, Carleton Univ., Ottawa, Canada, 2008.

[23] R. M. Gray and D. Neuhoff, "Quantization," *IEEE Trans. Information Theory*, vol. 44, no. 6, pp. 2325-2383, Oct. 1998.

[24] R. M. Gray, "Quantization Noise in ΔΣ A/D Converters," in *Delta-Sigma Data Converters*. Hoboken, NJ: Wiley-IEEE Press, 1995, ch. 2, pp. 44-74.

[25] J. Guilherme and J. Franca, "New CMOS logarithmic A/D converters employing pipeline and algorithmic architectures," *IEEE Int. Symp. Circuits and Syst.*, Seattle, WA, 1995, pp. 529-532.

[26] S. Hein and A. Zakhor, "On the stability of sigma delta modulators," *IEEE Trans. Signal Process.*, vol. 41, no. 7, pp. 2322-2348, July 1993.

[27] Y.-C. Ho, R. B: Staszewski, K. Muhammad, C.-M. Hung, D. Leipold and K. Maggio, "Charge-domain signal processing of direct RF samplingmixer with discrete-time filters in bluetooth and GSM receivers," *EURASIP J. Wireless Commun. Networking*, vol. 2006, no. 2, Apr. 2006.

[28] H. Inose and Y. Yasuda, "A unity bit coding method by negative feedback," *Proc. IEEE*, vol. 51, pp. 1524- 1535, Nov. 1963.

[29] M. Ismail and D. Rodríguez de Llera González, Eds., *Radio Design in Nanometer Technologies*, Dordrecht, Netherlands: Springer, 2006.

[30] D. Jakonis, K. Folkeson, J. Dabrowski, P. Erikson and C. Svensson, "A 2.4-GHz RF sampling receiver front-end in 0.18-μm CMOS," *IEEE J. Solid-State Circuits*, vol. 40, no. 6, pp. 1265–1277, June 2005.

[31] S. Jantzi, "Quadrature bandpass delta-sigma modulation for digital radio," Ph.D. dissertation, Dept. Electrical and Computer Eng., Univ. Toronto, Toronto, Canada, 1997.

[32] S. Jantzi, K. W. Martin, M. Snelgrove and A. S. Sedra, "A complex bandpass ΔΣ converter for digital radio," *IEEE Int. Symp. Circuits and Syst.*, London, UK, 1994, pp. 453-456.

[33] S. Jantzi, K. W. Martin and A. S. Sedra, “The effects of mismatch in complex bandpass ΔΣ modulators,” *IEEE Int. Symp. Circuits and Syst.*, Atlanta, GA, 1996, pp. 227-230.

[34] S. Jantzi, K. W. Martin and A. S. Sedra, “Quadrature bandpass ΔΣ modulation for digital radio,” *IEEE J. Solid-State Circuits*, vol. 32, no. 12, pp. 1935-1950, Dec. 1997.

[35] S. Jantzi, M. Snelgrove and R. Schreier, “Bandpass sigma-delta analog-to-digital conversion,” *IEEE trans. Circuits and Syst.*, vol. 38, no. 11, pp. 1406-1409, Nov. 1991.

[36] D. Johns and K. Martin, *Analog Integrated Circuit Design*. Crawfordsville, IN: John Wiley & Sons Inc., 1997.

[37] N. Jouida, C. Rebai and G. Ghazel, “Built-in filtering for out-of-channel interferers in continuous-time quadrature bandpass delta sigma modulators,” *14th IEEE Int. Conf. Electronics, Circuits and Syst.*, Marrakech, Morocco, 2007, pp. 947-950.

[38] N. Jouida, C. Rebai, G. Ghazel and D. Dallet, “Comparative study between continuous-time real and quadrature bandpass delta sigma modulator for multistandard radio receiver,” *Proc. Instrumentation Measurement Technology Conf.*, Warsaw, Poland, 2007, pp. 1-6.

[39] J. G. Kenney and L. R. Carley, “Design of multibit noise-shaping data converters,” *Analog Int. Circuits Signal Processing J.*, vol. 3, pp. 259-272, May, 1993.

[40] P. Kiss, ”Adaptive digital compensation of analog circuit imperfections for cascaded delta-sigma analog-to-digital converters,” Ph.D. dissertation, Elect. Eng. and Comput. Sci., Oregon State Univ., Corvallis, 1999.

[41] P. Kiss, J. Silva, A. Wiesbauer, T. Sun, U.-K. Moon, J. T. Stonick, and G. C. Temes, “Adaptive correction of analog errors in MASH ADCs – part II. Correction using test-signal injection,” *IEEE Trans. Circuits and Syst. II: Analog and Digit. Signal Process.*, vol. 47, no. 7, pp. 629-638, July, 2000.

[42] B. Le, T. W. Rondeau, J. H. Reed, and C. W. Bostian, “Analog-to-digital converters,” *IEEE Signal Proc. Mag.*, vol. 22, no. 6, pp. 69-77, Nov. 2005.

[43] E. A. Lee and D. G. Messerschmith, *Digital Communication*. Boston, MA: Kluwer Academic Publisher, 1988.

[44] P.-I. Mak, S.-P. U and R. P. Martins, “Transceiver architecture selection: review, state-of-the-art survey and case study,” *IEEE Circuits and Syst. Mag.*, vol. 7, no. 2, pp. 6-25, 2nd quarter 2007.

[45] K. W. Martin, “Complex signal processing is not complex,” in *IEEE Trans. Circuits and Syst.*, vol. 51, no. 9, pp. 1823-1836, Sept. 2003.

[46] J. Marttila, M. Allén and M. Valkama, ” I/Q imbalance effects in quadrature ΣΔ modulators – analysis and signal processing,” in *IEEE Int. Microwave Workshop Series RF Front-ends for Software Defined and Cognitive Radio Solutions*, Aveiro, Portugal, 2010, pp. 1–4.

[47] J. Marttila, M. Allén and M. Valkama, ”Quadrature ΣΔ modulation for cognitive radio – I/Q imbalance analysis and complex multiband principle,” *Circuits, Syst. and Signal Process.: Special Issue Embedded Signal Process. Circuits and Syst. Cognitive Radio-based Wireless Comm. Devices*, submitted and under review.

[48] S. Mirabbasi and K. Martin, “Classical and modern receiver architectures,” *IEEE Commun. Mag.*, vol. 38, no. 11, pp. 132-139, Nov. 2000.

[49] G. Mitteregger, C. Ebner, S. Mechnig, T. Blon, C. Holuigue, and E. Romani, “A 20-mW 640-MHz CMOS continuous-time ΣΔ ADC with 20-MHz signal bandwidth, 80-dB dynamic Range and 12-bit ENOB,” *IEEE J. Solid-State Circuits*, vol. 41, no. 12, pp. 2641-2649, Dec. 2006.

[50] K. Muhammad, R. B. Staszewski and D. Leipold, “Digital RF processing: toward low-cost reconfigurable radios,” *IEEE Commun. Mag.*, vol. 43, no. 8, pp. 105-113, Aug. 2005.

[51] National Semiconductor. (2008, January). National Semiconductor Delivers Industry’s First High-Speed, Continuous-Time Sigma-Delta Analog-to-Digital Converter. [Online]. Available: http://www.national.com/news/item/0,1735,1313,00.html

[52] J. Piper, “Floating-point analog-to-digital converter,” Ph.D. Disseration, Dept. Electroscience, Lund Univ., Lund, Sweden, 2004.

[53] K.-P. Pun, C.-S. Choy, C.-F. Chan and J. E. da Franca, “An I/Q mismatch-free switched-capacitor complex sigma-delta modulator,” *IEEE Trans. Circuits and Syst. I: Express Briefs*, vol. 51, no. 5, May 2004.

[54] G. Raghavan, J. F. Jensen, J. Laskowski, M. Kardos, M. G. Case, M. Sokolich, and S. Thomas III, "Architecture, design, and test of continuous-time tunable intermediate-frequency bandpass delta–sigma modulators," *IEEE J. Solid-State Circuits*, vol. 36, no. 1, pp. 5-13, Jan. 2001.

[55] B. Razavi, "Design considerations on for direct-conversion receiver," *IEEE Trans. Circuits and Syst. II: Analog and Digit. Signal Process.*, vol. 44, no. 6, pp. 428-435, June 1997.

[56] B. Razavi, *RF Microelectronics*. Upper Saddle River, NJ: Prentice Hall PTR, 1998.

[57] S. Reekmans, P. Rombouts and L. Weyten, "Mismatch insensitive double-sampling quadrature bandpass ΣΔ modulation," *IEEE Trans. Circuits and Syst. I: Regular Papers*, vol. 54, no. 12, Dec. 2007.

[58] L. Risbo, "Σ-Δ modulators-stability analysis and optimization", Ph.D. dissertation, Electronics Inst., Technical Univ. of Denmark, Lyngby, Denmark, 1994.

[59] A. Rusu, D. Rodríguez de Llera González and M. Ismail,"Reconfigurable ADCs enable smart radios for 4G wireless connectivity," *IEEE Circuits & Devices Mag.*, vol. 22, no. 3, pp. 6-11, May-June 2006.

[60] A. Rusu, D. Rodríguez de Llera González, M. Ismail and H. Tenhunen, "The Design of a Low-Distortion Sigma-Delta ADC for WLAN Standards," *Int. Symp. Signals, Circuits and Syst.*, Lasi, Romania, 2005, pp. 151-154.

[61] A. Rusu, B. Dong and M. Ismail, "Putting the 'flex' in flexible mobile wireless radios," *IEEE Circuits Devices Mag.* vol. 22, no. 6. pp. 24-30, Nov.-Dec. 2006.

[62] T. Salo, "Bandpass delta-sigma modulators for radio receivers", Ph.D. dissertation, Dept. Electrical and Communications Eng., Helsinki Univ. Technology, Helsinki, Finland, 2003.

[63] A. Silva, J. Guilherme and N. Horta, "Reconfigurable multi-mode sigma–delta modulator for 4G mobile terminals," *Integration, The VLSI J.*, vol. 42, no. 1, pp. 34-46, Jan. 2009.

[64] J. Silva, "High performance delta-sigma analog-to-digital converters," Ph.D. dissertation, Elect. Eng. and Comput. Sci., Oregon State Univ., Corvallis, 2005.

[65] R. Schreier, "An empirical study of high-order single-bit delta-sigma modulators," *IEEE Trans. Circuits and Syst. II: Analog and Digit. Signal Process.*, vol. 40, no. 8, pp. 461-466, Aug. 1993.

[66] R. Schreier, W. Yang and H. Shibata, "Quadrature bandpass ΔΣ converter," U.S. Patent 7262726, Aug. 28, 2007.

[67] R. Schreier and M. Snelgrove, "Bandpass sigma-delta modulation," in *Electronics Lett.*, vol. 25, no. 23, pp. 1560-1561, Nov. 1989.

[68] R. Schreier, G. C. Temes, *Understanding Delta-Sigma Data Converters*. Hoboken, NJ: John Wiley & Sons, Inc., 2005.

[69] W. M. Snelgrove, A. S: Sedra, G. R. Lang and P. O. Bracket, "Complex analog filters," unpublished. Available: http://www.dissonance.com/archive/journals/snelgrove_cmplx.pdf

[70] R. B. Staszewski, K. Muhammad and D. Leipold, "Digital RF processor (DRP™) for cellular phones," *IEEE/ACM Int. Conf. Computer-Aided Design*, San Jose, CA, 2005, pp. 122-129.

[71] M. Z. Straayer and M. H. Perrott, "A 12-bit, 10-MHz bandwidth, continuous-time ΣΔ ADC with a 5-bit, 950-MS/s VCO-based quantizer," *IEEE J. Soid-State Circuits,* vol. 43, no. 4, April, 2008.

[72] A. Swaminathan, "A single-IF receiver architecture using a complex sigma-delta modulator," M.S. thesis, Dept. Electronics, Carleton Univ., Ottawa, Canada, 1997.

[73] A. Tarighat, R. Bagheri, and A. H. Sayed, "Compensation schemes and performance analysis of IQ imbalances in OFDM receivers," *IEEE Trans. Signal Process.*, vol. 53, no. 8, pp. 3257-3268, Aug. 2005.

[74] R. Tortosa, J. M. de la Rosa, F. V. Fernández, A. Rodríguez-Vázquez, "Clock jitter error in multi-bit continuous-time sigma-delta modulators with non-return-to-zero feedback waveform," *Microelectronics J.*, vol. 39, no. 1, pp. 137-151, Jan. 2008.

[75] M. Valkama, "Advanced I/Q signal processing for wideband receivers: models and algorithms," Ph.D. dissertation, Dept. Information Technology, Tampere Univ. Technology, Tampere, Finland. 2001.

[76] M. Valkama, J. Pirskanen and M. Renfors, ”Signal processing challenges for applying software radio principles in future wireless terminals: an overview,” *Int. J. Commun. Syst.*, vol. 15, no. 8, pp. 741-769, Sep. 2002.

[77] M. Valkama, M. Renfors, and V. Koivunen, “Blind I/Q signal separation based solutions for receiver signal processing,” *EURASIP J. Appl. Signal Process. – Special Issue on DSP Enabled Radios*, vol. 2005, no. 16, pp. 2708-2718, Sep. 2005.

[78] R. J. van de Plassche, ”A sigma-delta modulator as an A/D converter,” in *Trans. Circuits and Syst.*, vol. 25, no. 7. pp. 510-514, July 1978.

[79] N. Vun, A. B. Premkumar, “ADC systems for SDR digital front-end” *Proc. 9th Int. Symp. Consumer Electronics*, Macau, Hong Kong, 2005, pp. 359- 363.

[80] R. H. Walden, “Analog-to-Digital Converter Survey and Analysis,” *IEEE J. Selected Areas Comm.*, vol. 17, no. 4, pp. 539-550, Apr. 1999.

[81] X. Wang, “A Fully Digital Technique for the Estimation and Correction of the DAC error in Multi-Bit Delta-Sigma ADCs,” Ph.D. dissertation, Elect. Eng. and Comput. Sci., Oregon State Univ., Corvallis, OR, 2003.

[82] R. Winoto, “Downconverting sigma-delta A/D converter for a reconfigurable RF receiver,” Ph. D. dissertation, Elect. Eng. and Comput. Sciences, Univ. California, Berkeley, 2009.

[83] J. Yang, R. W. Brodersen and D. Tse, “Addressing the dynamic range problem in cognitive radios”, *IEEE Int. Conf. Commun.*, Glasgow, Scotland, 2007, pp. 5183-5188.

[84] L. Yu and W. M. Snelgrove, “A novel adaptive mismatch cancellation system for quadrature IF radio receivers,” *IEEE Trans. Circuits and Syst. II: Analog and Digit. Signal Process.*, vol. 46, no. 6, pp. 789–801, Jun. 1999.